UNIVERSITÀ
DEGLI STUDI
DI PADOVA

UNIVERSITA DEGLI STUDI DI PADOVA

DIPARTMENTO DI INGEGNERIA INDUSTRIALE

PH.D. COURSE IN INDUSTRIAL ENGINEERING

CURRICULUM IN ELECTRICAL ENERGY ENGINEERING

XXXV CYCLE

ELECTRIC VEHICLE WIRELESS CHARGING SYSTEM WITH VEHICLE-TO-HOME CAPABILITIES

Coordinator of the Ph.D. Course:
Prof. Giulio Rosati
Coordinator of the Curriculum:
Prof. Luigi Alberti
Supervisor:
Prof. Manuele Bertoluzzo

Ph.D. Student: Abhay Kumar

Metricola: 1230458

Abstract

Wireless Power Transfer (WPT) is a method that has been developed for about two decades to charge the battery pack in electric vehicles (EVs). It behaves convenient features: that charge EVs by a WPT without any physical contact. In this power transfer takes place by magnetic coupling between two coils: which are placed under the road surface and onboard the vehicle. Therefore, with respect to wired EV charging, such a solution is more reliable as there are no connected items (cables, plugs and sockets), hence, there is no exposition of the connection items to the environment; moreover, it is more friendly, safe and secure as there are no plugs to insert, no cables on the sidewalk and much less chance of vandalism.

The different challenges that are currently with the electric power grid impose in terms of a synergistic, progressive, dynamic, and stable integration of electric mobility. Their solution is through a bidirectional power flow system through EVs. In this thesis some effects are taken to put these factors into a coherent framework for vehicle electrification in this thesis. The key contributions include the following areas: i) Grid-to-Vehicle, ii) Vehicle-to-Grid iii) Home-to-Vehicle, iv) Vehicle-to-Home, v) V2H Uninterruptible power supply have been discussed.

The step-by-step mathematical design of all the converters and coil system takes place as per the SAE J2954 for EVs and Low Voltage grid according to CEI 0-02, for bidirectional wireless system for V2H (BWV2H) application. On this basis, the input and output specifications for the BWV2H is designated. Subsequently, the active power involved at each conversion stage is calculated by the corresponding maximum current and voltage. This allows factors to determine the rating power of each power converter and of the passive elements arranging the BWV2H. The power sizings are of two different arrangements of BWV2H i.e., secondary in a chopper with cascade to the diode rectifier and a straightforward manner through the active rectifier was discussed.

The thesis continues with the study and analysis of converter losses at different stages together with the series-series (S-S) compensating coils, via two distinct approaches to control the power converters. The operation of converters in SAHFWPT and DAHFWPT are controlled by the extended phase shift and dual phase shift methods respectively. Moreover, in this study, we analysed the operation and losses of the uni-directional power flow of the WPT system, i.e., from the DC bus on the primary side to the battery load on the secondary side. The loss estimation includes high frequency switching losses, conduction losses, hard turn on and turn off losses coil losses, etc. Finally the efficiency of both arrangement are compared with respect to the internal phase shift angle of converters or input power.

Further, a study is carried out to review the effects of the different states of the control between primary and secondary H-bridge converters in WPT. However, in this arrangement the power regulated, in terms of active and reactive power takes place by changing external phase shift angle between both H-bridge by using DPS modulation method. It seems that the controller can work with a wide range of active and reactive power setups. Its helped in eliminating hard switching with small amount of reactive power drawn from source.

Finally, it includes discussion that control algorithms for BWV2H system only with the primary and secondary active H-bridge converter for battery charger. Its focuses on the power conversion stages that are needed for a charging work and grid synchronization at home. The algorithms are built one by one in the continuous time domain using techniques based on the

analysis of Bode diagrams of the transfer functions involved in the operation of the system. The performance of each algorithms are checked using the simulation done in Matlab/Simulink environment.

Dedicated to my mother & father

Acknowledgement

I wish to convey my heartfelt appreciation to everyone who assisted me throughout my PhD program by providing ongoing support and inspiration. Before anything else, I'd want to thank my advisor, Professor Manuele Bertoluzzo, for his supervision and seasoned counsel. His constant encouragement and support boosted my confidence in my research and ability to complete the course successfully. I would also like to thank Professor Giuseppe Buja for his invaluable advice, collaboration, constructive conversations, and support, all of which have contributed to the enhancement of my knowledge and abilities.

Once again, I'd like to express my appreciation to Prof. Manuele Bertoluzzo, my advisor in Padova, who secured my complete financing for the duration of my stay there and made sure I had a stable financial situation to work in. Following that, I'd want to thank the University of Padova for awarding me a *Borse di Ateneo* research scholarship.

This journey would not have been enjoyable without the company of my friends and fellow; in this way, I would like to express my gratitude to my lab colleagues Stefano and Amritansh for all of the assistance they provided and the positive working environment they fostered. I would like to express my appreciation in the same way to Stefano, Amritansh, Raghav, Subhadip, Rajat, and all of the others.

Last but not least, my loved ones, who have always been there for me and inspired me, are never far from my thoughts. I'd want to express my appreciation to my parents for giving me the opportunities they did, as well as to my sisters Divya, brother in law Rohit, brother chandan, and sister in law Archana and my lovely nephew and niece. Finally, I'd like to express my gratitude to my lovely wife Varsha, who always takes care of my child Advika (Radha) and my family even if I am not with them. Again, thanks to her for their moral support throughout my journey.

INDEX

Chapter 1

Introduction

1.1 Background

THE world biggest concern in the today's time is to increase the temperature of atmosphere of earth. That warning to human being for the wellbeing of mother earth and the existing lives on it. According to the records of several scientific agencies around the world, including National Aeronautics and Space Administration (NASA) and National Oceanic and Atmospheric Administration (NOAA), the year 2016 has been declared as the warmest year [1]. Contribution of conventional internal combustion engine (ICE) vehicles for global warming can be understood with the figure given by European Environment Agency (EEA) for the year 2016 according to which nowadays more than two-third of the CO_2 emission is done by ICE based vehicles. These emissions will increase rapidly in the coming future unless an appropriate action is taken [2]. Another big global concern is the forecasted crude oil scarcity in the coming future. Thus, to counter these issues, an ICE vehicle must be replaced by any other alternative technology. Electric vehicle (EV), in this context, is the best candidate due to its additional virtue of high efficiency, lower noise, zero-emission, and other. In current time being, In terms of vehicle autonomy, electric vehicles are not yet a mature technology, and a significant amount of research effort is being put forward by both academic institutions and private enterprises to enhance the overall performance of these vehicles. As per the Global EV outlook 2022 report the sales of the EVs are 6.6 million in 2021 i.e., the nearly10% of global car sales [3]. The target for zero emission CO_2 that can be achieve in transportation sector by 2050 through modernization conventional vehicle into highly efficient EVs. Apart from zero emission of CO2 from EVs, it wastes less energy during driving in cities, indeed, no tailpipe emissions of air pollutants such as nitrogen oxides and particles and less noise pollution too [4]. Up to the year 2022 there are several electric vehicles production company are available world wise market, such as Tesla, Volkswagen, Renault, Toyota, Nissan, Mecedes-Benz, Kia, Hyundai, Tata motors and many more [5]. However, in the initial stage of acceptance of EVs facing high production cost, performance, autonomy and recharging limitation of battery, indeed in current time the advancement in technology and several Government interest in world wise to increase the production of the EVs, public charging infrastructure, research on different method of charging such as plugin charging and wireless charging of EVs, to make the EVs more reliable sustainable, long lasting and less costly for the users [6].

1.2 History of Electric Vehicles

We're all aware that today's automotive industry has undergone a paradigm shift as a result of the advent of electric automobiles. Very less people are aware that the EVs are not a new innovation, these have been around lot longer than todays. Indeed, EVs come into existence long before the internal combustion engine (ICE) vehicle. The first motorized carriage was constructed by Robert Anderson around the beginning of the 1830s, perhaps between 1832s and 1839s. Its look trickier to ride this vehicle before 1859s as the rechargeable battery come into existing 1859s, it makes the EVs market more ideal and viable. EVs ruled the roadway vehicles sector in 1890s as it sells are higher than the gasoline vehicles, and showrooms, which continued to be increasingly popular up to the middle of the 1910s.

Nevertheless, all of this impetus would eventually come to a halt as a result of Ford's invention of the cost-efficient assembly line and the increased availability of petroleum. Several well-known enterprises, like Studebaker and Oldsmobile, had their start as manufacturers of EVs before transitioning into the production of vehicles powered by ICEs. Up until the middle of the 1910s, EVs were the first choice of both buyers and producers. The dark period for EVs in between 1914s to 1970s as the mass production of ICE vehicles are takes place.

From the 1960s through the 1980s, a series of events supposedly happened with the intention of bringing attention to the harmful consequences of pollution and environmental degradation; nevertheless, nobody brought the matter seriously and continued to disregard it. In the 1970s, 1980s, and 1990s, many countries started to realise that it had a nasty aspect even though there was a scarcity of foreign oil. The resurgence of EVs may be attributed to an increased consciousness of the drawbacks of combustion fuel and the dependence of ICE on it. In the late 1990s, a novel EV technology called the hybrid was made available for purchase on the market. The majority of hybrid vehicles are powered by gasoline, but they also include batteries that may be recharged when the vehicle comes to a stop or activated when the driver slows down, resulting in a decrease in fuel usage of around one-third.

A new movement toward electric vehicles has been sparked by the success of Toyota Motor Corporation in 2000s, which manufactures cars. A significant number of automobile manufacturers have opted to produce plug-in hybrid electric vehicles (PHEV), which feature a more compact ICEs but bigger battery packs and electric motors.

The revolution period of the EVs in the interval 2003s to 2020s. The demand of the EVs are increases exponentially, at the same time new battery technology entered the market, helping to improve range of EVs cost effective. Due to advancement of the technology the cost of lithium-ion batteries has reduced 97% since 1991 [7] and [8].

1.3 Benefits of EVs

The EVs stands out as the most promising alternative among the many technologies that are now available on the market as a result of the numerous advantages that it provides and the many benefits that it delivers.

a) Environment friendly

EVs contributes positive impact on the environment as they are able to reduce overall energy consumption as well as the amount of dangerous pollutants in the air. According to current research carried out in the United States, the eliminations of ICE leads to significant decreases in the overall emissions of volatile organic compounds (VOC), carbon monoxide (CO), and nitrogen oxides (NOx). Indeed, the use of EVs, powered by the energy supply by the thermal power plants, the green house emission from EVs may be limited to 59% compare to the ICE and its reduce the carbon foot print because of zero tailpipe emissions. It is important to take into account not just the emissions that are created by the vehicle itself, but also the activities that occur during the vehicle's entire life cycle that contribute to pollution. When it

comes to electric cars, a growing amount of waste batteries has a minimally negative impact on the surrounding environment [9] and [10]. It is good that lithium-ion batteries are more eco-friendly than other kinds of batteries, such as lead-acid and nickel–cadmium, since this indicates that other forms of batteries contribute more negatively to the environment.

b) Reduce the dependency on convention energy resource

The availability of fossil fuel is limited on earth, and that can be estinto in coming days. However, to power the EV wheel, it can converter 90% of energy of the grid. Whereas petrol and diesel vehicle only convert 17%-21% of energy to power the wheel. Indeed, the better alternative to power the EVs are by adopting renewable energy source (RES), that can led to reduce the dependence of vehicle on conventional energy source such as oil.

c) Healthier

It's wonderful news for human wellbeing since hazardous products of combustion are being lowered. Health and financial costs connected with air pollution may be reduced by improving air quality. Electrically powered vehicles provide less noise pollution as a consequence.

d) Low running cost

There are substantially smaller number of moving components in EVs than the traditional ICE vehicles. The yearly maintenance cost of the EVs is significantly low. The EV have good efficiency, when accompanied with the lower cost of electricity, results in the fact that recharging an EV is less expensive than refuelling a petrol or diesel vehicle for the same amount of travel.

e) Home-charge and discharge

EVs play an important role in meeting the grid's peak demand for electricity. During this time interval, the access energy in EVs can be utilised to give back to the grid. Even the EVs that are parked at home can be used to feed energy to the distributed network. And EVs can charge again when the grid's power demand is lower.

1.4 Drawback of EVs

Even if the proof of the benefits has become extremely evident, there are still certain drawbacks that each person has to think about before deciding whether or not to buy an electric vehicle as their next significant purchase. These are the reasons behind it:

a) Recharging Station

EV charging infrastructure is in the developing stage. If you don’t have a charging point at home, then it is quite difficult to find a charging station everywhere. So, at present, it is difficult to go on long drives with EVs. Apart from this, it’s also facing a longer charging period.

b) High initial investment

Since electric vehicles are still in their infancy on the market, you may be taken aback when you see how much they cost. Even the most budget-friendly versions may cost as much as $30,000 to $40,000, depending on the options and features.

c) Disadvantages of Silence

Quietness might have been a negative since people want to hear behind-the-scenes commotion. However, an electric vehicle is quiet and sometimes causes accidents [11].

1.5 Charging of EV

Electric vehicles may be refuelled in two ways: conductive charging (also known as cable charging) and wireless charging. To link the EV's charging port to the power grid, many connectors are utilized during the wired charging procedure. While charging by cable is common, it does have certain drawbacks. Most notably, there have been reports of difficulties with wires being entangled, and there have been concerns raised regarding its viability in damp environments. Over the last several years, there has been a rising tide of enthusiasm for decoupling electric load supply from the grid in favour of delivering it directly from a field. The rapid growth of decentralized power plants in recent years is largely responsible for this new emphasis. Field supply and wireless power transfer (WPT) systems relate to the same class of devices may be addressed using either term interchangeably. Their rollout has begun in order to jumpstart the process of charging the batteries installed in equipment that can operate off-grid. Currently, equipment is recharged while it is in a fixed, on-purpose arrangement; however, the ultimate goal is to feed the equipment while it is in motion, with the hope of either doing away with the batteries altogether or significantly reducing their power requirements. As time goes on, we will succeed at this. A charge is being put into the equipment even while it is being utilized for its intended purpose. When compared to the traditional cable method, wirelessly charging an electric vehicle's battery offers several advantages. In particular, wireless charging allows one to do away with the requirement for any plug, cable, or outlet; i) simplify the charging procedure; ii) transfer energy securely in any setting; etc. Any use of a cord, outlet, or plug is avoided. Improvements to the charging procedure that are more intuitive for the end user. iii) Power may be transmitted without risk in any setting. Because of these factors, it is expected that WPT will soon play a significant part in the process of charging electric vehicles.

The unique properties of electric, magnetic, and electromagnetic fields may be used in the construction of a WPTs via the employment of one of three distinct technological procedures. To achieve this goal, choose the most suitable method from those presented. Because magnetic field technology transfers more power per unit area than electric-field technology and is more efficient than electromagnetic-field technology, as employed in so-called inductive WPT system, is the most practical option. This is because it plays a role in inductively coupled WPT system. Actually, low-power inductive WPT system using tightly linked coils have been on sale to the public for a while now. However, in recent years there has been an increase in interest in the technique of supplying energy at a medium-to-high power

level to a piece of equipment that is located at a distant place. Resonant WPT system, shorthand for inductive WPT system with a resonant topology, are the kind of WPT system often used in such contexts. As an example, consider the widespread use of wireless charging for the batteries of electric cars.

Fig.1.1 depicts a resonant WPT system's overall architecture in a schematic format. It is made up of two different pieces: the primary section and the secondary section. Both of these sections include a coil that is related to the other section by a huge air gap in the middle. Power conversion circuitry is installed in both of the WPT system's individual portions. On the primary part, the grid supplies power to the coil by way of a combination of converters that may function as an AC-AC converter operating at low frequencies and producing high frequencies. Grid and AC-AC converter are the components that make up the supply for the primary coil. Then is capable of forming a magnetic coupling with the secondary coil, On the secondary end, the voltage that is induced across the secondary coil is used to charge the battery pack using an AC-DC converter. This converter adjusts the current and voltage that it produces in response to the needs of charging the battery.

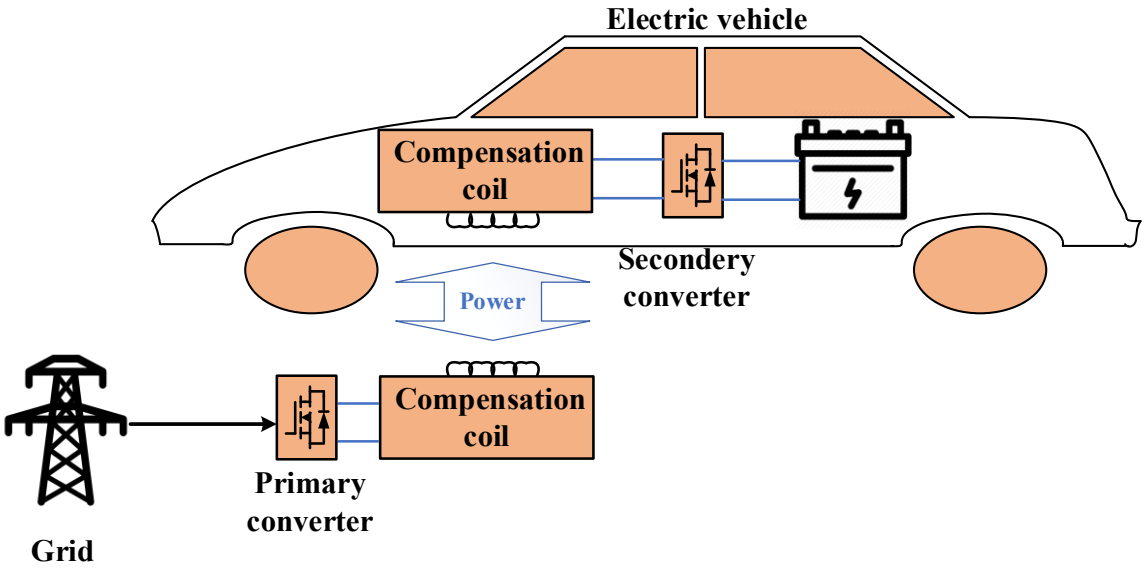

Fig. 1.1 WPT schematics

Despite the fact that we are aware that EVs have greater expenses at the moment. Then, we upgrade EV charging by using a WPT system. As a result, the total price of an EV rises dramatically. Most folks just cannot afford such a price range. Bidirectional wireless power transfer (BWPT) has gained popularity as a means to lessen this operating expense, hence lowering the total cost of ownership for EVs. But the current proliferation of distributed power generation has also prompted academics to investigate the use of BWPT for the purpose of charging and discharging electric vehicles. Therefore, a BWPT system can be used to realize the Grid-To-Vehicle (G2V) and Vehicle-To-Grid (V2G) concepts, which involve employing electric vehicles for purposes other than their traditional ones, such as driving the car by charging it via G2V, and instead treating the EV as the power source by using the battery as a

storage element for other users of the grid or other vehicles. V2G is a notion that stems from the principle of active demand, in which the end-user serves as both an energy consumer and generator.

Fig. 1.1 is applicable not only to the unidirectional WPT system for EVs charging but also to the BWPT system for EVs charging and discharging. In point of fact, we need to reconsider the functioning of the converter using a strategy that takes into account both directions. The flow of electricity will have an effect on how the converter is operated, and that change will take place. For instance, converters that are capable of functioning as inverters in the G2V power flow mode also have the capability of functioning as rectifiers in the V2G power flow mode.

1.6 Objective of the thesis

- ✓ To get an understanding of comprehensive analysis of the currently available wireless power transfer technologies, In addition to this, a study of the process of charging EVs using the WPT system.
- ✓ The standard SAE J2954 was used as the foundation for the research that was conducted on the WPT system. In order to charge electric vehicles in a unidirectional fashion using WPT, the J2954 standard, which referred as for the G2V method. The BWPT system does not have any standers. However, on the basis of J2954, which is often referred to as for V2G, an investigation for power flows reverse direction in BWPT systems is carried out.
- ✓ The purpose of this research is to analyse and evaluate the converters that used in BWPT systems in terms of the direction of power flow, efficiency, and power sizing.
- ✓ To evaluate the performance of the BWPT system using two distinct methods to the converter on the secondary side, one of which charges the battery using a chopper and the other of which does not use a chopper.
- ✓ To study the effect of external phase shift angle on the efficiency of the BWPT.
- ✓ Look into each converter's control approach for the BWPT system, such as synchronizing the flow of power between the primary and secondary converters, charging and discharging of batteries, and other similar activities.

1.7 Organization of the thesis

This thesis is organized into a total of six chapters, the first of which is the introduction. The general framework for the thesis is presented in the following:

Chapter 2

This chapter discusses the existing electric power grid challenges in term of synergistic, progressive, dynamic, and stable electric mobility integration. EV bidirectional power flow is their answer. This chapter proposes improvements in the following areas to integrate these previously stated variables into a vehicle electrification framework: G2V, V2G, Home-to-Vehicle (H2V), Vehicle-to-Home (V2H), Vehicle–to–Home Uninterruptible power supply, and more.

Chapter 3

This chapter interprets two power electronics converters-based bi-directional wireless power transmission systems for electric vehicles. In the second stage, we create a Vehicle-to-Home wireless charger step-by-step. The Italian reference technical guidelines for low-voltage utilities and SAE J2954 for wireless power transfer for electric cars set the design limits. Power scaling each step of the bidirectional wireless charger follows battery output power choices.

Chapter 4

This chapter analyses converter losses and series-series (S-S) compensatory coils in WPT systems using two alternative power converter control methods. The two approaches towards wireless DC-DC power flow control are termed as the Single-Active High Frequency Wireless Power Transfer (SAHFWPT) system and the Dual Active High Frequency Wireless Power Transfer (DAHFWPT) system. The extended phase shift and dual phase shift methods regulate converters in SAHFWPT and DAHFWPT, respectively. Both the SAHFWPT and DAHFWPT systems include active bridges. Ideal SAHFWPT and DAHFWPT efficiency evolutions are far from actual. This chapter also examines the WPT system's uni-directional power flow from the main DC bus to the secondary battery load. The converter controls WPT system efficiency. To test the concept, MATLAB/SIMULATION develops a 50 W–3600 W power range system at 85 kHz.

Chapter 5

Electric vehicles may act as flexible loads and mobile generators, making them important in future power grids, smart grids, and micro grids. Bidirectional electric car chargers are needed for complete V2H services. Hence, these systems must account for power supply variations in both directions. The EV's active and reactive power consumption and generation are examined in this chapter to assess the impacts of primary and secondary H-bridge control signal states. According to an analytical examination, the controller can function with a broad variety of active and reactive power settings in wireless power transfer between converters' primary and secondary sides.

Chapter 6

This chapter discusses Bi-directional wireless power transfer for V2H (BWV2H) system, with their control algorithms for primary and secondary active H-Bridge converter for battery charger. It focuses on power conversion stages for vehicle-to-home chargers and discharge. Bode diagrams and transfer functions are used to build each algorithm in continuous time. Each method was tested using Matlab/Simulink simulations.

1.8 Reference

1. National Aeronautics and Space Administration (NASA), National Oceanic and Atmospheric Administration (NOAA), 2017. [online]. Available: https://www.nasa.gov/press-release/2020-tied-for-warmest-year-on-record-nasa-

analysis-shows

2. European Environment Agency (EEA), 2016. [online]. Available: https://www.eea.europa.eu/publications/air-quality-in-europe-2016

3. International Energy Agency (IEA). Global EV outlook 2022 [online]. Available https://www.iea.org/reports/global-ev-outlook-2022

4. Electric vehicles: a smart choice for the environments. 2021. [online]. Available https://www.eea.europa.eu/articles/electric-vehicles-a-smart#:~:text=Electric%20motors%20are%20simply%20more,as%20nitrogen%20oxides%20and%20particles.

5. Jha, R., K.,. Power Stages and Control of Wireless Power Transfer Systems. 2018. https://www.research.unipd.it/handle/11577/3424780

6. König, A., Nicoletti, L., Schröder, D., Wolff, S., Waclaw, A., Lienkamp, M. "An Overview of Parameter and Cost for Battery Electric Vehicles," World Electr. Veh. J., 2021, 12, pp. 21.

7. The history of Electric vehicle, 2021. [online]. Available: https://blog.evbox.com/electric-cars-history

8. The history of the Electric car, 2014. [online]. Available: https://www.energy.gov/articles/history-electric-car

9. Allen, D. T., Shonnard, D. R. "Green Engineering: Environmentally Conscious Design of Chemical Processes," Prentice Hall: New York, 2001.

10. Malmgren, I. "Quantifying the Societal Benefits of Electric Vehicles," World Electr. Veh. J., 2016, 8, pp. 996-1007.

11. What is Electric car. [online]. Available https://www.conserve-energy-future.com/advantages-and-disadvantages-of-electric-cars.php

Chapter 2

Operation of Electric Vehicle with Home capabilities

2.1 Introduction

IN this chapter, we discuss the different challenges that the current electric power grid imposes in terms of a synergistic, progressive, dynamic, and stable integration of electric mobility. Their solution is through a bidirectional power flow system through EVs. In order to put these factors into a coherent framework for vehicle electrification, this chapter's key contributions include the following areas: i) G2V, ii) V2G iii) H2V, iv) V2H, v) V2H Uninterruptible power supply and many more.

2.2 EV Power Flow Principle of Operation in Smart Grid

Power in electric vehicles is transferred from the primary coil, which is buried in the road, to the secondary coil, which is located in the vehicle, through a magnetic field is known as WPT [1]. The WPT system includes coupling coils and the following components: i) a power supply connected with the primary coil to generate high-frequency voltage in accordance with SAE report J2954 [2], (ii) resonating capacitors together with the coupling coils to reduce the power supply sizing and increase the efficiency [3], and (iii) power conversion circuitry on the secondary side to convert the high-frequency-induced voltage into DC voltage suitable for the EV battery charging [4].

In the last few years, EVs have gained new interest from the grid-side point of view to mitigate the power fluctuations of renewable energy sources [5,6]. Ref. [7], for instance, demonstrates the grid frequency improvements in an isolated system derived from the EV battery utilization to reduce the impact of wind and solar generation. Such a strategy, known as V2G [8], stands on the fact that EVs are parked for most of the day and the energy stored in their batteries can be utilized during this time, provided that their initial state of charge (SoC) is restored before vehicle utilization by the user. The V2G strategy was created for the wired charging infrastructure, but it can be easily reproduced adopting the WPT technology [9,10], as long as all the unidirectional stages of the WPT systems are replaced by bidirectional ones to allow the power flow in both directions [11]. When considering a domestic or residential EV charging station, the V2G is also called Vehicle to Home (V2H) [12]. The customer in this case can either take advantage of the energy stored in the battery supplying its own domestic loads, or inject the power into the grid if the loads require low power [13,14,15]. The V2H strategy helps to stabilize or even reduce the variable power demand of domestic loads, decreasing the overall power cost. In addition, the user could receive remuneration for the service offered to the distribution system.

The developments concerning the recharging of EVs batteries allowed their utilization as distributed energy storage systems integrated into the distribution grid [16,17]. This scenario facilitates the flexibility of power management, providing grid services in an efficient and cost-effective way [16], through the so-called V2G concept. The EVs then not only draw the power from the grid, but they can deliver the power back to the grid via a bidirectional charger. In addition, their DC link capacitor inserted in the power conversion chain is inherently able to also provide reactive power to the grid utility [18], the EVs also has the ability to assist fix issues with power quality. The V2G concept can be easily extended to V2H systems to offer

more services. At the household level, the storage capacity presents significant potential such as voltage and load regulations and demand response capability. The V2H usually involves a single EV in a single house: its framework is depicted in Fig. 2.1, referring to a WPT charging infrastructure. While charging the battery, the EV absorb the power from the grid, but while discharging, the power flow has two possible directions: either to the domestic loads or to the main grid, according to the power demand of the home appliances during the discharging process.

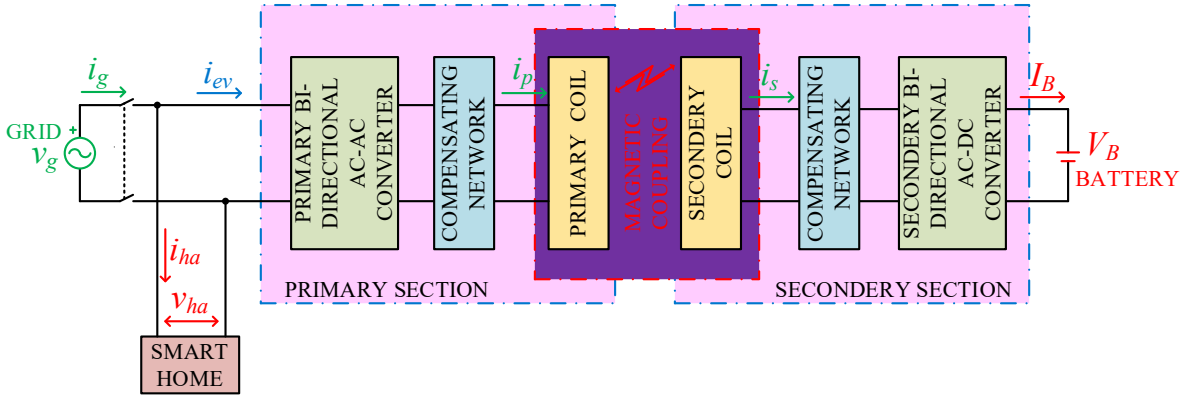

Fig. 2.1 BWPT converters block arrangement

2.3 Opportunities for Smart Grid

In the previous section, "Section 2.2," we discussed the basic workings of electric vehicle power flow structures with the smart Home, smart grid, and home electrical loads. Because the purpose of this section is not to conduct an perlustration of the electric vehicle wireless charger (EVWC) system in terms of power electronics, the precise details of the topologies of the converters, regardless of whether they are implemented in software or hardware, are not discussed in this section. Rather, the problems and possibilities presented by the electrification of vehicles in relation to smart grids and smart homes will be the primary emphasis of this section. This is due to the fact that the purpose of this section not being to conduct an examination of the structures.

2.3.1 EV Wireless Charger

The primary modes of operation of an EVWC are presented in this section, along with consideration given to the advantages and disadvantages, these modes provide challenges for the operations of smart houses and smart grids, in particular with respect to the controllability of power and the newly acquired features for the installation, where the electric vehicle has to park. Fig. 2.2 illustrates a scenario in which an electric vehicle has been connected to a smart home (typically, in a wireless power transfer system, a portion of the power electronics converter is located outside the EV (off-board), while the remaining portion is located within the EV (on-board)). To be more specific, the electric vehicle's battery is charged by means of an EVWC that is hooked into the electrical grid in parallel with the household loads. As a result, the electric vehicle itself is considered a home load for the duration of its stay at the location. As shown, from a smart grid point of view, bidirectional connection between the smart home and the electrical grid is studied from the standpoint of controllability.

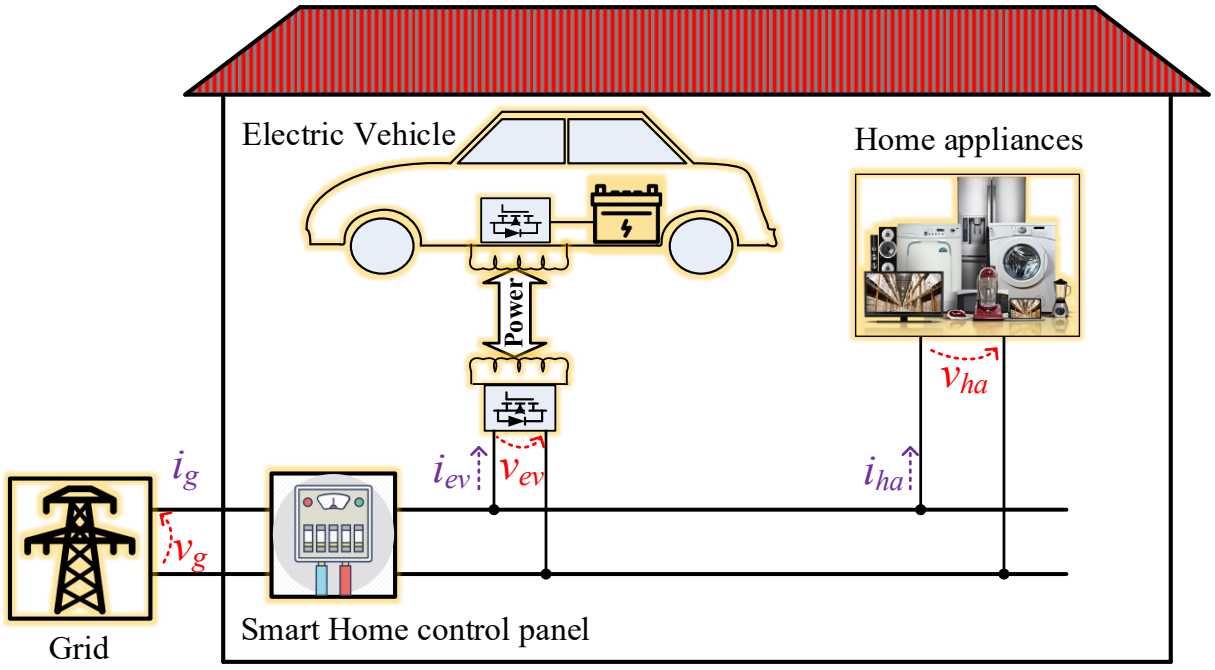

Fig. 2.2 BWPT scheme of principle

2.3.1.1 Grid-to-Vehicle (G2V)

In most electric vehicles, the G2V mode is the only one accessible, and its only focus is on charging the vehicle's battery from the power grid. Fig. 2.3(a) depicts the EVWC's connection to the electrical grid through a smart house, which allows for unidirectional and bidirectional power flow and bidirectional communication between the EVWC, the grid, and the smart home. In this mode of operation, the EVWC grid-side current (i_g) value is calculated independently of the other loads sharing the same electrical infrastructure (e.g., the entire current in a home is capped by the central circuit breaker, that might trip if the cap is breached). Fig. 2.3(b) depicts G2V mode voltage and current waveform, in a smart home by showing in the first subplot the grid voltage (v_g) in a solid red line, the grid current (i_g) in a solid black line, the home appliance load current ($i_{ha} = 0$) not present as there are no household loads connect to the EV, and the EVWC grid-side current ($i_{ev} = i_g$) that is represented by the solid green line in the second subplot. In this mode of operation, the ac–dc front-end converter is used to manage the current such that it is in phase with the voltage supplied by the power grid, so as not to degrade the power quality indices of the electrical grid. It is clear that actual circumstances, including skewed grid voltage (v_g) and current demands from household appliances, are not taken into account (i_{ha}). Entire current i_g taken from grid are utilised only charging to EV.

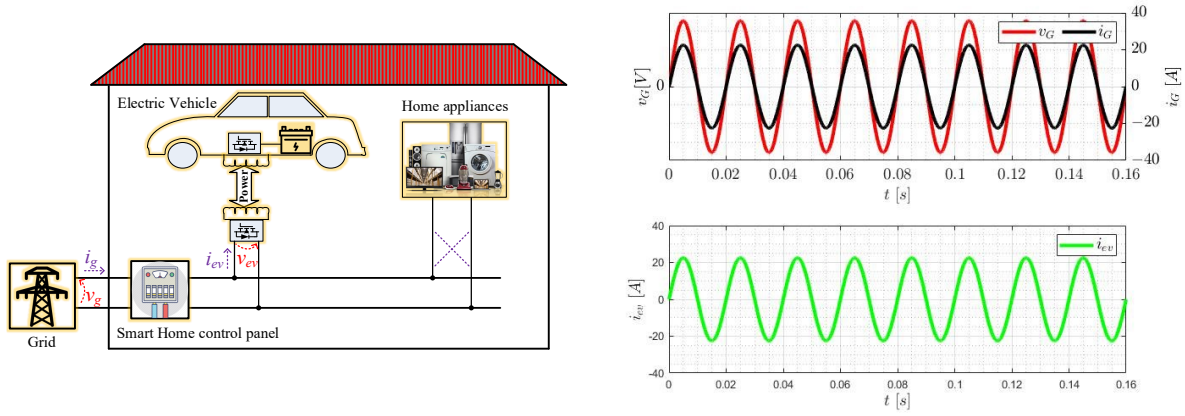

(a) (b)

Fig. 2.3 G2V mode only

2.3.1.2 Home-to-Vehicle (H2V)

The regulated G2V mode, which is shorthand for the method by which the battery of an electric car is charged straight away through the grid. On the other hand, the value about the working power at home energy manager, is changed in the controlled G2V mode depending on other loads that are connected in the house. When talking about a home-based or residential charging station for electric cars, the G2V connection is often referred to as the Home to vehicle connection. In addition, the operating power of the EVWC may be modified in line with the electricity that is injected by the grid while using the H2V mode of operation, for example. From the perspective of the smart home, the objective is to achieve a state of equilibrium between the generation and consumption of electrical power, while at the same time ensuring that the power quality delivered by the grid is not degraded (e.g., frequency and amplitude deviations on the grid voltage). In order to put this mode of operation into effect, it is vitally important to create the communication between the EVWC and the grid (or the house hold energy manager unit, i.e., at the same time as the EV concatenated with a smart home). The key operational concept that distinguishes the regulated H2V mode of operation is shown in Fig. 2.4(a). In this mode, the functionality of the energy management system at home is used to prevent overcurrent trips of the circuit breaker at the home control panel. Fig. 2.4(b) depicts H2V mode voltage and current waveform, in a smart home for the current demand by the grid i_g and the grid voltage v_g line for the domestic power demand contract, which are represented with the black and red solid line waveform in first subplot. The ac–dc front-end converter is used to manage the current such that the grid current is sinusoidal and in phase with the grid voltage, so as not to degrade the power quality indices of the electrical grid. In the second and third subplot the power demand of electrical home appliances together with the EV is represented in terms of current in a solid blue and green line waveform, and their amplitudes are equal (i.e., the power share by the EV and electrical home appliances are equal). Moreover, the maximum RMS current demand by the grid i_{g_max} is the sum of the current needed for EV charging i_{ev} and the current needed to power the electrical appliances at home i_{ha}, as expressed by equation (2.1).

$$i_{g\_max} = i_{ev} + i_{ha} \tag{2.1}$$

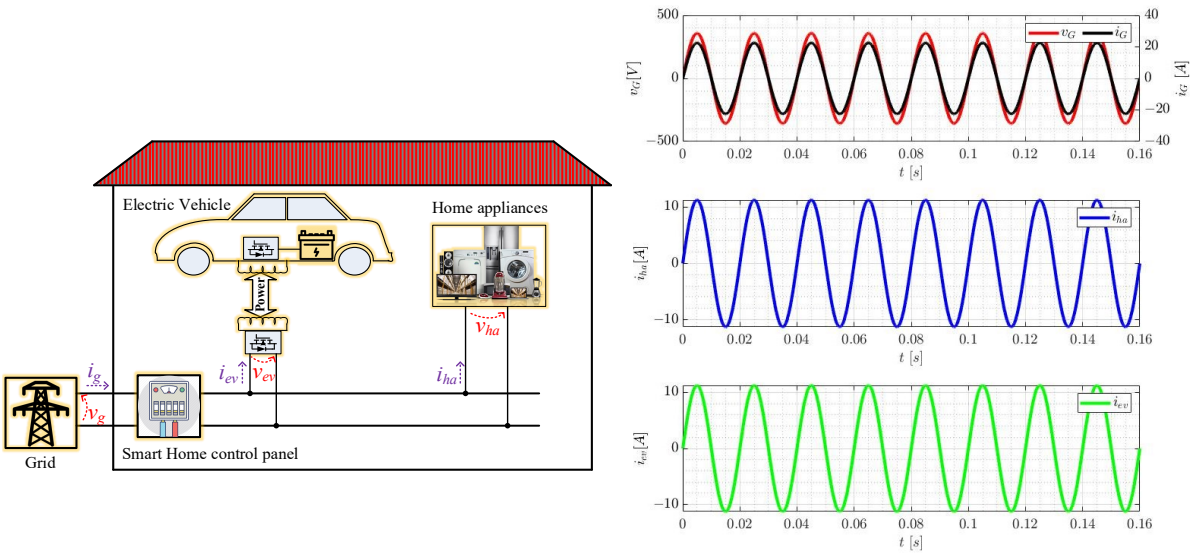

(a) (b)

Fig. 2.4 H2V with home appliance's

Fig. 2.5 provides an illustration of how the H2V regulated mode works in practice. The EVWC runs with a sinusoidal grid-side current, precisely like the H2V mode. However, its amplitude is modified in real time depending to the other loads in the house. During the progression from CASE #A to CASE #B and finally to CASE #C. In CASE #A (in time interval 0-0.08), there was equal power sharing by electrical appliances as a home load when they are active and the EV battery was in a charging state. As a consequence of this, the level of current consumption is equivalent to $i_{ha} = i_{ev}$. These are shown by the solid blue and green line waveforms in subplots two and three of Fig. 2.5, respectively. In CASE #B (in time interval 0.08-0.12), a some of home load was shut off, resulting in a lower current consumption i_{ha}, which caused the EVWC to increase the amount of running power it was using (increasing the current consumption, i_{ev}). However, due to the fact that the EVWC has an internal control system, the maximum power output that it is capable of cannot under any circumstances be surpassed. In CASE #C (in time interval 0.12-0.16), a some of home load was activated, which results in an increase in current consumption i_{ha}, leading the EVWC to reduce the amount of running power it uses (decreased the current consumption, i_{ev}). However, since these electrical household appliances have their own internal controls, the maximum amount of power that they are able to operate at cannot under any circumstances be surpassed. When this management approach is used to the charging of electric vehicle batteries, the maximum amount of power that the smart house is capable of functioning at is never surpassed, therefore the value remains the same. This is observable in the amplitude of the grid current i_g, which is shown as a continuous black line in the first subplot.

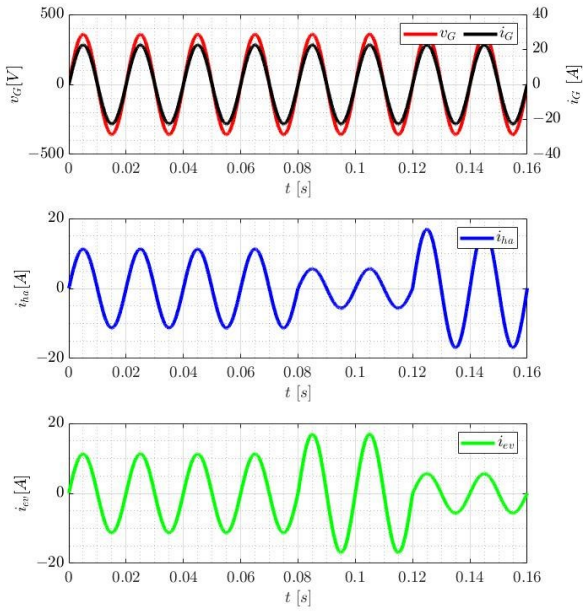

Fig. 2.5 H2V with power demand change of home appliance's

2.3.1.3 Vehicle-to-Grid (V2G)

The V2G mode's basic functioning is shown in Fig. 2.6 (a). The G2V mode is the primary mode of operation for the EV bidirectional battery charger; Whenever V2G scheme is enter into this state of operation, the EV's treated as the power sources and the portion of power store in EV batteries are flow back towards the domestic loads, smart grid, and power grid, together with power demand by the household appliances are not taken into the account, with the provision that the elementary SoC of EV batteries are return to a former state back when EV re-use by the user. This provides a convenience of operation for the grid management system and benefits the smart grid, power grid because it makes it possible to use the EV's as an energy storage system (ESS) to manage the smart grid, and power grid stability, as well as the user of the EV also benefited in term of running cost of vehicle. Fig. 2.6(b) depicts V2G mode voltage and current wave form, in a smart home by showing in first subplot the grid voltage (v_g) in solid red line, the grid current (i_g) in solid black line, the home appliance loads current ($i_{ha} = 0$) is not present as there is no household loads are connect to the EV, and the EVWC grid-side current ($i_{ev} = i_g$) that is represent with the solid green line in second subplot. In this mode of operation, the ac–dc front-end converter is used to manage the current such that it is in phase opposition with the voltage supplied by the power grid. This mode of operation is managed by the power grid supervisor in a smart grid and power grid environment, and it operates in line with the preferences of the electric vehicle driver. Because of this, when it is necessary to send energy from the EV's batteries to the smart grid and power grid, the EV will receive predetermined points of energy and will manage the current flowing through the battery.

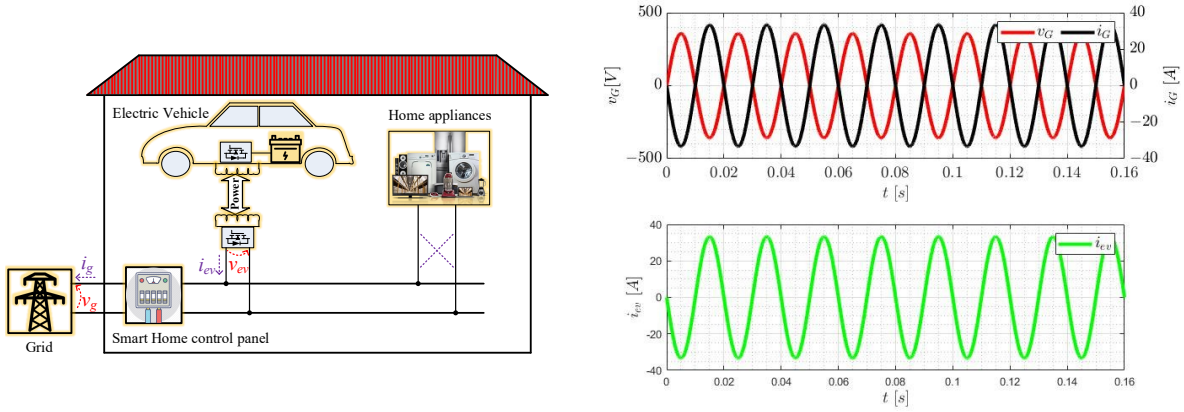

(a) (b)

Fig. 2.6 V2G mode only

2.3.1.4 Vehicle-to-Home (V2H)

The regulated V2G mode, which is shorthand for the method by which the battery of an electric car reverts back power to the grid. On the other hand, the value about the working power at home energy manager, is changed in the controlled V2G mode depending on other loads that are connected in the house. When talking about a home-based or residential charging station for electric cars, the V2G connection is often referred to as the Vehicle to Home (V2G) connection. In addition, the operating power of the EVWC may be modified in line with the electricity that is injected to the grid while using the V2H mode of operation, for example. From the perspective of the smart home, the objective is to achieve a state of equilibrium between the generation and consumption of electrical power, while at the same time ensuring that the power quality delivered to the grid is not degraded (e.g., frequency and amplitude deviations on the grid voltage). In order to put this mode of operation into effect, it is vitally important to create the communication between the EVWC and the grid (or the house hold energy manager unit, i.e., at the same time as the EV concatenated with a smart home). The key operational concept that distinguishes the regulated V2H mode of operation is shown in Fig. 2.7(a). In this mode, the functionality of the energy management system at home is used to prevent overcurrent trips of the circuit breaker at the home control panel. On the other hand, it is used in situations in which the current flowing through the electrical equipment in the house is more than the maximum total current permitted in the residence. Fig. 2.4(b) depicts H2V mode voltage and current waveform, in a smart home for the current supply to the grid i_g and the grid voltage v_g line for the domestic power demand contract, which are represented with the black and red solid line waveform in first subplot. The ac–dc front-end converter is used to manage the current such that the grid current is sinusoidal and in 180º out of phase with the grid voltage. In the second and third subplot the power demand of electrical home appliances together with the power supply by the EV is represented in terms of current in a solid blue and green line waveform, and the amplitudes of grid current and home current are equal (i.e., the power share by the grid and electrical home appliances are equal). Moreover, the maximum RMS current demand by the EV i_{ev_max} is the sum of the current needed for feedback power to grid i_g and

the current needed to power the electrical appliances at home i_{ha}, as expressed by equation (2.2).

$$i_{ev\_max} = i_g + i_{ha} \qquad (2.2)$$

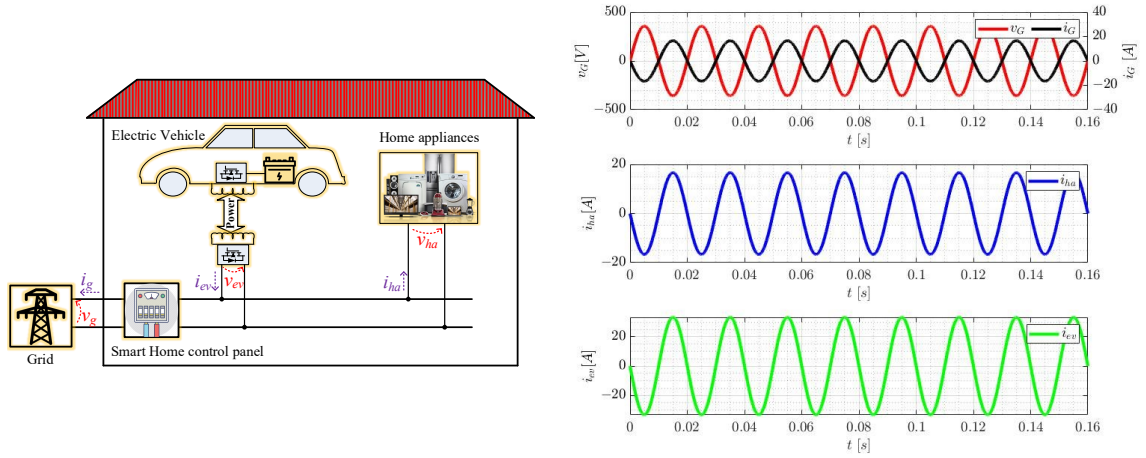

(a) (b)

Fig. 2.7 V2H with home appliance's

Fig. 2.8 provides an illustration of how the V2H regulated mode works in practice. The EVWC runs with a sinusoidal grid-side current, precisely like the V2H mode. However, its amplitude is modified in real time depending to the other loads in the house. During the progression from CASE #A to CASE #B and finally to CASE #C. In CASE #A (in time interval 0-0.08), there was equal power sharing by electrical appliances as a home load when they are active and the grid was in a power demand by alternate source such as EV's. As a consequence of this, the level of current consumption is equivalent to $i_{ha} = i_g$. These are shown by the solid blue and black line waveforms in subplots two and one of Fig. 2.8, respectively. In CASE #B (in time interval 0.08-0.12), a some of home load was shut off, resulting in a lower current consumption i_{ha}, which caused the grid to increase the amount of running power it was using (increasing the current consumption, i_g). However, due to the fact that the home power manager has an internal control system, the maximum power output that it is capable of cannot under any circumstances be surpassed. In CASE #C (in time interval 0.12-0.16), a some of home load was activated, which results in an increase in current consumption i_{ha}, leading the grid to reduce the amount of running power it uses (decreased the current consumption, i_g). However, since these electrical household appliances have their own internal controls, the maximum amount of power that they are able to operate at cannot under any circumstances be surpassed. When this management approach is used to the discharging of electric vehicle batteries, the maximum amount of power that the smart house is capable of functioning at is never surpassed, therefore the value remains the same. This is observable in the amplitude of the EV current i_{ev}, which is shown as a continuous green line in the third subplot.

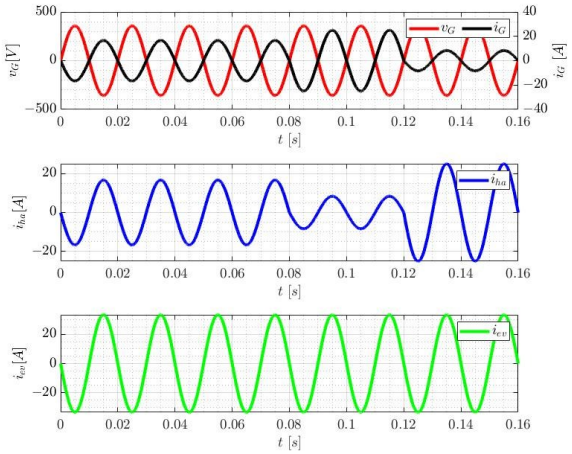

Fig. 2.8 V2H with power demand change of home appliance's

2.3.1.5 Vehicle–to-Home (V2H) Uninterruptible-power-supply

The EVWC has a second mode of operation that allows it to function as a voltage source, but with the features of an offline uninterruptible power supply (UPS). Because the EVWC can provide voltage to the smart house practically immediately in the case of a power outage, this mode opens a new possibility for smart homes. Therefore, in this method of operation, the EVWC must interact to the smart home in order to detect a power failure and restore power to the essential loads. Fig. 2.9 depicts the operating principle typical of the V2H mode as an UPS, making it easy to see that the EVWC is detached from the grid and runs in a unidirectional mode.

Similarly, to the described earlier method of operation, the grid-side converter of the EVWC functions with voltage control feedback and the current is set by the loads. A voltage failure may be detected by measuring the grid voltage, although this is not possible in the prior mode. When this happens, the EVWC immediately begins acting as a voltage source by sending a control signal to the main circuit breaker to disconnect the loads from the grid. The EVWC is aware of the issue once the grid power has been restored. When the grid voltage has completed a certain number of cycles, the system starts synchronizing with the phase of the voltage and, once the control system is synced, it returns to normal operation, at which point the loads are once again supplied by the grid. After this is complete, the EVWC might enter an idle state or switch to a different mode of operation (G2V, V2G, etc.). The schematic for this mode's operation is shown in Fig. 2.9 (b), which depicts the grid voltage (vg), grid current (i_g.), loads voltage (v_{ha}), loads current (i_{ha}.), EVWC voltage (v_{ev}), and EVWC current (i_{ev}). There are four distinct use-cases for this kind of functioning. In CASE #A (in time interval 0-0.08), the EVWC is linked to the grid to receive electricity and charge the batteries in a G2V mode (i.e., with a sinusoidal current and unitary power factor). In CASE #B (in time interval 0.08-0.12), the EVWC detects a drop in grid voltage and switches to UPS mode, powering the loads. If CASE #C (in time interval 0.12-0.16) occurs, the grid power is restored, the EVWC exits UPS mode, and the loads are once again supplied back via the electrical grid. A sinusoidal voltage is produced by the EVWC, as indicated, even when the

grid voltage is distorted (CASE #A and CASE #C) or when there is no grid voltage (CASE #B).

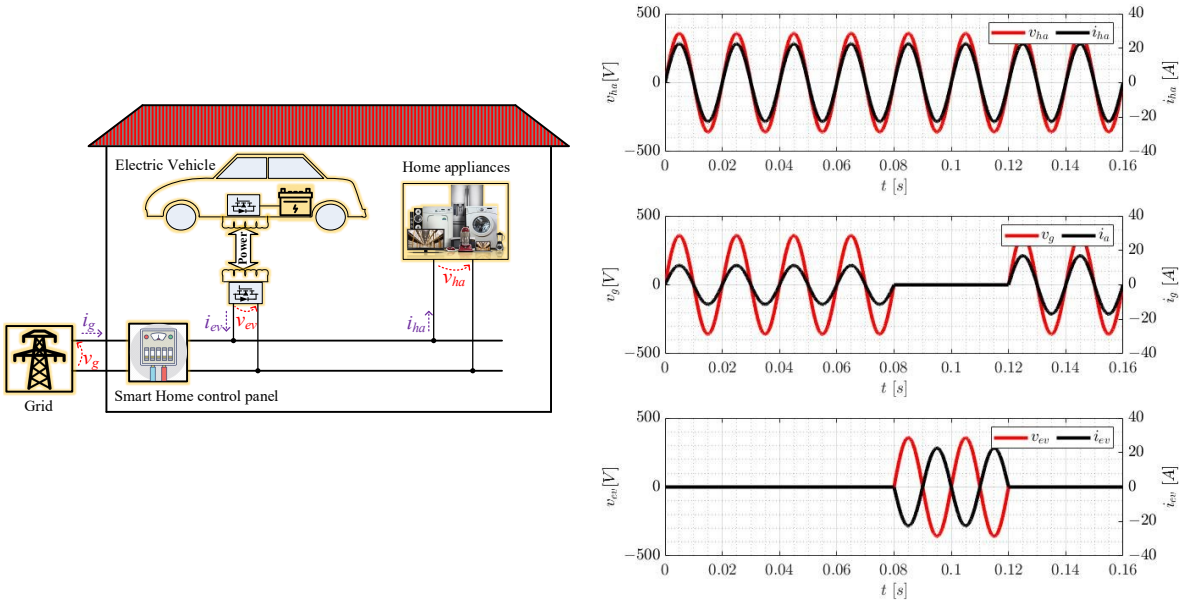

(a) (b)

Fig. 2.9 V2H with Uninterruptible-power-supply

2.4 Conclusions

The electrification of vehicles is now a reality, and its enormous foreseeable growth and accompanying potential point toward a paradigm shift in the urban transportation industry. The positive benefits of this revolution on the electrical power system must, however, be balanced against the additional difficulties that have arisen as a result of it. As such, this chapter presents a thorough overview of the new issues and possibilities presented by on-board and off-board EVWCs in the form of operating modes that may be handled by smart grids.

It has been shown that in-vehicle EVWCs have applications beyond grid-to-vehicle and vehicle-to-grid communication throughout this chapter. However, it has been shown that on-board EVWCs may be linked with other aspects of smart grids, such as renewable energy sources and energy storage systems, while simultaneously correcting power quality concerns in the locations where they are deployed. There has been a lot of talk about the positive effects of new technologies toward a more sustainable future, and one of them is the potential for on-board and off-board EVWCs to provide chances for smart grids.

2.5 Reference

1. Li, S., Mi, C.C. “Wireless power transfer for electric vehicle applications,” IEEE J. Emerg. Sel. Top. Power Electron. 2015, 3; pp. 4–17.

2. J2954: Wireless Power Transfer for Light-Duty Plug-In/Electric Vehicles and Alignment Methodology; SAE International: Warrendale, PA, USA, 2020.

3. Chinthavali, M., Onar, O.C. “Tutorial on wireless power transfer systems,” In Proceedings of the IEEE Transportation Electrification Conference and Expo (ITEC), Dearborn, MI, USA, 27–29 2016; pp. 1–142.

4. Monteiro, V., Afonso, J.A., Ferreira, J.C., Afonso, J.L. “Vehicle Electrification: New Challenges and Opportunities for Smart Grids,” *Energies* 2019, *12*, pp. 118.

5. A. Ahmad, M. S. Alam, and R. Chabaan, “A Comprehensive Review of Wireless Charging Technologies for Electric Vehicles,” in IEEE Transactions on Transportation Electrification, 2018, 4, 1, pp. 38-63,

6. A. A. S. Mohamed, and O. Mohammed, “Bilayer Predictive Power Flow Controller for Bidirectional Operation of Wirelessly Connected Electric Vehicles,” in IEEE Transactions on Industry Applications, 2019, 55, 4, pp. 4258-4267,

7. D. T. Hoang, P. Wang, D. Niyato, and E. Hossain, “Charging and Discharging of Plug-In Electric Vehicles (PEVs) in Vehicle-to-Grid (V2G) Systems: A Cyber Insurance-Based Model,” in IEEE Access, 2017, 5, pp. 732-754,

8. Y. Yang, Y. Benomar, M. El Baghdadi, O. Hegazy, and J. Van Mierlo, “Design, modeling and control of a bidirectional wireless power transfer for light-duty vehicles: G2V and V2G systems,” 2017 19th European Conference on Power Electronics and Applications (EPE'17 ECCE Europe), Warsaw, Poland, 2017, pp. 1-12,

9. H. Ben Sassi, F. Errahimi, N. Essbai, and C. Alaoui, “V2G and Wireless V2G concepts: State of the Art and Current Challenges,” 2019 International Conference on Wireless Technologies, Embedded and Intelligent Systems, Fez, Morocco, 2019, pp. 1-5,

10. S. Samanta, and A. K. Rathore, “A single-stage universal wireless inductive power transfer system with V2G capability,” 2018 International Conference on Power, Instrumentation, Control and Computing, Thrissur, India, 2018, pp. 1-5,

11. Bertoluzzo, M., Giacomuzzi, S., and Kumar, A. “Design of a Bidirectional Wireless Power Transfer System for Vehicle-to-Home Applications,” Vehicles 2021, 3, pp. 406–425.

12. G. Dong, T. Mishima, and H. Omori, “A Dual-Active Single-Ended Wireless V2H System with Mutually Synchronized Phase-Difference Control Method,” 2022 IEEE 17th Conference on Industrial Electronics and Applications , Chengdu, China, 2022, pp. 810-815,

13. S. Ohara, H. Omori, N. Kimura, T. Morizane, M. Nakaoka, and Y. Nakamura, “A new V2H system with single-ended inverter drive bidirectional wireless resonant IPT,” 2014 International Power Electronics and Application Conference and Exposition, Shanghai, China, 2014, pp. 619-623,

14. H. Fukuoka et al., “A new resonant IPT wireless V2H system with bidirectional single-ended inverter,” 2014 16th European Conference on Power Electronics and Applications, Lappeenranta, Finland, 2014, pp. 1-6,

15. T. Takahashi, H. Omori, M. Tsuno, N. Kimura, and T. Morizane, “A New Control Method of One-Switch Wireless V2H with a Combination of Resonant Selector and Voltage Changer,” 2019 8th International Conference on Renewable Energy Research and Applications , Brasov, Romania, 2019, pp. 663-667,

16. Igualada, L., Corchero, M., Cruz-Zambrano, F. “Optimal energy management for a residential microgrid including a vehicle-to-grid system,” IEEE Trans. Smart Grid 2014, 5, PP. 2163–2172.

17. Y. Luo, J. He, H. Liu, and L. Wu, “Application of the distributed generation, micro and smart power grid in the urban planning,” The 4th Annual IEEE International Conference on Cyber Technology in Automation, Control and Intelligent, Hong Kong, China, 2014, pp. 634-637,

18. Sangswang, A., Konghirun, M. “Optimal Strategies in Home Energy Management System Integrating Solar Power, Energy Storage, and Vehicle-to-Grid for Grid Support and Energy Efficiency,” IEEE Trans. Ind. Appl. 2020, 56, pp. 5716–5728

Chapter 3

Bidirectional wireless power transfer converter topology with Electric vehicle

3.1 Introduction

THE Bi-directional wireless power transfer system [1] is made up of two Uni-directional WPT converters [2,3], which are depicted in Fig. 3.1 by the help block B_1 and B_2 together with the other electrical parameters. Indeed, block B_1 is employed to propagate power P_{gB} from grid to battery (i.e., forward mode), and block B_2 is employed to propagate power P_{Bg} in the opposite direction, i.e., battery to grid (i.e., backward mode). While seeing the arrangement in Fig. 3.1, it looks like two different converter arrangements are required for the power flow in either direction. However, in the real-life scenario, this was not the case. We use single converters at each stage of WPT with the bi-directional switch to regulate the power flow in either direction of the bi-directional WPT converters. In initial study of this chapter, we interpret two distinct arrangements based on power electronics converters technology of Bi-directional wireless power transfer for V2H (BWV2H) [4]. In the second stage of this chapter, we present a comprehensive step-by-step design of a wireless charger for a Vehicle-to-Home application. The design procedure begins from the constraints disposed by the Italian reference technical rules for Low Voltage utilities (CEI-021) [5] and by the standard SAE J2954 for Wireless Power Transfer for electric vehicles [6]. The selection of the output power of the battery is followed by the power sizing of each stage of the bidirectional wireless charger.

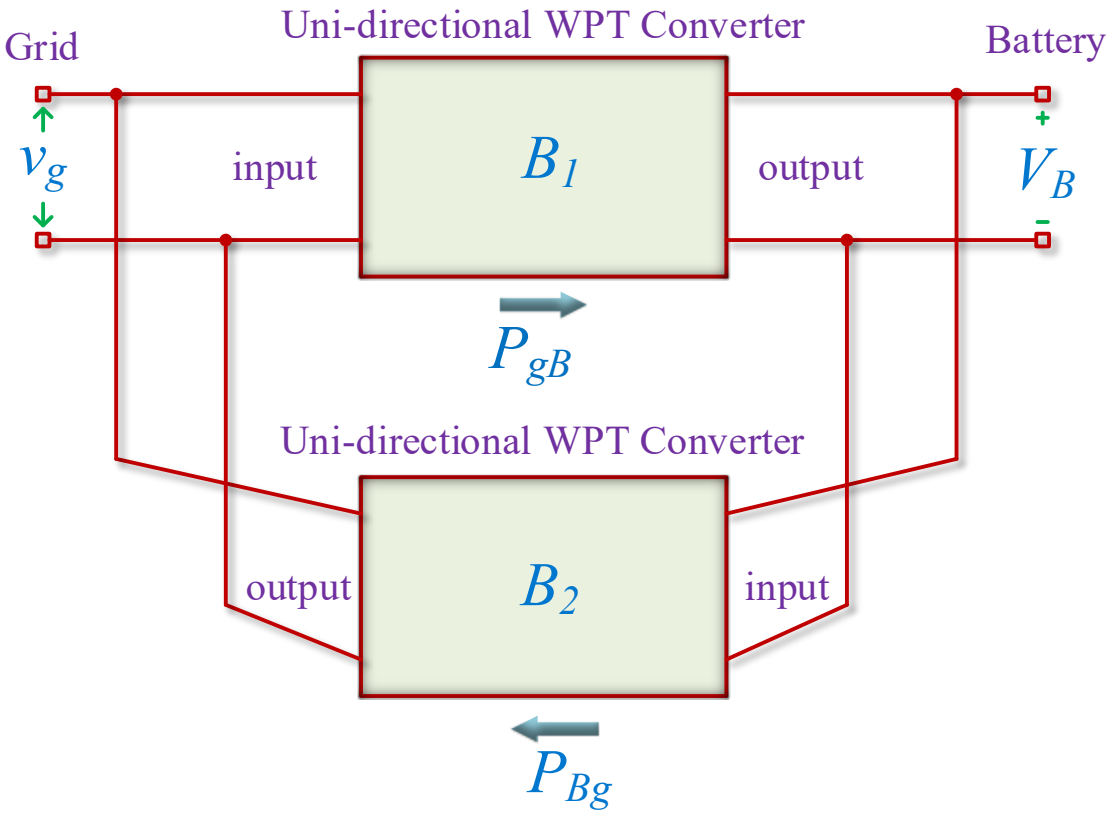

Fig. 3.1 Construction of a Bi-directional WPT Converter using Ui-directional WPT Converter

3.2 Type of Bi-directional WPT

The BWV2H schematic is shown in Fig. 3.1. It's simply arranged in the form of the black box. The black box doesn't show what kind of converter topology, circuit configuration, and coil arrangement that is being used. That merely indicates the direction of the power flow that takes place between the domestic grid and electric vehicles. To further understand the operation of BWV2H, its converter topology, circuit configuration, and coil arrangement are further

divided into two different converter topologies, whose descriptions are presented in the upcoming subsection 3.21 and 3.2.2 of the chapter.

3.2.1 Bi-directional WPT with secondary uncontrolled rectifier and chopper

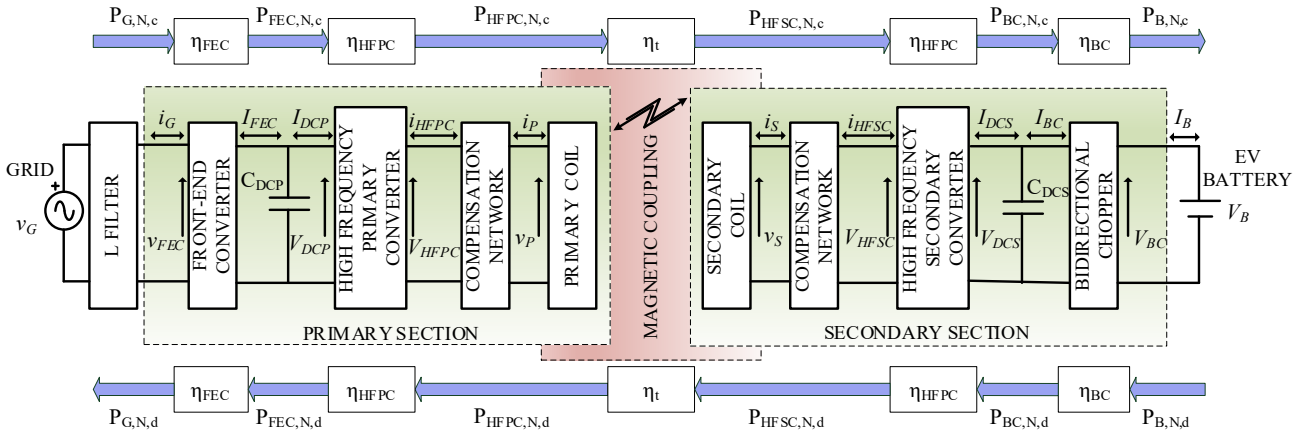

Fig. 3.2 BWV2H with the uncontrolled rectifier with chopper

The WPT chargers stand on the inductive coupling principle between two coils. The alternating magnetic field produced by the alternating current flowing through the coil placed under the road, hereafter called the primary coil, induces a voltage across the coil placed on board the vehicle, hereafter called the secondary coil. The voltage v_s induced on the secondary coil derives from the well-known Faraday law [7] (3.1), which can be rewritten as in (3.2) in the case of sinusoidal quantities, according to Steinmetz transform [8]

$$v_S = M\frac{di_P}{dt} \tag{3.1}$$

$$\bar{V}_S = j\omega_{HF} M \bar{I}_P, \tag{3.2}$$

where M is the mutual inductance between the coils, i_P is the current flowing through the primary coil, V_S and I_P are the peak values of v_S and i_P, and ω_{HF} is the supply angular frequency. Equation (3.2) is inferred considering the current i_P as purely sinusoidal. Being the induced voltage across the secondary coil dependent from the supply frequency of the primary coil, the highest is the supply frequency f_{HF}, the highest is the efficiency of the power transmission between the two coils and the smaller are the requested size for the two coils. For this reason, the primary coil cannot be directly fed by the grid utility, but several conversion stages are required: specifically, a rectification stage followed by an inversion one, to proper supply the primary coil at higher frequency. Finally, since the battery calls for Direct Current (DC), a further rectifier is needed on the secondary coil, which can be followed by a chopper to regulate the battery voltage. In a BWV2H application, the power flows alternatively from the grid to the battery and vice versa; then, both the chopper and the rectification stages need to be bidirectional. Fig. 3.2 depicts the architecture of the BWV2H. During charging mode, the grid voltage v_G feeds the Front-End Converter (FEC) with the grid current i_G through a filter inductor with inductance L_G. The FEC output current I_{FEC} is filtered by a capacitor C_{DCP} to maintain the DC primary voltage V_{DCP} nearly constant. The current I_{DCP} supplies the High Frequency

Primary Converter (HFPC), whose output voltage and current are v_{HFPC} and i_{HFPC}, respectively. The current i_{HFPC} flows in the compensation network and, subsequently, in the primary coil. If a series compensation is adopted, as explained in Section 3.5.1.2.5, i_{HFPC} corresponds to the current circulating through the primary coil, i.e. i_P. The voltage v_S induced across the secondary coil forces the circulation of the current i_S, which corresponds with the current i_{HFSC} at the input of the High Frequency Secondary Converter (HFSC) in case of series compensation. The input voltage of the HFSC is v_{HFSC}, whilst the output is V_{DCS}, which corresponds to the voltage across the capacitor C_{DCS}. The HFSC output current is split between the current flowing through C_{DCS} and the one at the input of the Bidirectional Chopper, namely I_{BC}. Finally, the BC output are the battery voltage and current, V_B and I_B, respectively. The FEC, the HFPC and the HFSC are Bi-directional H-bridge converters. The BC can reverse the current flow but not the voltage, which is necessarily lower on the battery-side, i.e. $V_B < V_{DCS}$. The HFPC and HFSC operate as the uncontrolled rectifiers, while power flow takes place from G2V and vice versa as V2G, respectively. The uncontrolled operations are done by the body diode of the MOSFETs.

3.2.2 Bi-directional WPT with secondary controlled rectifier

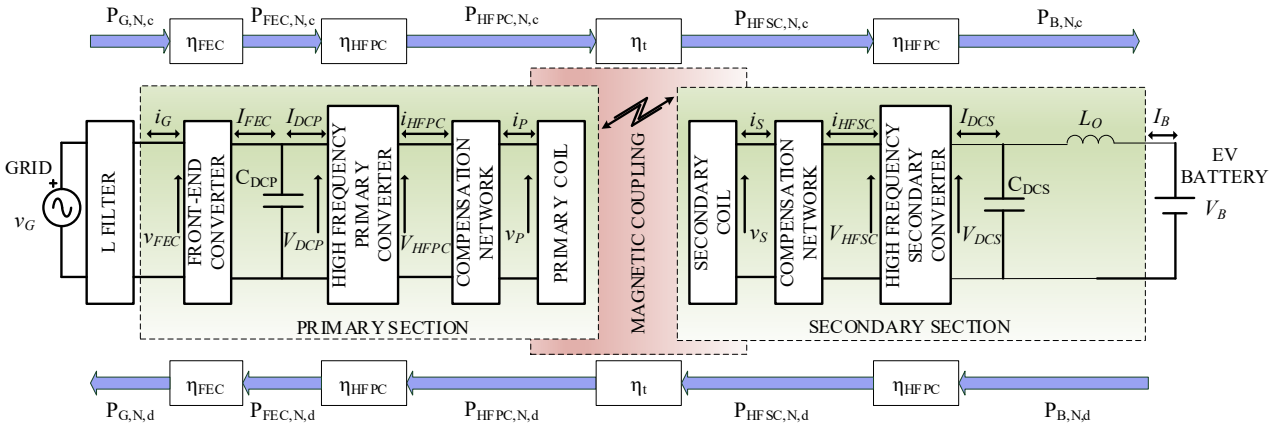

Fig. 3.3 BWV2H with the control rectifier

In a BWV2H application with secondary controlled rectifier, the power flows alternatively from the grid to the battery and vice versa. The construction of the BWV2H with secondary controlled rectifier is shown in Fig. 3.3. The circuit configuration of the primary side of BWV2H with the control converter is the same as the circuit configuration of the primary side of BWV2H with the uncontrolled rectifier and chopper shown in Fig. 3.2. Indeed, on the both arrangement of BWV2H working of primary side converters system are quite similar. Furthermore, it is not required to describe the same thing again up to the i_P current that is circulating in the primary series-compensated coil. The operational detail after the voltage v_S is induce in the secondary coil is presented in the following paragraph.

The voltage v_S induced across the secondary coil forces the circulation of the current i_S, which corresponds with the current i_{HFSC} at the input of the High Frequency Secondary Converter in case of series compensation. The input voltage of the HFSC is v_{HFSC}, while the output is V_{DCS}, which corresponds to the voltage across the capacitor C_{DCS}. The HFSC output current is split between the current flowing through C_{DCS} and the one at the input of the battery

passing through the filter inductance L_O, namely I_B. Finally, the voltage across the battery is V_B. Where HFSC converter work as control rectifier. That can regulate the current across the EV battery while charging and discharging. The FEC, the HFPC, and the HFSC are Bi-directional H-bridge converters.

3.3 Reference technical rules for the connection to the LV electrical utilities

The BWV2H is meant for domestic user connected to LV utility grid. The majority of this kind of users have a single-phase connection, therefore the nominal RMS value of the grid voltage is 230 V [5]. The purpose of this chapter is the design and sizing of the different passive elements and of the power converters: therefore, the peak values of all the involved quantities will be hereafter considered. According to [5], the peak value of the nominal grid voltage $V_{G,N}$ that feeds the BWV2H is

$$\mathrm{V_{G,N}} = 230\sqrt{2}\ V \cong 325\ V \tag{3.3}$$

with maximum and minimum allowed values respectively equal to [18]

$$\begin{aligned} V_{G,m} &= 0.9\ V_{G,N} \cong 293\ V \\ V_{G,M} &= 1.1\ V_{G,N} \cong 358\ V \end{aligned} \tag{3.4}$$

and nominal frequency $f_{G,N}$, as per [5]

$$f_{G,N} = 50\ Hz. \tag{3.5}$$

The typical contractual power of a domestic customer is 3 kW, where the allowable maximum power $P_{G,N}$ and current $I_{G,N}$ withdrawn by the user, hereafter identified as nominal, are

$$\begin{aligned} P_{G,N} &= 3.3\ kW \\ I_{G,N} &= 16\sqrt{2}\ A \cong 22.6\ A. \end{aligned} \tag{3.6}$$

The main purpose of the BWV2H is recharging the battery of the electric vehicle; nevertheless, in certain conditions part of the stored energy can be released towards the domestic loads, with the possibility of injecting it in the grid if it is higher than the overall power absorbed by the home appliance. For this reason, the Italian reference technical rules for the connection to the LV electrical utilities (CEI 0-21) [5] categorizes the BWV2H as an active user, also called a prosumer. It is worth to note that the contractual power sets the limits for the maximum absorbable power, but it is not effective also for the injected one. In addition, [18] requires that the FEC exchanges reactive power with the grid, according to the diagram of Fig.3.4. It is shown that when the injected power is between 0 and 0.2 $P_{G,N}$ the prosumer can behaves either as an inductive or capacitive load, provided that the power factor $\cos(\varphi_G)$ is in

the range of $0.95 < \cos(\varphi_G) < 1$. When injecting active power in the range $0.2\ P_{G,N} < P_G < 0.5\ P_{G,N}$, $\cos(\varphi_G)$ must be maintained at 1. At last, when the power is higher than $0.5\ P_{G,N}$, the user has to inject reactive power of capacitive type, behaving as an inductive load, when the grid voltage exceeds a certain lock-in value (i.e., $1.05\ V_{G,N}$).

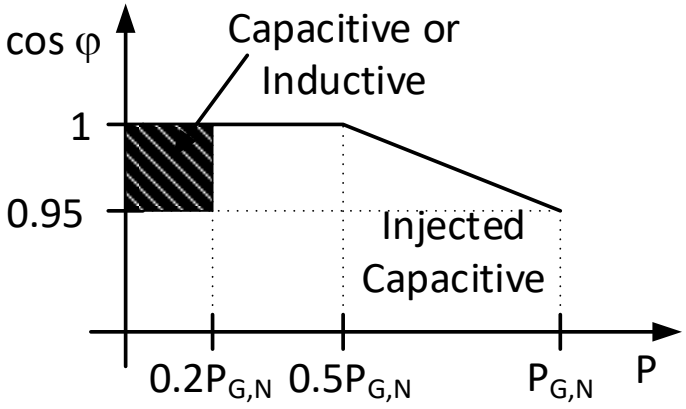

Fig. 3.4 Power factor $\cos(\varphi_G)$ as a function of the active power injected into the grid.

3.4 SAE J2954 Standard

SAE J2954 standard establishes an industry-wide specification that defines acceptable criteria for WPT for light-duty plug-in electric vehicles. It addresses unidirectional charging, whilst bidirectional energy transfer may be evaluated in the future. Four power classes are defined (WPT1, WPT2, WPT3 and WPT4) according to the maximum volt-amps drawn from the grid connection, corresponding to 3.3 kVA, 7.7 kVA, 11.1 kVA, and 22 kVA, respectively. The vertical distance between the ground surface and the lower surface of the on-board coil identifies the WPT Z-class. The study case presented in this chapter refers to a WPT1/Z2 system, with a range of 140-210 mm for the vertical distance.

For WPT1, WPT2 and WPT3 a minimum efficiency of the system is required, measured as the ratio between the active power injected in the battery and the one withdrawal from the grid

$$\eta_{tot} = \frac{P_B}{P_G} \geq 0.80. \qquad (3.7)$$

This value has to be maintained in every condition (i.e. minimum or maximum voltage, power, etc.) when the coils are aligned. Instead, in nominal condition η_{tot} shall be ≥ 0.85 while with coil misalignment it shall be ≥ 0.75. The transmitting coil, which can be either the primary or the secondary in case of bidirectional power transfer, has to be supplied by a voltage with a frequency f_{HF} in the range of 79÷90 kHz having nominal value $f_{HF,N} = 85$ kHz.

3.5 Power sizing of BWV2H

The design of the power converter, together with the series-compensated coil in terms of power sizing of electrical components such as resistance, inductance, capacitance, MOSFETs,

an EV battery, and many more, is taking place. Indeed, the design procedure starts with the constraints imposed by the Italian reference technical rules for domestic low-voltage (LV) utilities grids (CEI 0-21) and the Society of Automotive Engineers (SAE) J2954 for wireless power transfer for electric vehicles. Section 3.2 gives a description of two different converter arrangements for BWV2H and their operation principles. where the primary converter configuration is the same but the secondary converter configuration is not. Indeed, the power sizing process up to the secondary coil is the same, while power differences may be possible. Which are described in the upcoming section.

3.5.1 Power sizing of BWV2H with secondary uncontrolled rectifier and chopper

3.5.1.1 Grid-side and Battery-side Specification

The specifications concerning the input and output of the BWV2H are determined considering the constraints given by CEI 0-21 and the battery, respectively. Being the power flow bidirectional, the involved quantities are worked out both during charging and discharging mode, so that the higher values can be subsequently taken as references for the sizing of the power converters.

The electric vehicle's market is addressing the storage branch towards the Lithium batteries, due to their high energy density and the long lifecycle. This chapter refers to a city car WPT charger, then the nominal battery voltage $V_{B,N}$ is set at 96 V [9] for this case is chosen. Table 3.1 lists six lithium cells, reporting the nominal, minimum and maximum cell voltage V_N, V_m and V_M, respectively, the required number of cells to reach the nominal battery voltage $V_{B,N}$, and the corresponding minimum and maximum battery voltage $V_{B,m}$ and $V_{B,M}$ for each cell type. From these values, in order to carry out a design as general as possible, the minimum and maximum chopper voltage $V_{BC,m}$ and $V_{BC,M}$ have been selected so that they can accommodate all the cell types listed in Table 3.1. Specifically, they can be set respectively at

$$V_{BC,m} = 65\ V$$
$$V_{BC,M} = 120\ V. \qquad (3.8)$$

Table 3.1. Features of lithium cells.

Cell Type	V_N	V_m	V_M	Cells No.	$V_{B,m}$	$V_{B,M}$
$LiFePO_4$	3.2	2.5	3.65	30	75	109
$LiMn_2O_4$	3.7	3.0	4.2	26	78	109
$LiNiMnCoO_2$	3.6	3.0	4.2	27	81	113
$LiCoO_2$	3.6	3.0	4.2	27	81	113
$LiNiCoAlO_2$	3.6	3.0	4.2	27	81	113
Li_2TiO_3	2.4	1.8	2.85	40	72	114

In the case of BWV2H with uncontrolled rectifier and chopper, LiFePO4 cells have been selected as case study [9]. The battery pack is made of thirty LiFePO4 type cells modules connected in series; its overall nominal capacity is 100 Ah. The nominal battery voltage $V_{B,N}$ is 96 V while the working voltage of the battery is between 75 V and 109 V so that the output voltage of the BWV2H must be able to vary in this range. The nominal input and output currents

are 50 A. The current reference to be injected or extracted from the battery is regulated by the Battery Management System (BMS), which lithium battery packs are always equipped with, and whose function is to manage the battery charging process and to monitor its discharging process. The BMS estimates also the SoC of the battery, and according to its level manages the battery operation such as withdrawing power from the vehicle to inject it to the domestic loads, absorbing power from the grid to recharge the battery, or stopping the operations. Accurate SoC estimation is a critical concern for a proper V2G or V2H strategy: to this purpose, several methods have been presented, which can be classified into four main categories according to [10]: direct measurements methods, which estimate the SoC through physical measurements; book-keeping estimations that use battery charging and discharging current as input; model-based methods, where the battery parameters and SoC are estimated using adaptive filters and observers; computer intelligence methods, also called data-driven algorithms [11], which require high computational time and storage size, but can operate without battery model. Direct measurements methods, such as ampere-hour, open-circuit voltage and impedance method, ignore the internal variation [12]. Model-based methods consider the battery as a dynamic system, describing its state-space using battery modelling. A variety of filters and observers, such as the extended Kalman filter [13], unscented Kalman filter [12], sliding-mode observer [14] are introduced to estimate the state variables. Their performance is related to the model accuracy and the signal collection precision. Finally, the data-driven, methods use intelligent algorithms to train the model, as neural networks [15] and fuzzy logic [16]. The selection of the best method for the SoC estimation related to the BWV2H application is out of the scope of this chapter, which aims to size its power stages.

Considering the recommendations of SAE J2954, the total system efficiency η_{tot} has been designated equal to 0.85. The transmission efficiency η_t between the two coils is affected by the alignment, but it is usually above 0.9 [2]. In this work it has been reasonably assumed $\eta_t = 0.92$, as found from previous experimental results [3]. The total converter efficiency η_c is therefore equal to

$$\eta_c \geq \frac{\eta_{tot}}{\eta_t} \cong 0.92. \tag{3.9}$$

As demonstrated in [3], the efficiency of each power converter is similar to the other ones. As a consequence, the hypothesis that all the converters have the same efficiency η_i (with i = FEC, HFPC, HFSC, BC) is plausible; it derives that it has to be equal to

$$\eta_{FEC} = \eta_{HFPC} = \eta_{HFSC} = \eta_{BC} = \sqrt[4]{\eta_c} = 0.98 \tag{3.10}$$

The nominal power absorbed by the domestic user only for EV charging cannot exceed the one prescribed by the contract and highlighted in (3.6). As a consequence, the maximum power $P_{B,N,c}$ that can be injected in the battery during the charging mode is equal to

$$P_{B,N,c} = \eta_{tot} P_{G,N} = 2.8\ kW \tag{3.11}$$

where the subscript N,c states the nominal value during charging mode. The battery absorbs the nominal current $I_{B,N,c}$ in the first stage of the charging process, called constant-current mode [3]. The nominal current absorbed by the battery with the limitation imposed by the domestic contract is then

$$I_{B,N,c} = \frac{P_{B,N,c}}{V_{B,m}} = 37.33\ A \tag{3.12}$$

It can be observed that it is lower than the nominal battery current during the charging mode; this suggests that the charging time will be higher, but at the same time the battery life will be increased as a result of the diminished thermal stresses. While the battery voltage increases from $V_{B,m}$ up to the maximum value $V_{B,M}$, the charging current should remain constant. Nevertheless, the power limitation imposed by the domestic contract forces the current to decrease to keep the power constant. Afterwards, the constant-voltage charging mode begins, where the current gradually decreases and so does the power. Subsequently, this charging mode does not affect the sizing of the BWV2H.

During the discharging mode the vehicle injects the energy stored in its battery towards the domestic loads and, if there is a surplus, in the utility grid. In the extreme case that the home power is null, all the battery power $P_{B,N,d}$, except the losses, is injected in the grid. Its value corresponds to

$$P_{G,N,d} = \eta_{tot} P_{B,N,d} = \eta_{tot} P_{B,N} = 4.63\ kW \tag{3.13}$$

where the subscript N,d states the nominal value during discharging mode. According to CEI 0-21, when injecting power into the grid the power factor must be maintained in the range $0.95 < \cos(\varphi_G) < 1$ by the FEC. In the worst case, i.e. when $\cos(\varphi_{G,m}) = 0.95$ and $V_G = V_{G,m}$, in order to inject the nominal power $P_{G,N,d}$, the maximum grid-side current $I_{G,M,d}$ is:

$$I_{G,M,d} = \frac{2\ P_{G,N,d}}{V_{G,m}\ cos(\varphi_{G,m})} = 33.32\ A. \tag{3.14}$$

The voltages and currents referred to the grid-side and battery-side of the BWV2H are reported in Table 3.2. The calculation of the grid-side and battery-side nominal power and the evaluation of the converters efficiencies allows us to determine the active power flow at each stage of the BWV2H, as represented in Table 3.3.

Table 3.2. Specifications for the grid-side and battery-side BWV2H sizing.

Parameter	Symbol	Value
Grid-side voltage	$V_{G,M}$	358 V
Grid-side current	$I_{G,M}$	33.32 A
Battery-side voltage	$V_{BC,M}$	120 V
Battery-side current (charging mode)	$I_{B,N,c}$	37.4 A

Battery-side current (discharging mode)	$I_{B,N,d}$	50 A

Table 3.3. Power exchanged in the BWV2H stages.

Parameter	$P_{G,N}$	$P_{FEC,N}$	$P_{HFPC,N}$	$P_{HFSC,N}$	$P_{BC,N}$	$P_{B,N}$
Charging mode	3.3 kW	3.23 kW	3.17 kW	2.92 kW	2.86 kW	2.8 kW
Discharging mode	4.63 kW	4.725 kW	4.82 kW	5.24 kW	5.35 kW	5.45 kW

3.5.1.2 Sizing of the Power Converters

The key elements of a WPT system are the coupling coils and the related compensation networks. Nevertheless, the design of their reactive parameters relies upon the operating parameters of the HFPC and HFSC and, more specifically, on the currents and voltage I_{HFPC}, I_{HFSC}, V_{HFPC} and V_{HFSC}. In turn, these values depend upon the grid-side and battery-side sizing values reported in Table 3.2 and upon the operating parameters of the FEC and BC, which set the maximum values of the quantities I_{FEC}, V_{DCP}, I_{BC} and V_{DCS}. The sizing of the coils and compensation networks can be realized only after a first approximation design of the power converters, from the external ones (i.e. FEC and BC) towards the internal ones (i.e. HFPC and HFSC).

3.5.1.2.1 Front-end Converter

The FEC grid-side is connected to the home network through the L_G inductor, whose aim is twofold: decoupling the grid voltage v_G from the FEC medium frequency modulated voltage v_{FEC}, and reducing the harmonic content of the grid current i_G. The value has been set to L_G = 3 mH, which allows to comply with the harmonic current limits established by [33].

The amplitude of the fundamental component $V_{FEC,1}$ that must be available at the FEC input can be derived from the equivalent circuit of Fig. 3.5a and its phasor diagram in Fig.3.5b. The voltage drop on the L_G filter inductor must be counterbalanced by an increase in the fundamental component of the voltage $V_{FEC,1}$. This effect is stronger the more the current I_G is out of phase with respect to voltage V_G, as can be seen from the following expression of $V_{FEC,1}$

$$V_{\mathrm{FEC},1} = \sqrt{(\omega_G L_G I_G)^2 + V_{\mathrm{G}}^2 + 2\omega_{\mathrm{G}} L_{\mathrm{G}} I_{\mathrm{G}} V_{\mathrm{G}} sin(\varphi_G)}. \qquad (3.15.)$$

Analysis of (3.15) shows that $V_{FEC,1}$ is maximum in the condition of maximum grid current and voltage $I_{G,M}$ and $V_{G,M}$, respectively, maximum grid angular frequency $\omega_{G,M}$ = 316.04 rad/s and minimum power factor cos($\varphi_{G,m}$) = 0.95. From these values it comes out $V_{FEC,1,M}$ = 368.88 V. Fig..3.5b shows that the maximum FEC voltage is reached either during charging mode with the current leading the grid voltage or during discharging mode with the current lagging the grid voltage.

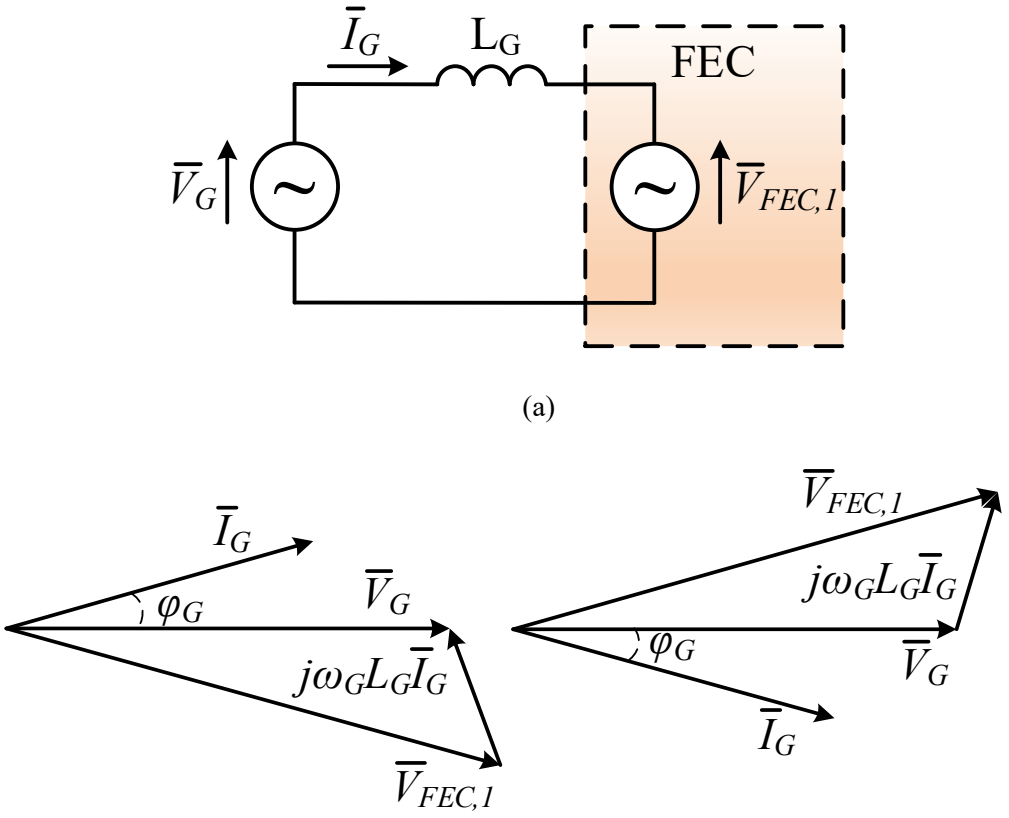

Fig. 3.5 (a) Equivalent circuit of the FEC input and (b) related phasor diagram for maximum $V_{FEC,1}$ during charging and discharging mode, respectively.

The simplified schematic of FEC interfaced to the grid is shown in Fig. 3.6. Assuming ideal switches for the FEC, $V_{FEC,1,M}$ is equal to the C_{DCP} bus voltage V_{DCP}. To guarantee the proper operation of the FEC, the voltage across the capacitor C_{DCP} must be kept as much constant as possible, even though the oscillation induced by the instantaneous power exchanged with the grid cannot be completely eliminated. Assuming a safety margin of 30 V for the proper operation of the BWV2H, the operating V_{DCP} shall be at least equal to 400 V, which is perfectly in accordance with SAE J2954 [6] that establishes

$$V_{DCP} = 450\ V \tag{3.16}$$

By approximating V_{DCP} with its average value and by neglecting the power exchanged with L_G and the power losses in the parasitic resistances, from the instantaneous power balance at the input and at the output of the FEC it derives that the low frequency component of i_{FEC} is mainly constituted by a continuous contribution equal to I_{DCP} and a sinusoidal contribution at twice the grid frequency. Ideally, this contribution flows through C_{DCP} and originates a voltage ripple whose amplitude given by

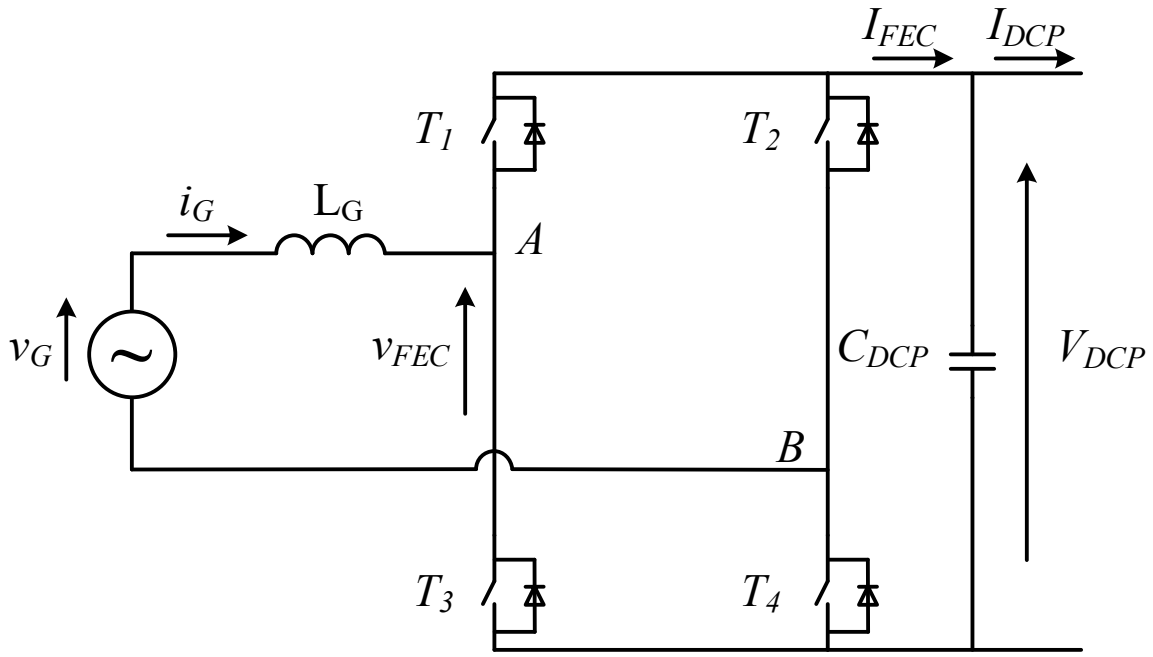

Fig. 3.6 Grid-side of the BWV2H with convention of the current according to charging mode.

$$\Delta V_{DCP} = \frac{1}{2}\frac{V_G I_G sin(\varphi_G)}{2}\frac{1}{V_{DCP}}\frac{1}{C_{DCP}}\frac{1}{2\omega_G}\int_{-\frac{\pi}{2}}^{\frac{\pi}{2}} sin(\theta)d\theta = \frac{P_G}{4\omega_G V_{DCP} C_{DCP}}. \quad (3.17)$$

From (3.17), the value of C_{DCP} can be inferred by considering the worst condition (i.e. nominal grid power $P_{G,N}$ and minimum frequency $\omega_{G,m}$ = 298.45 rad/s) and assuming a reasonable voltage ripple ΔV_{DCP} = 25 V. Therefore, the capacitor to be installed needs to have a capacitance C_{DCP} at least equal to

$$C_{DCP} = 0.25\, mF. \quad (3.18)$$

Since the fundamental frequency of the current i_{DCP} alternating components is equal to $2f_{HF}$, i.e. 1700 times higher than the ripple generated by the grid frequency, the value obtained in (3.18) is sufficient to neglect the high frequency ripple on V_{DCP}. The voltage V_{DCP}, increased by the allowed voltage variation $\Delta V_{DCP}/2$, corresponds to the voltage to be handled by the switches, which results in 462.5 V. Similarly, the maximum voltage $V_{LG,M}$ to whom the filter inductor L_G is subjected is given by

$$V_{LG,M} = V_{DCP} + V_{G,M} = 808\, V \quad (3.19)$$

The maximum current flowing into the switches, in the filter inductor and in the primary DC capacitor is equal to $I_{G,M}$.

3.5.1.2.2 Bi-directional Chopper

The BC works as a buck converter during charging mode and as a boost converter during discharging mode. Then, it is a two-quadrant DC/DC converter with the possibility of reversing only the current. Its task is to regulate the battery current I_B and voltage V_B during the charging and discharging process, according to voltage-current profile supplied by the battery manufacturer. The BC scheme is shown in Fig. 3.7.

As mentioned in (3.8), $V_{BC,M}$ is set at 120 V. Considering the voltage drop across the BC switches, the voltage V_{DCS} across the capacitor C_{DCS} must be slightly higher than $V_{BC,M}$; it is then set at

$$V_{DCS} = 130\,V. \tag{3.20}$$

which corresponds to the maximum voltage handled by the HFSC and BC switches

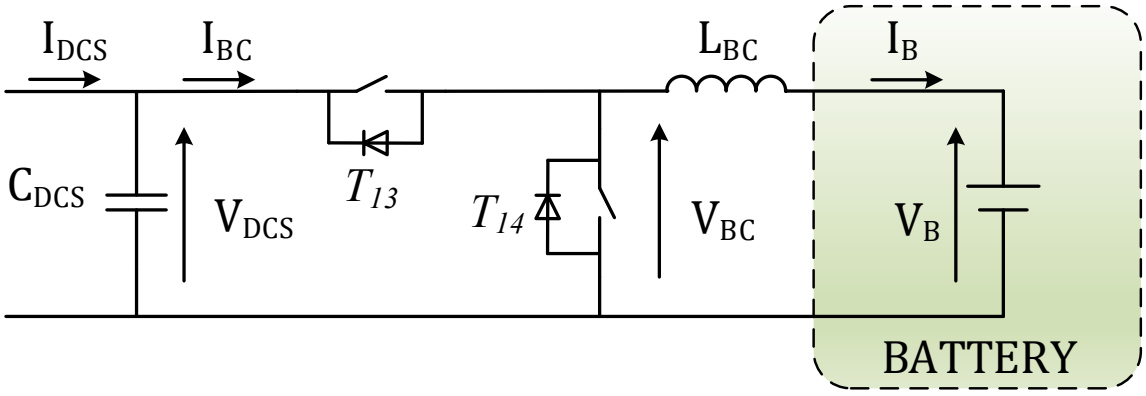

Fig. 3.7 Battery-side of the BWV2H with BC and convention of the current according to charging mode.

The inductance L_{BC} is interposed between the BC and the battery, and its function is twofold: decoupling the modulated voltage V_{BC} from the slowly variable battery voltage V_B and reducing the current oscillations in order to safeguard the battery life. During the constant-voltage charging process mode, the current injected into the battery gradually decreases until it disappears. Therefore, the end of the charging process can be arbitrarily set when the current reduces to 0.05 $I_{B,N,c}$. The same value is then also imposed as the maximum limit of the peak-to-peak oscillation of the current I_B to ensure the continuous conduction of the current throughout the charging process.

Indicating with δ_{BC} the duty cycle of the control signal of the upper switch of the BC, in steady-state conditions and neglecting the parasitic resistance of the inductance L_{BC}, the following relation holds

$$\delta_{BC} = \frac{V_B}{V_{BC}}. \tag{3.21}$$

Assuming continuous conduction operation, the peak-to-peak ripple of the current I_B is given by

$$\Delta I_B = \frac{1}{L_{BC}} V_B (1 - \delta_{BC}) T_{BC} \tag{3.22}$$

where T_{BC} is the switching period of the BC. From (3.21) and (3.22) it can be derived that ΔIB reaches its maximum value when $V_B = V_{BC}/2$ and that, once exceeded this value, ΔI_B decreases as V_B increases. In order to carry out a more general design, the worst case among the cells listed in Table 3.1 is considered. The minimum value of V_B is obtained with Li_2TiO_3 cells and it is still larger than $V_{BC}/2$. As a consequence, the maximum value of ΔI_B is achieved by charging this type of cells, when the battery voltage reaches the minimum value $V_{B,Li2TiO3,m}$ = 72 V. Assuming that the BC switching frequency is the same of both the HFPC and the HFSC, the current oscillation is maintained within the desired limits for L_{BC} choosing the minimum value of

$$L_{BC} = \frac{V_{B,Li_2TiO_3,m}(1 - \delta_m) T_{BC}}{0.05\, I_{B,N,d}} = 151\ \mu H \tag{3.23}$$

where δ_m is the minimum duty cycle of the BC given by the ratio $V_{B,Li2TiO3,m}/V_{DCS}$. The maximum current flows in L_{BC} during the battery discharging and is equal to $I_{B,N,d}$, while the maximum voltage applied to its terminals is $V_{BC,M}$.

The sizing of the DC secondary capacitor C_{DCS} starts by assessing the current flowing through it. The average value of the current I_{BC} is easily derived considering the DC bus voltage V_{DCS} and the power exchanged by the BC during the charging and the discharging mode, reported in Table 3.3.

$$\begin{aligned} I_{BC,N,c} &= \frac{P_{BC,N,c}}{V_{DCS}} = 22.0\ A \\ I_{BC,N,d} &= \frac{P_{BC,N,d}}{V_{DCS}} = 41.2\ A, \end{aligned} \tag{3.24}$$

The average value of I_{BC} is equal to the direct component of current i_{DCS}, which is a rectified sinewave whose amplitude during charging and discharging mode is respectively

$$\begin{aligned} I_{DCS,N,c} &= \frac{\pi}{2} I_{BC,N,c} = 34.5\ A \\ I_{DCS,N,d} &= \frac{\pi}{2} I_{BC,N,d} = 64.7\ A \end{aligned} \tag{3.25}$$

and whose frequency is twice the switching one, i.e. 170 kHz. The minimum sizing value of the capacitor C_{DCS} can be obtained hypothesizing that it is flown by the alternate component of I_{DCS} and considering the worst operating conditions, i.e. minimum switching frequency $\omega_{HF,m}$ = 79 kHz and maximum current $I_{DCS,N,d}$. By imposing the voltage ripple across C_{DCS} is $\Delta V_{DCS} = 0.1 V_{DCS}$, it results

$$C_{DCS} = \frac{1}{\omega_{HF,m}\Delta V_{DCS}} 2 \int_{asin\left(\frac{2}{\pi}\right)}^{\frac{\pi}{2}} I_{DCS,N,d} \left[sin(\theta) - \frac{2}{\pi}\right] d\theta = \frac{I_{DCS,N,d}}{\omega_{HF,m}\Delta V_{DCS}} 2 \left[\sqrt{1 - \frac{4}{\pi^2}} - 1 + \frac{2}{\pi} asin\left(\frac{2}{\pi}\right)\right] = 4.22\ \mu F. \quad (3.26)$$

3.5.1.2.3 High-Frequency Primary Converter

The HFPC is a H-bridge converter, as shown in Fig. 3.8. The generation of the high frequency voltage v_{HFPC} required during charging mode does not allow the utilization of the PWM technique to regulate the amplitude of its fundamental component, since this technique would lead to excessively high switching frequencies. As a result, during the charging mode of the BWV2H, the HFPC is controlled with the phase shift technique, which allows to obtain a semi-square wave voltage whose fundamental component has frequency equal to the switching frequency of the HFPC, set at $f_{HF,N}$, and amplitude given by

$$V_{HFPC,1} = \frac{4}{\pi} V_{DCP} sin\left(\frac{\sigma}{2}\right), \quad (3.27)$$

where σ is the delay angle between control signals of T_5 and T_7 with respect to those of T6 and T8. The maximum value of the fundamental voltage component is reached when the control signals are delayed by π. Neglecting the voltage drop on the switches and the ripple of V_{DCP}, the voltage at the HFPC output is a square wave whose fundamental component amplitude is

$$V_{HFPC,1,M} = \frac{4}{\pi} V_{DCP} = 573\ V. \quad (3.28)$$

3.5.1.2.4 High-Frequency Secondary Converter

During charging mode, the easiest control solution for the HFSC is to leave all the switches off so that it acts as a diode rectifier. In such an operation mode, the alternated voltage v_{HFSC} depicted in Fig. 3.9 is a square wave voltage in phase with the current i_{HFSC} and with amplitude of the fundamental component of voltage given by

$$V_{HFSC,1,M} = \frac{4}{\pi} V_{DCS} = 165.5\ V \quad (3.29)$$

When the BWV2H operates in battery discharging mode, the HFPC works as a diode rectifier and the HFSC works as an inverter. Maintaining the same control techniques described in Section 3.5.1.2.3, the voltage v_{HFSC} is a semi-square wave voltage with frequency f_{HF} and fundamental component equal to

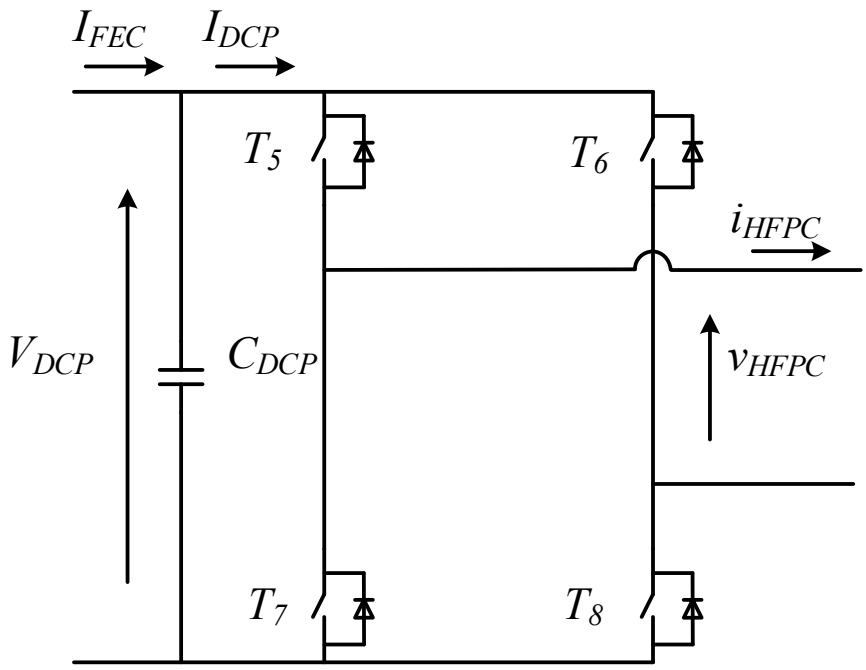

Fig. 3.8 Schematics of the HFPC and convention of the current according to charging mode.

$$V_{HFSC,1} = \frac{4}{\pi} V_{DCS} sin\left(\frac{\sigma}{2}\right), \tag{3.30}$$

whose maximum value corresponds to (3.29). During discharging mode, the voltage v_{HFPC} is a square wave voltage, in phase with the current i_{HFPC} and with amplitude of the fundamental component equal to (3.28). The H-bridge schematics of HFSC is shown in Fig. 3.9, where the current direction is drawn according to the charging mode.

3.5.1.2.5 Sizing of the Coupling Coils and Compensation Networks

Considering the necessity of a symmetrical behavior for BWV2H in both the power flow directions, the series compensation results to be the preferred one in both the primary and secondary side [3]. This compensation technique forces the current flowing through the coils to be nearly sinusoidal, because the series of the resonant capacitors and the coils self-inductances behave as short circuits at the nominal frequency $f_{HF,N}$. As a consequence, the voltage induced in the primary and secondary coils are ideally equal to v_{HFPC} and v_{HFSC}, respectively. These features allow us to simplify the schematics of the BWV2H by expressing the voltages v_{HFPC} and v_{HFSC} and the induced voltages across the coils as ideal voltage sources. This leads to circuital scheme of Fig. 3.10, where R_P and R_S represent the parasitic resistances of the coils.

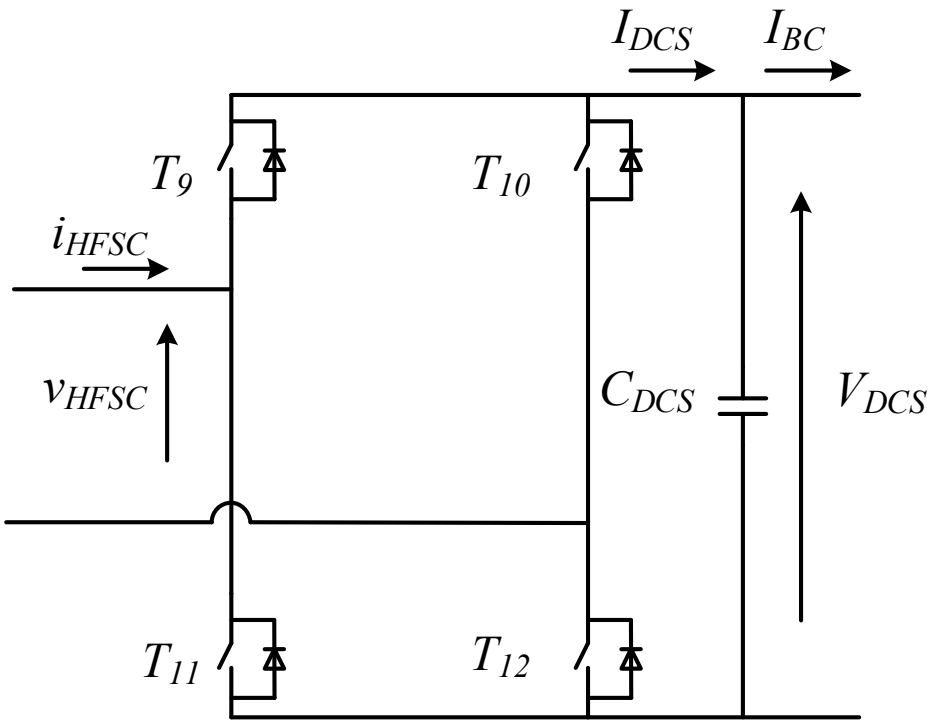

Fig. 3.9 Schematics of the HFSC and convention of the current according to charging mode

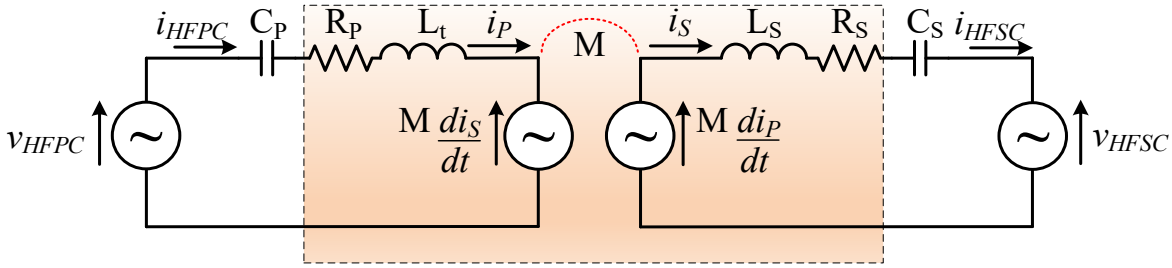

Fig. 3.10 Equivalent diagram of S-S coupling coil.

During battery charging mode, the presence of the parasitic resistances requests the HFPC to generate a voltage fundamental component $V_{HFPC,1}$ higher than the one induced across the primary coil. In the same way, the voltage fundamental component $V_{HFSC,1}$ is lower than the one induced across the secondary coil. By defining the primary and secondary coil efficiency as $\eta_{t,P}$ and $\eta_{t,S}$, respectively, during the charging mode the active power flowing from the HFPC output to the secondary coil is given by the first of (3.31) while the second gives the active power at the input of the HFSC,

$$P_{HFPC,c} = \frac{V_{HFPC,1}I_P}{2} = \frac{1}{2}\frac{\omega_{HF}MI_SI_P}{\eta_{t,P}}$$
$$P_{HFSC,c} = \frac{V_{HFSC,1}I_S}{2} = \frac{1}{2}\omega_{HF}MI_SI_P\eta_{t,S}. \quad (3.31)$$

From (3.31), the transmission efficiency can be derived as follows

$$\eta_t = \frac{P_{HFSC,c}}{P_{HFPC,c}}. \tag{3.32}$$

Considering two identical coils, the transmission efficiency can be equally divided between primary and secondary coil

$$\eta_{t,P} = \eta_{t,S} = \sqrt{\eta_t}. \tag{3.33}$$

From (3.33), the voltage fundamental component $V_{HFPC,1}$ and $V_{HFSC,1}$ during battery charging mode becomes

$$\begin{aligned} V_{HFPC,1} &= \frac{\omega_{HF,N} M I_{HFSC}}{\sqrt{\eta_t}} \\ V_{HFSC,1} &= \omega_{HF,N} M I_{HFPC} \sqrt{\eta_t}. \end{aligned} \tag{3.34}$$

where $\omega_{HF,N}=2\pi f_{HF,N}$ is the nominal angular frequency of the HFPC. For battery discharging mode, dual equations can be written and are therefore omitted in this chapter.

Assuming to charge the battery at the power $P_{B,N,c}$, the power at the input of the HFSC needs to be $P_{HFSC,N,c}$, as stated in Table 3.3; therefore, the amplitude of current i_{HFSC} corresponds to

$$I_{HFSC,N,c} = \frac{2P_{HFSC,N,c}}{V_{HFSC,1,M}} = 35.2\ A. \tag{3.35}$$

In order for this current to actually flow in the secondary coil, the induced voltage across the primary coil, increased of the voltage drop across R_P, needs to be lower than the maximum fundamental component of the voltage v_{HFPC}. From (3.34), the following inequality can be derived

$$M \leq \frac{V_{HFPC,1,M}}{I_{HFSC,N,c}\ \omega_{HF,M}} \sqrt{\eta_t} = 27.6\ \mu H. \tag{3.36}$$

Eq. (3.36) states the maximum value for the mutual inductance between the two coupling coils, determined considering the maximum angular frequency $\omega_{HF,M}$.

The value established in (3.36) needs to be verified also for the discharging mode. The power at AC side of the HFPC is $P_{HFSC,N,d}$, as expressed in Table 3.3. The nominal amplitude of current $i_{HFPC,d}$ is

$$I_{HFPC,N,d} = \frac{2P_{HFPC,N,d}}{V_{HFPC,1,M}} = 16.8\ A.. \tag{3.37}$$

In order for this current to actually flow in the primary coil, the induced voltage across the secondary coil, increased of the voltage drop on R_S, needs to be lower than the maximum fundamental component of the voltage v_{HFSC}. Using the dual equation of (3.34) for the discharging mode, the following inequality is derived

$$M \leq \frac{V_{HFSC,1,M}}{I_{HFPC,N,d}\ \omega_{HF,M}}\sqrt{\eta_t} = 16.7\ \mu H \tag{3.38}$$

Eq. (3.38) is stricter than (3.36); hence, the value of M is fixed at

$$M = 16.5\ \mu H. \tag{3.39}$$

Once set the value of M, it is possible to conclude the determination of the current flowing into the coils in both charging and discharging mode, and then size the switches that form the HFPC and HFSC. The worst condition is verified when the frequency is minimum, since higher currents are necessary to obtain the required induced voltages to transfer the predetermined amount of power.

During battery charging mode, the voltage fundamental component of v_{HFPC} in correspondence of minimum operating frequency is

$$V_{HFPC,1,m,c} = \frac{\omega_{HF,m} M I_{HFSC,N,c}}{\sqrt{\eta_t}} = 300\ V. \tag{3.40}$$

Consequently, to transfer the power $P_{HFPC,N,c}$, the amplitude of the current supplied by the HFPC has to be

$$I_{HFPC,N,c} = \frac{2P_{HFPC,N,c}}{V_{HFPC,1,m,c}} = 21.1\ A. \tag{3.41}$$

Similarly, in discharging mode the voltage fundamental component of v_{HFSC} in correspondence of minimum operating frequency is

$$V_{HFSC,1,m,d} = \frac{\omega_{HF,m} M I_{HFPC,N,d}}{\sqrt{\eta_t}} = 143.5\ V. \tag{3.42}$$

Consequently, to transfer the power $P_{HFSC,N,d}$, the amplitude of the current supplied by the HFSC has to be

$$I_{HFSC,N,d} = \frac{2P_{HFSC,N,d}}{V_{HFSC,1,m,d}} = 72.9\ A. \tag{3.43}$$

By comparison between (3.37) and (3.41) and between (3.35) and (3.43) it can be observed that the primary coil, the primary resonant capacitor and the switches of the HFPC

have to be sized according to the current $I_{HFPC,N,c}$, whilst the secondary coil, the secondary resonant capacitor and the switches of the HFSC have to be sized for the current $I_{HFSC,N,d}$.

Considering a coupling coefficient k = 0.12, where $k = M/\left(\sqrt{L_P L_S}\right)$, in-between the minimum and maximum value established by SAE J2954, and assuming the same shape for the two coils, the self-inductance results to be

$$L_P = L_S = \frac{M}{k} = 162\ \mu H \tag{3.44}$$

The resonant capacitors are sized according to the nominal frequency $f_{HF,N}$

$$C_P = C_S = \frac{1}{\omega_{HF,N}^2 L_P} = \frac{1}{\omega_{HF,N}^2 L_S} = 21.7\ nF. \tag{3.45}$$

Each coil is subject to a voltage given by the sum of the voltage drop on the self-inductance and the voltage induced by the current flowing through the other coil. With the series resonance topology, the two voltage contributions are π/2 out-of-phase one respect to the other. The nominal voltage on the coils is then equal to

$$\begin{aligned} V_{LP,N} &= \sqrt{\left(\omega_{HF,N} L_P I_{HFPC,N,c}\right)^2 + \left(\omega_{HF,N} M I_{HFSC,N,c}\right)^2} = 1.85\ kV \\ V_{LS,N} &= \sqrt{\left(\omega_{HF,N} L_S I_{HFSC,N,d}\right)^2 + \left(\omega_{HF,N} M I_{HFPC,N,d}\right)^2} = 6.3\ kV.. \end{aligned} \tag{3.46}$$

The voltage across the resonant capacitors ideally corresponds to the voltage drop across the self-inductances of the coils, because of the series resonance. The nominal value for the primary capacitor is reached during the charging process, whilst the one across the secondary capacitor is reached during the discharging process:

$$\begin{aligned} V_{CP,N} &= \frac{I_{HFPC,N,c}}{\omega_{HF,N} C_P} = 1.82\ kV \\ V_{CS,N} &= \frac{I_{HFSC,N,d}}{\omega_{HF,N} C_S} = 6.3\ kV. \end{aligned} \tag{3.47}$$

3.5.2 Power sizing of BWV2H with secondary controlled rectifier

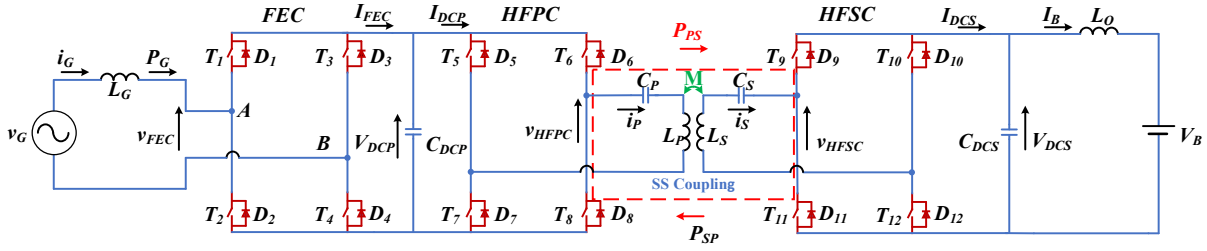

Fig. 3.11. Schematics of the WPT with both bridge are active control.

3.5.2.1 Power sizing of BWV2H Grid-side and Battery-side Specification with secondary controlled converter

It was specified in section 3.5.1.1, the input and output specifications of BWV2H are chosen, the higher values can be subsequently taken as references for the sizing of the power converters as per the constraints given by CEI 0-21 and the battery, respectively.

Electric vehicle storage uses lithium batteries for their high energy density and long lifetime. The nominal battery voltage for the WPT city car $V_{B,N}$ is set at 118 V for this case and is chosen in this section. Table 3.1 already gives a precise description of six lithium cells. Here in Table 3.4, we report the nominal, minimum, and maximum cell voltages V_N, V_m and V_M, respectively for $LiFePO_4$ battery, the required number of cells to reach the nominal battery voltage $V_{B\_LiFePO4,N}$=118 V, and the corresponding minimum and maximum battery voltages $V_{B\_LiFePO4,m}$ and $V_{B\_LiFePO4,M}$ for $LiFePO_4$ only. The detailed specification of $LiFePO_4$ for charging through the BMS was mentioned in section 3.5.1.1. This can also be taken into account in this section.

$$V_{B\_m} = 92\ V$$
$$V_{B,M} = 135\ V. \qquad (3.48)$$

As filter inductor have some drop, there for the voltage at the secondary DC bus capacitor C_{DCS}.is higher then Maximum batter voltage $V_{B,M.}$ There for maximum secondary DC voltage assume as $V_{DCS,M}$= 160 V.

Table 3.4. Features of lithium cells with secondary control converter.

Cell Type	V_N	V_m	V_M	Cells No.	$V_{B\_,m}$	V_{B_M}
$LiFePO_4$	3.2	2.5	3.65	37	92	135

The total system efficiency η_{tot}, transmission efficiency $\eta_{t,}$ and converter efficiency η_c are 0.85, 0.92, and 0.92, respectively, already mentioned in section 3.5.1.1. As demonstrated in [4], the efficiency of each power converter is similar to the other ones. As a consequence, the hypothesis that all the converters have the same efficiency η_i (with i = FEC, HFPC, HFSC) is plausible; it derives that it has to be equal to

$$\eta_{FEC\_C} = \eta_{HFPC\_C} = \eta_{HFSC\_C} = \sqrt[3]{\eta_c} = 0.97 \qquad (3.49)$$

The maximum power $P_{B,N,c}$ that can be injected into battery, while charging is 2.8kW. The battery absorbs the nominal current $I_{B,N,c}$ in the first stage of the charging process, called constant-current mode [4]. Relation (3.12) is used to calculate the nominal current absorbed by the battery, i.e., 30.48A. The charging current is lower than the nominal current 50A, there for the battery charging time will be higher and fewer thermal stresses on battery that causes longer battery life. While the battery voltage increases from $V_{B,m}$ up to the maximum value $V_{B,M}$, the

charging current should remain constant. Nevertheless, the power limitation imposed by the domestic contract forces the current to decrease to keep the power constant. Afterwards, the constant-voltage charging mode begins, where the current gradually decreases and so does the power. Subsequently, this charging mode does not affect the sizing of the BWV2H.

During the discharging mode, the vehicle injects the energy stored in its battery towards the domestic loads and, if there is a surplus, into the utility grid. In the extreme case that the home power is null, all the battery power $P_{B,N,d}$, except the losses, is injected into the grid. Its value corresponds to

$$P_{G,N,d} = \eta_{tot} P_{B,N,d} = \eta_{tot} P_{B,N} = 5.73\ kW \qquad (3.50)$$

To inject the nominal power $P_{G,N,d}$ into the grid, the maximum grid-side current $I_{G,M,d}$ =41.3 A is obtain by using the relation (3.14) in worst case when $\cos(\varphi_{G,m}) = 0.95$ and $V_G = V_{G,m}$.

The voltages and currents referred to the grid-side and battery-side of the BWV2H are reported in Table 3.5. The calculation of the grid-side and battery-side nominal power and the evaluation of the converters efficiencies allows us to determine the active power flow at each stage of the BWV2H, as represented in Table 3.6.

Table 3.5. Specifications for the grid-side and battery-side BWV2H sizing with secondary control converter.

Parameter	Symbol	Value
Grid-side voltage	$V_{G,M}$	358 V
Grid-side current	$I_{G,M}$	41.3 A
Battery-side voltage	$V_{B\_,M}$	135 V
Battery-side current (charging mode)	$I_{B,N,c}$	30.48 A
Battery-side current (discharging mode)	$I_{B,N,d}$	50 A

Table 3.6. Power exchanged in the BWV2H stages with secondary control converter.

Parameter	$P_{G,N}$	$P_{FEC,N}$	$P_{HFPC,N}$	$P_{HFSC,N}$	$P_{B,N}$
Charging mode	3.3 kW	3.2 kW	3.1 kW	2.85 kW	2.8 kW
Discharging mode	5.73 kW	5.84 kW	6.0 kW	6.54 kW	6.75 kW

3.5.2.2 Sizing of the Power Converters with secondary control rectifier

The coupling coils and associated compensation networks are essential components of a WPT system. Nevertheless, the currents and voltage I_{HFPC}, I_{HFSC}, V_{HFPC} and V_{HFSC} play role in the design of their reactive characteristics. The maximum values of I_{FEC}, and V_{DCP} are determined by the operating parameters of the FEC, which in turn are dependent on the grid-side and battery-side size values shown in Table 3.5. After a first approximation design of the power converters, the size of the coils and compensation networks may be accomplished (i.e. FEC, HFPC and HFSC).

3.5.2.2.1 Front-end Converter with secondary control rectifier

As in the case of BWV2H with the secondary control rectifier arrangement, primary side converters FEC and HFPC operation, and converter elements are same as in the case of BWV2H with the secondary uncontrolled rectifier shown in section 3.2. The FEC grid-side is connected to the home network via the L_G inductor; the value has been set to L_G = 3 mH, which is the same as the L_G value chosen in Section 3.5.1.2.1, allowing compliance with the harmonic current limits established by [17].

The amplitude of the fundamental component $V_{FEC,1}$ that derived from the equivalent circuit of Fig. 3.5a and its phasor diagram in Fig.3.5b. And equation (3.15) can be utilized to calculate the maximum $V_{\mathrm{FEC},1}$ in the condition of maximum grid current and voltage $I_{G,M}$ and $V_{G,M}$, respectively, maximum grid angular frequency $\omega_{G,M}$ = 316.04 rad/s and minimum power factor cos($\varphi_{G,M}$) = 0.95. From these values it comes out $V_{FEC,1,M}$= 368.88 V.

The simplified schematic of FEC interfaced to the grid is shown in Fig. 3.6. The $V_{FEC,1,M}$ is equal to the C_{DCP} bus voltage V_{DCP}. As same as in section 3.5.1.2.1, the safety margin of $V_{FEC,1,M}$ is chosen 30 V, the operating V_{DCP} shall be at least equal to 400 V, which is perfectly in accordance with SAE J2954 [5] that establishes V_{DCP}.=450 V.

By approximating V_{DCP} with its average value and by neglecting the power exchanged with L_G and the power losses in the parasitic resistances, from the instantaneous power balance at the input and at the output of the FEC it derives that the low frequency component of i_{FEC}. is mainly constituted by a continuous contribution equal to I_{DCP} and a sinusoidal contribution at twice the grid frequency. Ideally, this contribution flows through C_{DCP} and originates a voltage ripple.

From (3.17), the value of C_{DCP} can be inferred by considering the worst condition (i.e. nominal grid power $P_{G,M}$ and minimum frequency $\omega_{G,M}$ = 298.45 rad/s) and assuming a reasonable voltage ripple ΔV_{DCP} = 25 V. Therefore, the capacitor to be installed needs to have at least a capacitance $C_{DCP} = 0.25mF$.

High frequency ripple on V_{DCP} ignored by using the value found for C_{DCP} in (3.18), since the fundamental frequency of the alternating components of the current i_{DCP} is equal to $2f_{HF}$, i.e. 1700 times higher than the ripple generated by the grid frequency. The voltage V_{DCP}, increased by the allowed voltage variation $\Delta V_{DCP}/2$, corresponds to the voltage to be handled by the switches, which results in 462.5 V. Similarly, the maximum voltage $V_{LG,M} = 808\,V$ in (3.19) to whom the filter inductor L_G is subjected. The maximum current flowing into the switches, in the filter inductor and in the primary DC capacitor is equal to $I_{G,M}$.

3.5.1.2.2 High-Frequency Primary Converter and High-Frequency Secondary Converter with secondary control rectifier

The HFPC and HFSC are H-bridge converter, as shown in Fig. 3.8 and 3.9. During the charging and discharging mode of the BWV2H, the HFPC and HFSC are controlled with the

phase shift technique i.e., dual phase shift (DPS). Indeed, DPS is the controlled method by which we regulate the HFPC and HFSC with an equal internal phase shift angle, that can represent in Equations (3.27) band (3.28), which allows to obtain a semi-square wave voltage whose fundamental component has frequency equal to the switching frequency of the HFPC and HFSC, set at $f_{HF,N}$. The maximum value of the fundamental voltage component is reached when the control signals are delayed by π. Neglecting the voltage drop on the switches and the ripple of V_{DCP}, the voltage at the HFPC output is a square wave whose fundamental component amplitude $V_{HFPC,1,M} = 573\ V$. obtain from (3.28), when $V_{DCP} = 450\ V$ and the voltage at the HFPC input is a square wave whose fundamental component amplitude $V_{HFSC,1,M} = 203\ V$. obtain from (3.29), when $V_{DCS} = 160\ V$.

3.5.1.2.3 Sizing of the Coupling Coils and Compensation Networks with secondary control rectifier

Considering the necessity of a symmetrical behavior for BWV2H in both the power flow directions, the series compensation results to be the preferred one in both the primary and secondary side [3]. This compensation technique forces the current flowing through the coils to be nearly sinusoidal, because the series of the resonant capacitors and the coils self-inductances behave as short circuits at the nominal frequency $f_{HF,N}$. As a consequence, the voltage induced in the primary and secondary coils are ideally equal to v_{HFPC} and v_{HFSC}, respectively. These features allow us to simplify the schematics of the BWV2H by expressing the voltages v_{HFPC} and v_{HFSC} and the induced voltages across the coils as ideal voltage sources. This leads to circuital scheme of Fig. 3.10, where R_P and R_S represent the parasitic resistances of the coils.

By defining the primary and secondary coil efficiency as $\eta_{t,P}$ and $\eta_{t,S}$, respectively, during the charging mode the active power flowing from the HFPC output to the secondary HFSC. Assuming to charge the battery at the power $P_{B,N,c}$, the power at the input of the HFSC needs to be $P_{HFSC,N,c}$, as stated in Table 3.6; therefore, the amplitude of current i_{HFSC} is I_{HFSC} = 28 A obtain by using the equation (3.35). In order for this current, that actually flow in the secondary coil, the induced voltage across the primary coil, increased of the voltage drop across R_P, needs to be lower than the maximum fundamental component of the voltage v_{HFPC}. From (3.34), and (3.35) the mutual inductance $\mathrm{M} \leq 34.6\ \mu H$ is derived.

The value established in (3.36) needs to be verified also for the discharging mode. The power at AC side of the HFPC is $P_{HFSC,N,d}$, as expressed in Table 3.6. The nominal amplitude of current $i_{HFPC,d}$ is $I_{HFPC,N,d} = 21\ A$ obtain by using the equation (3.37).

In order for this current, that actually flow in the primary coil, the induced voltage across the secondary coil, increased of the voltage drop on R_S, needs to be lower than the maximum fundamental component of the voltage v_{HFSC}. Using equations (3.34) and (3.37) for the discharging mode, the mutual inductance $\mathrm{M} \leq 16.4\ \mu H$ is derived. Eq. (3.38) is stricter than (3.36); hence, the value of $M = 16.5\ \mu H$ is fixed.

Once set the value of M, it is possible to conclude the determination of the current flowing into the coils in both charging and discharging mode, and then size the switches that form the

HFPC and HFSC. The worst condition is verified when the frequency is minimum, since higher currents are necessary to obtain the required induced voltages to transfer the predetermined amount of power.

During battery charging mode, the fundamental component of voltage v_{HFPC} in correspondence of minimum operating frequency is $V_{HFPC,1,m,c} = 239\ V$ is obtain from Equation (3.40). Consequently, to transfer the power $P_{HFPC,N,c}$, the amplitude of the current supplied by the HFPC has to be $I_{HFPC,N,c} = 25.9\ A$. It is obtained from Equation (3.41) by putting the value of $V_{HFPC,1,m,c} = 239\ V$ and $P_{HFPC,N,c}$ from Table 3.6.

Similarly, in discharging mode, the fundamental component of voltage v_{HFSC} in correspondence of minimum operating frequency is $V_{HFSC,1,m,d} = 179.5\ V$. It is obtained by putting the value of $I_{HFPC,N,c} = 25.9\ A$ in Equation (3.42). Consequently, to transfer the power $P_{HFSC,N,d}$, the amplitude of the current supplied by the HFSC has to be $I_{HFSC,N,d} = 72.9\ A$. It is obtained from Equation (3.43) by putting the value of $V_{HFSC,1,m,d} = 179.5\ V$ and $P_{HFSC,N,d}$ from Table 3.6.

By comparison between (3.37) and (3.41) and between (3.35) and (3.43) it can be observed that the primary coil, the primary resonant capacitor and the switches of the HFPC have to be sized according to the current $I_{HFPC,N,c}$, whilst the secondary coil, the secondary resonant capacitor and the switches of the HFSC have to be sized for the current $I_{HFSC,N,d}$.

Considering a coupling coefficient k = 0.12, where $k = M/\left(\sqrt{L_P L_S}\right)$, in-between the minimum and maximum value established by SAE J2954, and assuming the same shape for the two coils, the self-inductance results to be $L_P = L_S = \frac{M}{k} = 162\ \mu H$. The resonant capacitors are sized according to the nominal frequency $f_{HF,N}$ is $C_P = C_S = \frac{1}{\omega_{HF,N}^2 L_P} = \frac{1}{\omega_{HF,N}^2 L_S} = 21.7\ nF$.

Each coil is subject to a voltage given by the sum of the voltage drop on the self-inductance and the voltage induced by the current flowing through the other coil. With the series resonance topology, the two voltage contributions are π/2 out-of-phase one respect to the other. The nominal voltage on the coils is then equal to $V_{P,N} = 2.25\ kV$ and $V_{S,N} = 6.3\ kV$. Obtained by relation (3.46).

The voltage across the resonant capacitors ideally corresponds to the voltage drop across the self-inductances of the coils, because of the series resonance. The nominal value for the primary capacitor is reached during the charging process, whilst the one across the secondary capacitor is reached during the discharging process are $V_{CP,N} = 2.24\ kV$ and $V_{CS,N} = 6.3\ kV$. It is obtained relation (3.47).

3.5.1.2.4 Sizing of the Coupling Coils and Compensation Networks with secondary control rectifier

V_{DCS} is set at 160 V. Considering the voltage drop across the LPF, the voltage V_{DCS} across the capacitor C_{DCS} must be slightly higher than $V_{B\_C,M}$. The inductance L_O is interposed between

the HFSC and the battery, and its function is twofold: decoupling the modulated voltage V_{DCS} from the slowly variable battery voltage V_B and reducing the current oscillations in order to safeguard the battery life. During the constant-voltage charging process mode, the current injected into the battery gradually decreases until it disappears. Therefore, the end of the charging process can be arbitrarily set when the current reduces to 0.13 $I_{B,N,d}$. The same value is then also imposed as the maximum limit of the peak-to-peak oscillation of the current I_B to ensure the continuous conduction of the current throughout the charging process.

Assuming continuous conduction operation, the peak-to-peak ripple of the current I_B is given by

$$L_O = V_{LO} \frac{T_B}{\Delta i_B} \tag{3.51}$$

where T_B is the switching period of the HFSC. $i_{B,N,d}$=42.2 A ripple of inductor current is chosen 13 %, worst condition of switching frequency is 79kHz. $V_{LO} = 68\,V$ when we choose voltage across battery have minimum i.e., 75V. As the 13% ripple are in the tolerance rage, the filter inductor $L_O = 156.9\,\mu H$ is achieve. There for we chose the final value of L_O is same as the previous case i.e., $151\,\mu H$.

The sizing of the DC secondary capacitor C_{DCS} starts by assessing the current flowing through it. The average value of the current I_B is easily derived considering the DC bus voltage V_{DCS} and the power exchanged by the battery during the charging and the discharging mode, reported in Table 3.6. The charging and discharging current of the battery $I_{B,N,c} = 17.5\,A$ and $I_{B,N,d} = 42.2\,A$ obtained by considering the data from Table 3.5 and 3.6 in Equation (3.24).

The average value of I_B is equal to the direct component of current i_{DCS}, which is a rectified sinewave whose amplitude during charging and discharging mode are $I_{DCS,N,c} = 27.49\,A$ and $I_{DCS,N,d} = 66.28\,A$, respectively from equation (3.25). and whose frequency is twice the switching one, i.e. 170 kHz. The minimum sizing value of the capacitor C_{DCS} can be obtained hypothesizing that it is flown by the alternate component of I_{DCS} and considering the worst operating conditions, i.e. minimum switching frequency $\omega_{HF,m}$ = 79 kHz and maximum current $I_{DCS,N,d}$. By imposing the voltage ripple across C_{DCS} is $\Delta V_{DCS} = 0.1 V_{DCS}$, it results $C_{DCS} = 3.51\,\mu F$ by using equation (3.26).

3.6 Result and Discussion

This Section presents some considerations concerning the sizing of both the BWV2H system such as, the secondary uncontrolled rectifier together with the chopper, and secondary controlled rectifier, the simulations results obtained through the MATLAB software. The sizing values of the coupling coil and compensation networks are resumed in Table 3.7, and 3.9, while Table 3.8 and 3.10 reports the sizing values of the main components of the BWV2H system such as, the secondary uncontrolled rectifier together with the chopper, and secondary controlled rectifier, respectively It can be observed that in the secondary side a higher current

can flow. This leads to higher voltage across both the secondary reactive elements, i.e. L_S and C_S, as illustrated in Table 3.7 and 3.9. The current values selected for sizing purposes are the highest between the charging and discharging mode in each stage. The current on the secondary side is strongly related to the sizing of the reactive elements, in particular of the mutual inductance M (and, consequently, of the self-inductances and the resonating capacitor). A higher value of M leads to higher induced voltage and, therefore, lower current to ensure the requested power transfer.

Table 3.7. Sizing values of the BWV2H coupling coils and compensation networks for secondary uncontrolled rectifier together with chopper.

Element	Symbol	Value	Voltage [kV]	Current [A]
Mutual inductance	*M*	*16.5 μH*	-	-
Primary coil self-inductance	L_P	*162 μH*	*1.85*	21.1
Secondary coil self-inductance	L_S	*162 μH*	*6.3*	72.9
Primary resonant capacitor	C_P	*21.7 nF*	*1.82*	21.1
Secondary resonant capacitor	C_S	*21.7 nF*	*6.3*	72.9

Table 3.8. Sizing values of the BWV2H power converters for secondary uncontrolled rectifier together with chopper.

Converter	Element	Value	Voltage [V]	Current [A]
Front-End Converter	Filter inductor L_G	3 mH	808	33.3
	Static switches	-	462.5	33.3
High Frequency Primary Converter	Capacitor C_{DCP}	0.25 mF	462.5	33.3
	Static switches	-	462.5	21.1
High Frequency Secondary Converter	Capacitor C_{DCS}	6.92 μF	143	72.9
	Static switches	-	143	72.9
Bidirectional Chopper	Inductor L_{BC}	151 μH	120	67.5
	Static switches	-	143	67.5

The cost analysis of a WPT installation has been reported in [4] for an EV battery with nominal power of 560 W, i.e. much lower than the one analyzed in this paper. The total cost for the prototype in that case was equal to 5800 €. Differently from the unidirectional WPT of [4], the FEC, HFSC and BC of the BWV2H are bidirectional converters, contributing to further increase the installation costs, nevertheless, it shall be considered that a future mass-production of such a technology could remarkably decrease its cost.

Table 3.9. Sizing values of the BWV2H coupling coils and compensation networks for secondary controlled rectifier.

Element	Symbol	Value	Voltage [kV]	Current [A]
Mutual inductance	*M*	*16.5 μH*	-	-
Primary coil self-inductance	L_P	*162 μH*	*2.25*	25.9
Secondary coil self-inductance	L_S	*162 μH*	*6.3*	72.9
Primary resonant capacitor	C_P	*21.7 nF*	*2.24*	25.9
Secondary resonant capacitor	C_S	*21.7 nF*	*6.3*	72.9

Table 3.10. Sizing values of the BWV2H power converters for secondary controlled rectifier.

Converter	Element	Value	Voltage [V]	Current [A]
Front-End Converter	Filter inductor LG	3 mH	808	41.3
	Static switches	-	462.5	41.3
High Frequency Primary Converter	Capacitor C_{DCP}	0.25 mF	462.5	41.3
	Static switches	-	462.5	21.1
High Frequency Secondary Converter	Capacitor C_{DCS}	3.51 µF	179.5	72.9
	Static switches	-	179.5	72.9
Filter Inductor	Inductor L_O	151 µH	135	42.2

3.6.1 Simulation

This Subsection shows the waveforms obtained through the MATLAB software of some quantities involved in the BWV2H operation such as, the secondary uncontrolled rectifier together with the chopper, and secondary controlled rectifier. At first, the grid-side has been analyzed, achieving the results showed in Fig. 3.12. The grid voltage and the FEC voltage are depicted in solid red and dashed blue line, respectively, while the dashed magenta line reports the voltage across the capacitor C_{DCP} and the solid black line reports the grid current, whose peak value corresponds to $I_{G,N} = 22.6$ A as highlighted in (3.6). Fig. 3.12a and c shows the grid-side of BWV2H during charging mode: it can be observed that the current is lagging the grid voltage: the power factor is in fact set at 0.95, i.e. the minimum allowed by CEI 0-21. The voltage v_{DCP} shows the ripple given by the alternating component of current i_{FEC}, whose frequency is twice the grid frequency and whose amplitude is given by (3.16). Fig. 3.12b and d shows the same quantities depicted in Fig. 3.12a and c, but in discharging mode. Since the grid current is designated as positive when entering into the BWV2H, its phase is shifted by 180°. Furthermore, its amplitude is increased to 33.32 A and 41.3 A, respectively, as described by (3.14).

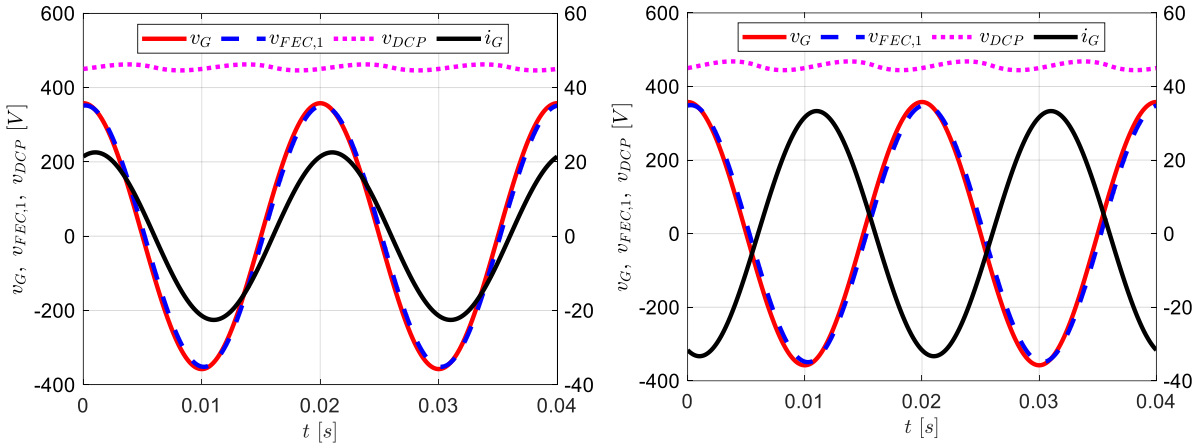

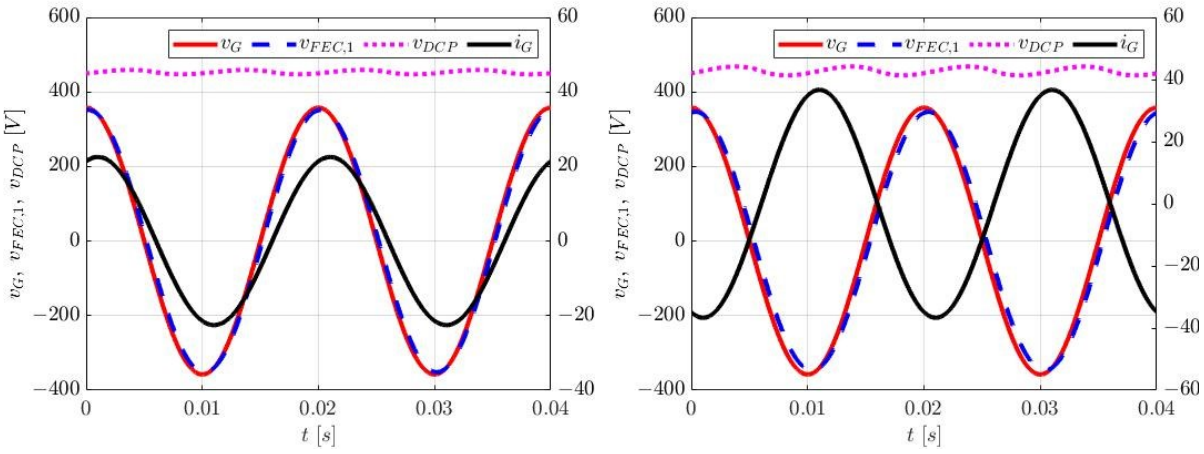

Fig 3.12 Grid-side voltage and current waveform in (a) and (c) charging and (b) and (d) discharging mode, respectively.

Fig. 3.13 presents qualitatively the quantities related to the battery of the BWV2H system such as, the secondary uncontrolled rectifier together with the chopper, and secondary controlled rectifier, i.e. voltage V_B, current I_B and power P_B, in solid red, dashed blue and solid black line, respectively. The time scale indicates 6 hours: during the first 3 hours the battery is charging, whilst during the second 3 hours it operates in discharging mode. Different time intervals during charging and discharging mode are divided as follows:

- *0h-0.3h*: the battery voltage is constant at its minimum value $V_{B,m}$; the current and the power are equal to 0.

- *0.3h-2h*: the current initially is at the nominal value $I_{B,N,c}$ given by (3.12) and the battery voltage increases from $V_{B,m}$ until reaching the maximum value $V_{B,M}$; the current consequently decreases in order to comply with the power limitation.

- *2h-3h*: the voltage is kept at the maximum value $V_{B,M}$ during the constant-voltage charging mode; simultaneously, the current decreases and so does the power.

- *3h-4h*: the battery is in discharging mode. The voltage decreases reaching the nominal value $V_{B,N}$. The battery delivers the nominal current $I_{B,N,d}$. The power is maximum only for the first instants when the battery voltage is equal to $V_{B,M}$, since the current is fixed at $I_{B,N,d}$; then, the power follows the voltage profile.

- *4h-4.3h*: during the last period, the battery voltage is constant at minimum value, whilst the current and the power are equal to 0.

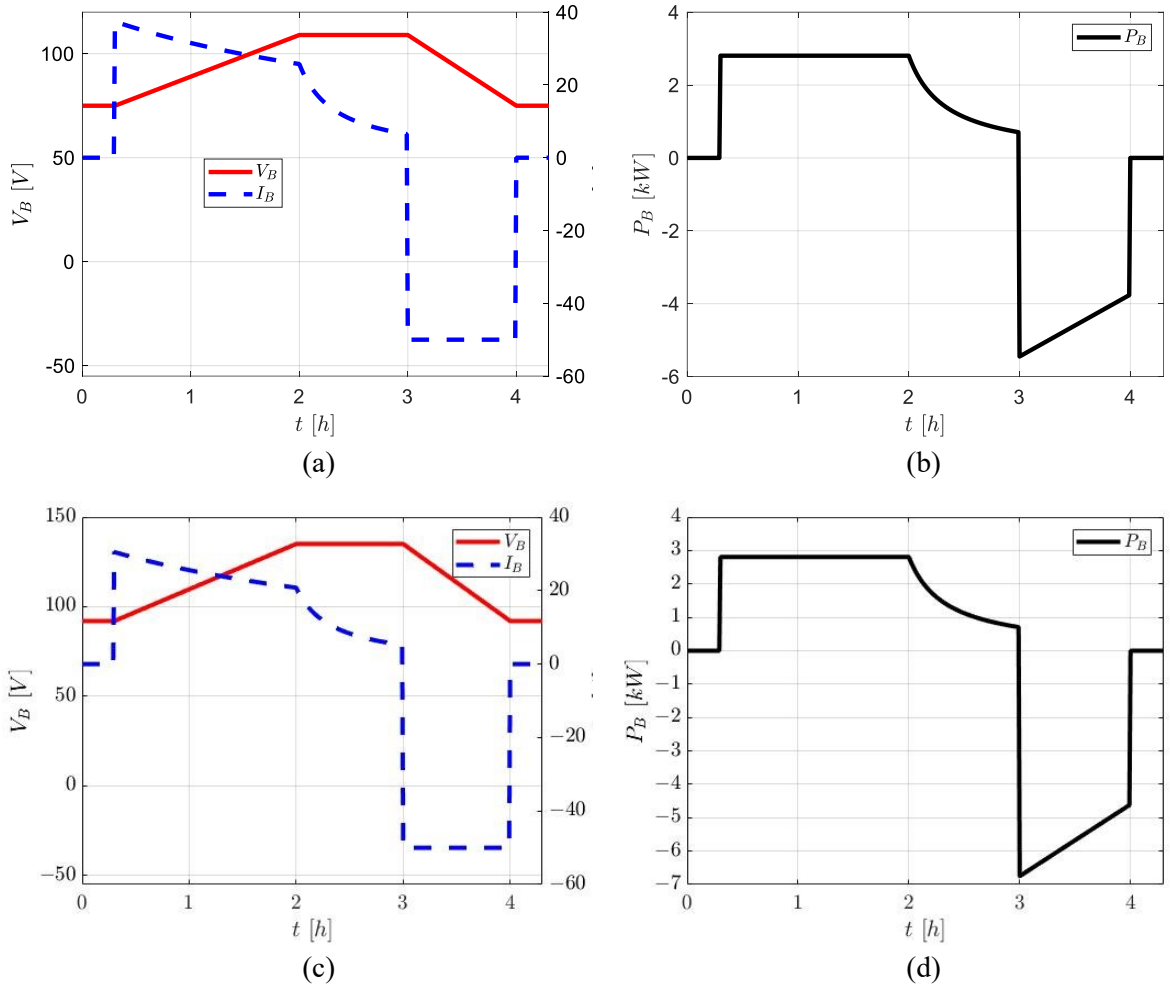

Fig 3.13 Battery-related quantities during charging (from 0 to 3 h) and discharging mode (from 3 to 6 h): (a) and (c) voltage and current and (b) and (d) power.

Usually the first part of battery charging is the constant-current mode, where the voltage increases while the current is kept constant. On the contrary, in this situation when the voltage increases, the current decreases so as to keep the active power constant, as can be observed by inspection of Fig. 3.13a and c. This is due to the power limit set by the maximum contractual power of the user and expressed by (3.11). From 3h to 4h, the battery is in discharging mode, supplying with its power either the domestic loads or the distribution grid. The discharging mode can be inferred from the reverse of the current and power, which are denoted with negative sign in the figure. Since no limitation is established by CEI 0-21 for the injected power, the battery is delivering the nominal current $I_{B,N,d}$ throughout the whole discharging process. As a consequence, when the battery voltage decreases, the power follows the voltage profile. The values reported in Fig. 3.13 reflect the ones found in the design part of Section 3.5.1. In particular, $I_{B,N,c}$ is equal to 37.4 A and 30.48 A respectively, and $I_{B,N,d}$ is equal to 50 A, as specified in Table 3.2 and 3.5. Concerning Fig. 3.13b and d, in the time interval the power absorbed by the battery is 2.8 kW, corresponding to $P_{B,N,c}$, whilst the maximum power is delivered only at the beginning of the discharging process (when $V_B = V_{B,M}$), and it is equal to 5.45 kW and 6.75 kW by using data of Table3.3 and 3.6, shown in Fig 3.13 b and d , respectively.

3.7 Conclusions

This chapter presents a comprehensive step-by-step design procedure for a BWV2H for two different arrangement, giving a handy instrument for its design, which can be easily utilized for higher power WPT systems. Starting from the Italian reference technical rule for the connection of active loads to the LV utility and from the SAE J2954 standard for WPT chargers, the initial constraints are set, regarding the grid-side quantities and the efficiency and operational frequency of the WPT. Subsequently, the grid-side and battery-side specifications have been derived, together with the power limits in each stage of the BWV2H. The maximum allowable currents and voltages are then calculated for each converter, comparing the charging and discharging mode to find out the correct values to be considered for the design. Finally, the reactive elements for the WPT are sized, including the capacitors of the compensation networks, on the basis of the mutual inductance between the two coils required to transfer the active power defined in previous steps. The obtained voltage and current values are plotted though the MATLAB software to illustrate the different modes of operation identified throughout the paper. By suitably changing the constraints introduced in this chapter, such as the input power or the battery parameters, the equations presented can be easily rearranged so as to design a BWV2H according to the user requests. The spread of BWV2H technology will help the demand response and the transition towards the smart grid and a smooth integration of renewable energy sources. A future extension of SAE J2954 in favor of bidirectional WPT will help the development of BWV2H, which require a standardization for their ultimate diffusion.

3.8 Reference

1. Tan, T., Chen, K., Jiang, Y., Lin, Q., Yuan, L., Zhao, Z "A Bidirectional Wireless Power Transfer System Control Strategy Independent of Real-Time Wireless Communication," IEEE Trans. Ind Appl 2020, 56, pp. 1587–1598.

2. Jha, R.K., Buja, G., Bertoluzzo, M., Giacomuzzi, S., Mude, K.N "Performance Comparison of the One-Element Resonant EV Wireless Battery Chargers," IEEE Trans. Ind. Appl. 2018, 54,pp. 2471–2482.

3. Buja, G., Bertoluzzo, M., Mude, K.N. "Design and Experimentation of WPT Charger for Electric City Car," IEEE Trans. Ind. Electron. 2015, 62, pp.7436–7447.

4. Wang, L., Madawala, U.K., Wong, M.-C. A "Wireless Vehicle-to-Grid-to-Home Power Interface with an Adaptive DC," Link. IEEE Trans. Emerg. Sel. Topics Power Electron. 2021, 9, pp.2373–2383.

5. Italian Electrotechnical Committee (CEI). Reference Technical Rules for the Connection of Active and Passive Users to the LV electrical Utilities. CEI 0-21. 2019. Available online: https://www.ceinorme.it/it/norme-cei-0-16-e-0-21.html (accessed on 1 July 2021).

6. J2954: "Wireless Power Transfer for Light-Duty Plug-In/Electric Vehicles and Alignment Methodology," SAE International: Warrendale, PA, USA, 2020.

7. Barnett, S.J. “A Report on Electromagnetic,” Induction. Trans. Am. Inst. Electr. Eng. 1919, 38, pp.1495–1513.

8. Steinmetz, C.P. “Theory of the General Alternating Current Transformer,” Trans. Am. Inst. Electr. Eng. 1895, 12, 245–256.

9. CEBA® EnnoPro Group Limited. Specification for LiFePO4 Rechargeable Cell. Available online: http://en.winston-battery.com/?cnxdc/313.html (accessed on 25 July 2021).

10. Ali, M.U., Zafar, A., Nengroo, S.H. Hussain, S. Junaid Alvi, M.; Kim, H.-J. “Towards a Smarter Battery Management System for Electric Vehicle Applications: A Critical Review of Lithium-Ion Battery State of Charge Estimation. Energies ,”2019, 12, 446.

11. Lipu, M.S.H., Hannan, M.A., Hussain, A., Ayob, A., Saad, M.H.M., Karim, T.F., “How, D.N.T. Data-driven state of charge estimation of lithium-ion batteries: Algorithms, implementation factors, limitations and future trends. J. Clean,” Prod. 2020, 277, 124110.

12. Chen, Z., Yang, L., Zhao, X., Wang, Y., He, Z. “Online state of charge estimation of Li-ion battery based on an improved unscented Kalman filter approach,” Appl. Math. Model. 2019, 70, pp.532–544.

13. Paschero, M., Storti, G.L., Rizzi, A., Mascioli, F.M.F., Rizzoni, G. A “Novel Mechanical Analogy-Based Battery Model for SoC Estimation Using a Multicell EKF,” IEEE Trans. Sustain. Energy 2016, 7, pp.1695–1702.

14. Gholizadeh, M., Salmasi, F.R. “Estimation of state of charge, unknown nonlinearities, and state of health of a lithium-ion battery based on a comprehensive unobservable model,” IEEE Trans. Ind. Electron. 2014, 61, pp.1335–1344.

15. Bonfitto, A., Feraco, S., Tonoli, A., Amati, N., Monti, F. “Estimation Accuracy and Computational Cost Analysis of Artificial Neural Networks for State of Charge Estimation in Lithium Batteries. Batteries” 2019, 5,pp . 47.

16. Salkind, A.J., Fennie, C., Singh, P., Atwater, T., Reisner, D.E “Determination of state-of-charge and state-of-health of batteries by fuzzy logic methodology,” J. Power Sources 1999, 80, pp. 293–300.

17. Electromagnetic Compatibility (EMC) Part 3-2: Limits-Limits for Harmonic Current Emissions (Equipment Input Current ≤ 16 A per Phase); Cei EN IEC 61000-3-2; Italian Electrotechnical Committee (CEI): Milan, Italy, 2019.

Chapter 4

Analysis of losses in two different control approaches for S-S wireless power transfer systems for Electric Vehicle

4.1 Introduction

THIS chapter presents the study and detailed analysis of converter losses at different stages together with the series-series (S-S) compensating coils in wireless power transfer systems, via two distinct approaches to control the power converters. The two approaches towards wireless DC-DC power flow control are termed as the Single-Active High Frequency Wireless Power Transfer (SAHFWPT) system and the Dual Active High Frequency Wireless Power Transfer (DAHFWPT) system. The operation of converters in SAHFWPT and DAHFWPT are controlled by the extended phase shift (EPS) and dual phase shift method respectively. The general schematic of the SAHFWPT system consists of an active bridge and a passive bridge, while the schematic of the DAHFWPT system consists of both active bridges. The efficiency evolutions of ideal SAHFWPT and DAHFWPT are far away from the real ones. Moreover, this chapter analyses the operation and losses of the uni-directional power flow of the WPT system, i.e., from the DC bus in the primary side to the battery load in the secondary side. The loss estimation includes high frequency switching losses, conduction losses, hard turn on and turn off losses coil losses, etc. Also the efficiency of the WPT system depends on operation of the converter. A 50 W–3600 W Power range system at a resonant frequency of 85 kHz is implemented in MATLAB/SIMULATION to demonstrate the validity of the proposed method.

4.2 Background

In the current scenario, the energy storage system (ESS) plays an important role during the different trend of power demand as explained in [1]. As intensity of renewable energy (RE) is not constant throughout a day, the ESS plays a crucial role in the area of storage excess energy that can be generated by the RE sources [2], and that can be used to power the various loads such as a household load, industrial load, street load, etc. when we are not able to use the RE sources. The wireless DC–DC converters are becoming more pervasive due to the fact that they are compact in size, isolated power flow between the resonating coils, and have excellent efficiency [3]. In earlier studies, there have been a lot of isolated DC–DC power converters, such as single active bridge (SAB), dual active bridge (DAB), phase shift full bridge (PSFB), and so on for high-frequency applications mentioned in [4,5,6,7,8].

Fig. 4.1 shows the generalized schematic of the wireless DC–DC converter that can be used for both Single Active High-Frequency Wireless Power Transfer (SAHFWPT) and Dual Active High-Frequency Wireless Power Transfer (DAHFWPT). During the operation of the SAHFWPT system, the primary side converter operates as an active converter, i.e., high-frequency inverter, and the secondary side converter operates as a passive converter through the diode, i.e., uncontrolled rectifier. The control approach of the primary H-bridge converter takes place by the internal phase shift control method as describe in [9,10,11]. In the operation of DAHFWPT system, the primary and secondary sides H-bridge converters are operating as active bridges, but their operation is different, i.e., the primary works as the high-frequency inverter and the secondary works as the controlled rectifier [12]. Moreover, the control of the primary and secondary H-bridge converters was also takes place by the internal phase shift

control method. However, in both the SAHFWPT and DAHFWPT converters, power transfer takes place via external phase shift of converter from the source voltage V_S to the load which can be considered equivalent load resistance R_B in place of the battery. As the H-bridge works at high frequency, the passive components (i.e., S-S coupling coil, source filters, and load filters) compatibly reduce in size so that the SAHFWPT and DAHFWPT system stand out due to the high values for the power density as well as specific power in [13,14,15,16].

As previously stated, the SAHFWPT and the DAHFWPT converters can be used in applications requiring both uni-directional and Bi-directional power flow, such as electric vehicles, household appliances, mobile phones, medical devices, and other fields [17]. The schematics for SAHFWPT and DAHFWPT in Fig. 4.1 include two H-Bridge, besides the two H-bridges, with following elements: (1) the coupling coils L_P and L_S as well as the series resonating capacitors C_P and C_S, which keep coil current sinusoidal even when the voltage across the series compensated coil in a quasi-square or square wave; the mutual inductance M between the primary and secondary coils; (2) the capacitor C_O, which filters out ripple of the voltage V_O; (3) the inductor L_O, which can filter out the ripple of current that passes through R_B; (4) and the resistance R_B represents the battery's equivalent resistance [18,19,20,21,23,24].

The most effective optimization models are those that are based on the nonlinear equivalent model of the magnetic equivalent coupler of the WPT converters. This model considers the losses that are incurred as a result of the nonlinear operation of the converters, which include the conduction losses in MOSFETs, diodes, and body diodes, the hard-switching loss of the switches, and the reverse recovery loss of diodes. The gap between standard loss models and experimental measurements is well-known in [6]. Table 4.1 provides a comparison overview between a SAHFWPT and a DAHFWPT in terms of control method, losses, and selection of extra DC–DC converter. It is ideal to build a DAHFWPT battery charger with no additional DC–DC converter. Soft switching of the inverter and active rectifier circuits takes place with the help of zero voltage switching (ZVS) and zero current switching (ZCS), resulting in low circulating reactive power when the external phase shift of the converters is equal to 3π/2, and optimized overall loss is described in [14]. Depending on their application, four distinct switching modes (single phase shift (SPS) [25], extended phase shift (EPS), dual phase shift (DPS) [26], and triple phase shift (TPS) [6] may be used to optimize converters losses. Whereas, SAHFWPT is ideal to build a battery charger with an additional DC–DC converter, while SAHFWPT has no circulating current as the external phase shift angle is fixed at 3π/2, soft switching of the inverter and passive rectifier by the help of zero voltage switching (ZVS) and zero current switching (ZCS) are mention in [27], and overall loss optimization. Depending on their use, two distinct switching options are available, such as SPS and EPS. The S-S coil losses are included in both systems, but these losses are not same as they are dependent on the current and design parameters of the coil.

Many of the articles discuss the switching operation, power flow operation, and different approaches to control of the SAHFWPT and DAHFWPT converters for EV. The comparative study of power loss of converters and coils during operation of the SAHFWPT and DAHFWPT converters is discussed in this chapter. Apart from that, the purpose of this chapter is to study

the effects on the overall efficiency of the WPT of the two different control methods, i.e., EPS and DPS of the H-bridge converter for SAHFWPT and DAHFWPT, respectively. Further, we performed a comparative analysis of the power range of WPT, while keeping the battery voltage constant. For this study, we fixed the internal phase angle of the primary and secondary H-bridge, the angles to be equal in the operation of DAHFWPT, and we are aware that the secondary of SAHFWPT works as the uncontrolled rectifier. So, to maintain the same power drawn from the source as DAHFWPT, we must only change the internal phase shift angle of the primary H-bridge.

Table 4.1 A comparison is made between a SAHFWPT and a DAHFWPT.

Feature		**SAHFWPT**			**DAHFWPT**		
Reference		[3]	[5]	[6–9]	[3]	[5]	[6–9]
Switching control	SPS	✗	✓	✓	✗	✓	✓
	EPS	✓	✓	✓	✗	✓	✓
	DPS	✗	✗	✗	✓	✓	✓
	TPS	✗	✗	✗	✗	✓	✓
Additional chopper		✓	✓	✓	✗	✗	✗
Hard switching of MOSFET		✗	✗	✓	✗	✗	✓
Circulating current		✗	✗	✗	✗	✓	✓
S-S coil loss		✓	✓	✓	✓	✓	✓
Overall loss analysis		✗	✗	✓	✗	✗	✓

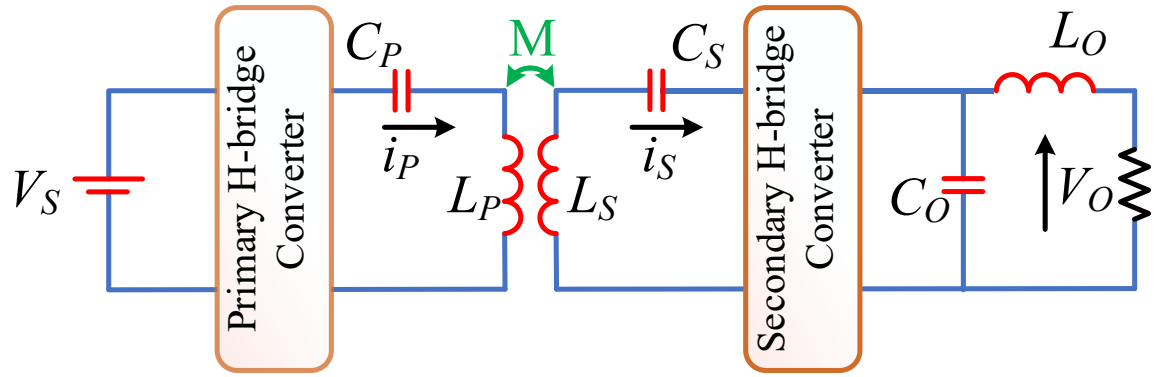

Fig 4.1 Schematic of wireless DC–DC converter.

4.3. Methods of Operation of SAHFWPT and DAHFWPT

4.3.1. Circuit Schematic

The schematics of the SAHFWPT and DAHFWPT converters are shown in Fig. 4.2. a,b. The SAHFWPT and DAHFWPT are separated into primary and secondary sections. The primary active H-bridge is designed as the high-frequency primary converter (HFPC), which is powered by the DC source voltages V_{DCP_S} and V_{DCP_D} for both the SAHFWPT and the DAHFWPT, respectively. HFPC work as a high-frequency phase shift inverter, generating high-frequency quasi-square wave output voltages v_{HFPC_S} andv_{HFPC_D}. The output current i_{P_S} and i_{P_D} are sinusoidal due to the resonating effect of the coil. Moreover, output voltage waveform level depends on switching control method, as mentioned in Table 4.1. The output voltage levels of HFPC by SPS and EPS switching are two and three, whereas in the control

operation the HFSC have an output voltage level of two in SAHFWPT and DAHFWPT. Aside from these two switching methods, the DPS and TPS are only useful for DAHFWPT. Since the SAHFWPT secondary is uncontrolled and the resulting voltage is always two levels. The HFPC consists of four MOSFETs ($T_5 - T_8$). Furthermore, if we look at the HFPC schematic in Fig. 4.2.a,b, we can observe the antiparallel body diodes ($D_5 - D_8$) of MOSFETs, that can be operated when the circulating current flow takes place. The coupled coils create the connection between the primary and secondary converter by wireless means. The secondary H-bridges is referred as the high-frequency secondary rectifier (HFSR) or high-frequency secondary converter (HFSC) according to their passive or active operations, respectively. The voltage v_{HFSR_S} and v_{HFSC_D} induced in the secondary coil due to variation in current i_{P_S} and i_{P_D} in the primary coil, according to the Faraday law of induction, secondary voltage serves as the input voltage source of the HFSR and HFSC and the current i_{S_S} and i_{S_D} flow through the secondary coil. The output voltage V_{O_S} and $V_{O_D}$of the HFSR and HFSC are applied across the equivalent load, which includes the low pass filter $L_O C_O$ and R_B equivalent battery resistance, where C_O can be used to smooth or remove the ripple of voltage V_{O_S} and V_{O_D}, and L_O can be used to smooth or remove ripple of current I_{O_S} and I_{O_D}. The output voltages V_{O_S} and V_{O_D}, as well as the currents I_{O_S} and I_{O_D}, are kept at the desire levels for charging the battery by the phase-shifted regulation of the HFPC and HFSC. The HFSR and HFSC are fabricated of four high-frequency diodes ($D_9 - D_{12}$) and MOSFETs ($T_9 - T_{12}$) with the relevant antiparallel body diodes ($D_9 - D_{12}$), respectively. The primary side's input filter is a C_I filter, which is not seen in Fig. 4.2. a,b.

The switching frequency of the SAHFWPT and DAHFWPT converters are in the range of 79–90 kHz. The operating frequency was fixed at 85 kHz and the resonant circuits are tuned to this frequency as in [9,10]. This frequency is selected as per the J2954 standard of the society of automotive engineering (SAE) about charging of electric vehicle through WPT. The design of self-inductor L_P, L_S and capacitors C_P, C_S of the series-series resonating coil are usually at resonating frequency ω_r i.e,

$$\omega_r = \frac{1}{\sqrt{L_P C_P}} = \frac{1}{\sqrt{L_S C_S}} \tag{4.1}$$

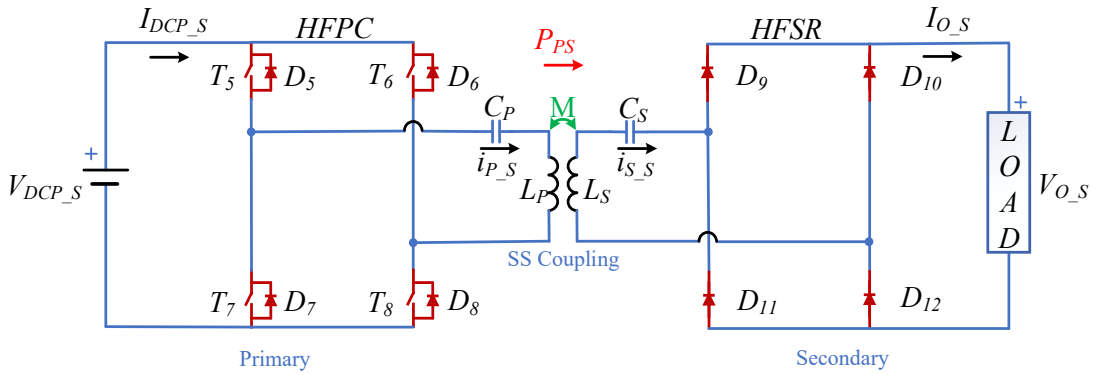

(a)

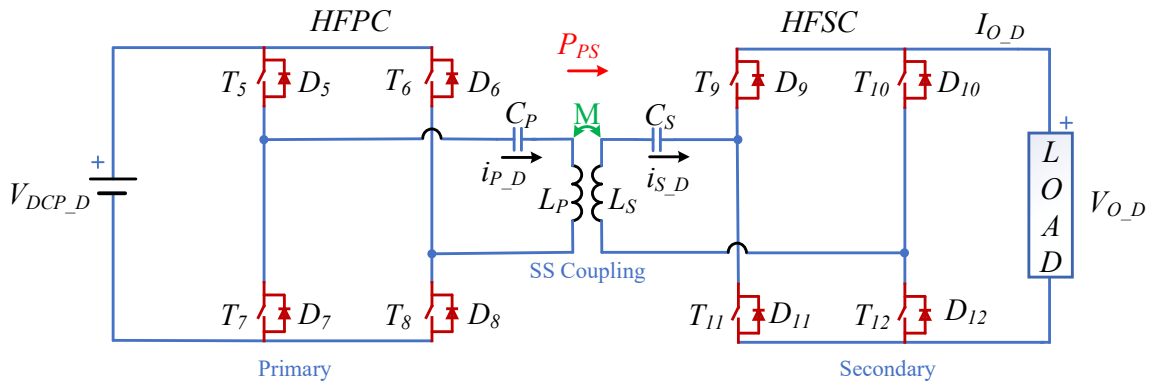

(b)

Fig 4.2 Schematic of WPT converter with equivalent load (a) SAHFWPT (b) DAHFWPT

4.3.2. Operation and Analysis

Fig. 4.2.a,b depict the switching operation of the SAHFWPT and DAHFWPT converters at resonance frequency. The EPS and DPS switching mechanisms are used to control the converters of SAHFWPT and DAHFWPT, respectively. The plot is divided in three parts: (1) gate signals of the HFPC on the upper section of the plot, (2) waveforms of current and voltage of HFPC together with the conduction intervals of its switches, (3) and waveforms of current and voltage for HFSR together with the conduction intervals of its switches in the case of SAHFWPT (Fig. 4.3. a) and gate signals. For correlation between both the wave forms, the gate signals in the upper section are assumed same for both SAHFWPT and DAHFWPT, the HFPC switching operation takes place by the internal phase shift angle between its two legs. The middle part of Fig. 4.3. a,b, depicts the direction of current flow through the HFPC's. During the positive half cycle of the current, three different switching periods can be recognized, namely (1) interval 1: (0 to $\Phi - \alpha/2$), (2) interval 2: ($\Phi - \alpha/2$ to $\Phi + \alpha/2$), and (3) interval 3: ($\Phi+\alpha/2$ to π). While the currents i_{P_S} and i_{P_D} circulate in the MOSFETs and body diode, the circulating current does not flow across the source voltage V_{DCP_S} and V_{DCP_D}, respectively. Indeed, the output voltage of HFPC is zero, i.e., $v_{HFPC\_S} = v_{HFPC\_D} = 0$, in the intervals 1 and 3. Switches (T8, D7), and (T5, D6) are in conduction state, as the energy stored in the reactive element such as L_P and C_P forces the current to circulate in intervals 1 and 3. Aside from that, the amplitudes of v_{HFPC_S} and v_{HFPC_D} in interval 2 are identical to V_{DCP_S} and V_{DCP_D}. The wave forms clearly show that the output voltages v_{HFPC_S} and v_{HFPC_D} square, as well as the currents current i_{P_S} and i_{P_D} sinosuidal, are in the same phase and have half-wave symmetry, due to the resonating behavior of the coil. As per the Faraday law induction, EMF is induced in the secondary coil due to flux linkage between the primary and secondary. The average power P_{PS} flow from primary to secondary due to induced voltage in the secondary, which can serve as voltage source for the SAHFWPT and DAHFWPT secondary.

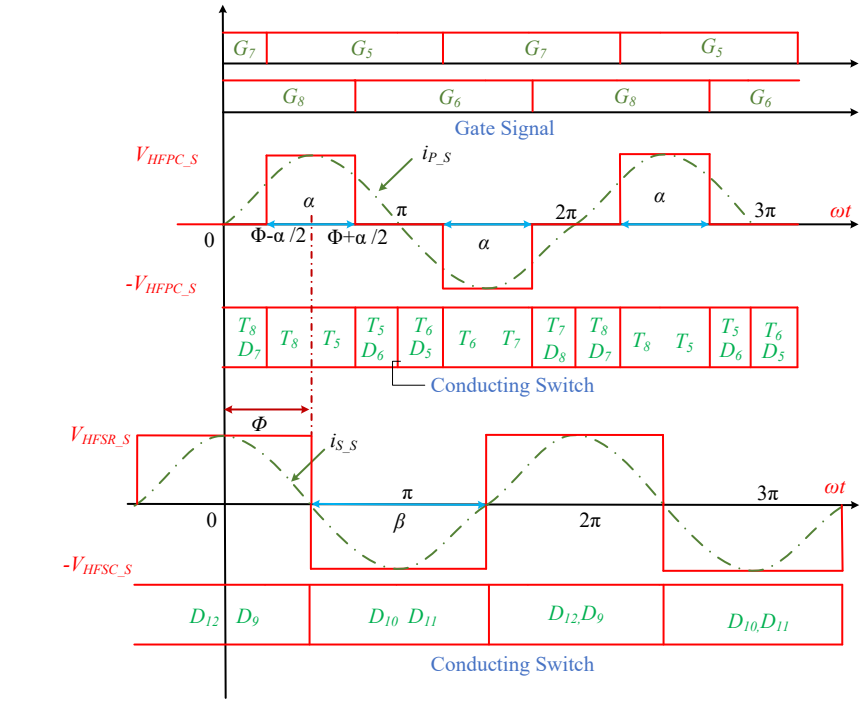

(a)

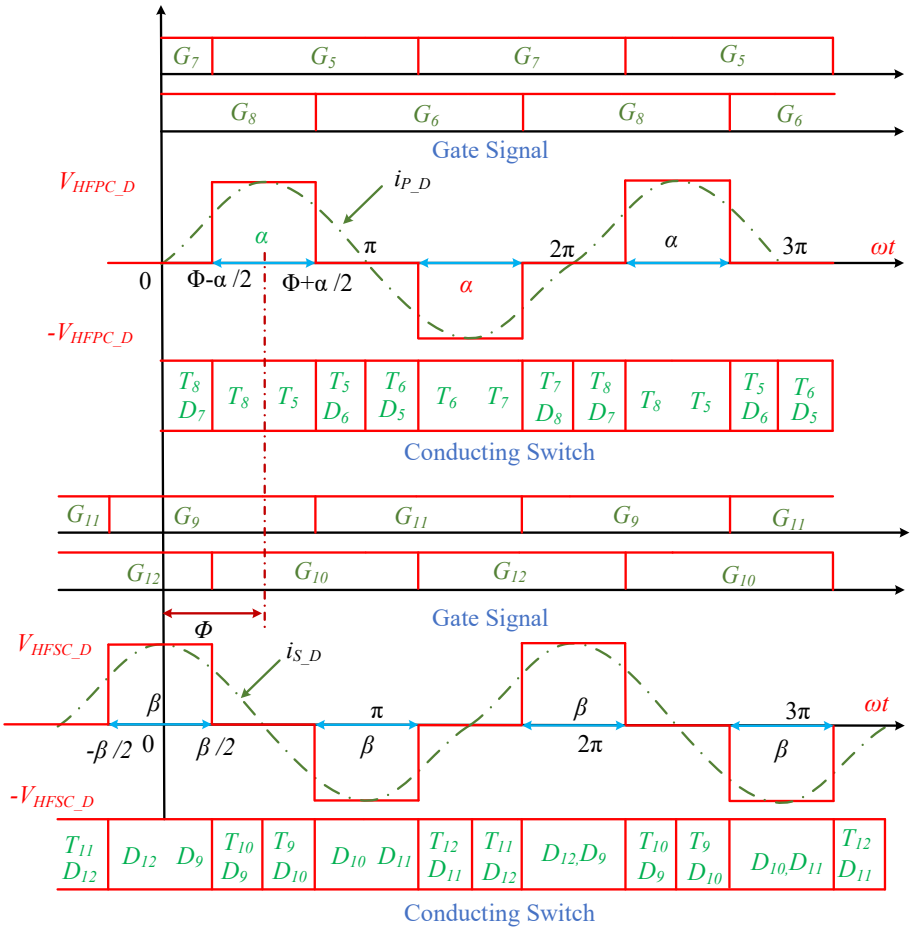

(b)

Fig. 4.3 Control signal and operating waveform of WPT (a) SAHFWPT (b) DAHFWPT.

HFSR and HFSC converters are passive and active in behaviour, respectively. As shown in the lower part of the waveform in Fig. 4.3. a, HFSR conducts for a full cycle, i.e., (D_{12}, D_9) conducts during the positive half cycle and (D_{10}, D_{11}) conducts during the negative half cycle. As a matter of fact, the HFSR input voltage v_{HFSR_S} and current i_{S_S} are square and sin wave, respectively, thanks to the resonating behaviours of the coil. On the contrary, the active rectifier HFSC operation during the positive half cycle is divided into three intervals: (1) interval 1: $-\pi/2$ to $-\beta/2$; (2) interval 2: $-\beta/2$ to $\beta/2$; and (3) interval 3: $\beta/2$ to $\pi/2$. In the intervals 1 and 3, the output voltage of HFSC is zero, i.e., $v_{HFSC\_D} = 0$, while the current i_{S_D} flows in the MOSFETs and body diodes of HFSC and do not reach the load. The switches (T_{11}, D_{12}) and (T_{10}, D_9) are in conduction state during the intervals 1 and 3 respectively. The circulation of current occurs due to the energy stored in the reactive elements such as C_S and L_S. Apart from this, the amplitudes of v_{HFSR_S} and v_{HFSC_D} are equal to V_{O_S} and V_{O_D} in the interval 2. From the shape of the wave form, it was easy to see that the output voltages v_{HFSR_S} and v_{HFSC_D} square and the currents i_{S_S} and i_{S_D} sinusoidal have the same phase and are half-wave symmetric, due to the resonating behaviours of the coil.

The output voltagesV_{O_S} , V_{O_D} and currents i_{S_S}, i_{S_D} of the HFSR, and HFSC are almost constant due to filtering effect of L_O and C_O. The external phase shift angle for primary and secondary converter is fixed at Φ in the case of SAHFWPT and DAHFWPT.

The equivalent circuit of SAHFWPT and DAHFWPT with S-S coupling is shown in Fig. 4.4. As per Fig.4.3 the operation begins at time t = 0, and the internal phase shift angles of HFPC and HFSC are α and β, respectively (whereas in the case of SAHFWPT, $\beta = \pi$ is fixed). The external phase shift angle Φ varying in the range [0 2π] during the operation of DAHFWPT (whereas $\Phi = 3\pi/2$ is fixed in the case of SAHFWPT). The voltages v_{HFPC} and v_{HFSC} are expressed as a Fourier series as follows:

$$v_{HFPC}(t) = v_{HFPC\_M} \sum_{n=1,3,\ldots}^{\infty} \frac{1}{n} sin(\omega_r t)\, sin\left(\frac{n\alpha}{2}\right) \qquad (4.2)$$

$$v_{HFSC}(t) = v_{HFSC\_M} \sum_{n=1,3,\ldots}^{\infty} \frac{1}{n} sin(\omega_r t + \Phi)\, sin\left(\frac{n\beta}{2}\right) \qquad (4.3)$$

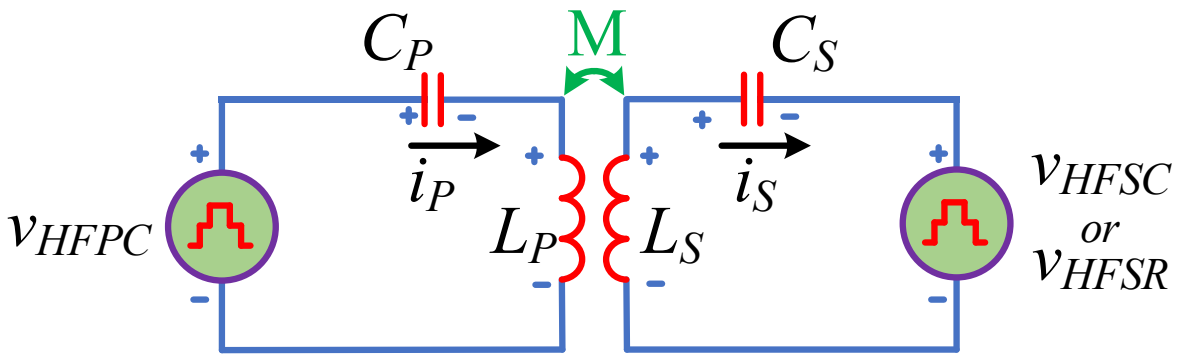

Fig. 4.4 Equivalent circuit of the SAHFWPT and DAHFWPT with S-S coupling.

The maximum values of amplitudes for the first harmonic components of the voltages of the HFPC and HFSC of DAHFWPT are represented by v_{HFPC_M} and v_{HFSC_M}, respectively. Take into consideration that the external phase shift angle Φ ranges in the interval [0, 2π] for the Bi-directional operation DAHFWPT, whilst for the uni-directional operation, such as power flow exclusively from primary to secondary, the external phase shift angle Φ spans the interval [π, 2π]. However, for maximum power transfer it is Φ = 3π/2. Apart from Φ = 3π/2 value, the power transfer is not maximal due to the reactive current being not in the phase with the HFPC output and HFSC input voltage. This leads the circulating current flowing through the converter and coil.

Since the HFSR is a passive converter, the following conditions hold β = π and Φ = 3π/2, and from (4.3) the input voltage for the HFSR is expressed as:

$$v_{HFSR}(t) = v_{HFSR\_M} \sum_{n=1,3,\dots}^{\infty} \frac{1}{n} sin(\omega_r t + \Phi) \tag{4.4}$$

The harmonic and maximum harmonic input voltage of HFSR of SAHFWPT are represented by v_{HFSR} and v_{HFSR_M}. From Equation (4.2) it is clear that primary voltage v_{HFPC} relation is same for SAHFWPT and DAHFWPT. So from Fig. 4.3 and 4.4 $v_{HFPC\_S} = v_{HFPC\_D} = v_{HFPC}$. Indeed the secondary voltage relation is not same, from the Fig. 4.3 and Fig. 4.4, $v_{HFSR\_S} = v_{HFSR}$ and $v_{HFSC\_D} = v_{HFSC}$, respectively.

Applying Kirchhoff's voltage law in Fig. 4.4, we obtain

$$v_{HFPC}(t) = R_P i_P(t) + L_P \frac{di_P(t)}{dt} + v_{P_C}(t) + v_P(t) \tag{4.5}$$

$$v_{HFSC}(t) = -R_S i_S(t) + +L_S \frac{di_s(t)}{dt} + v_{s_C}(t) + v_S(t) \tag{4.6}$$

where R_P and R_S internal resistance, L_P and L_s self-impedance of coil, $v_{P_C}(t)$ and $v_{S_C}(t)$ voltage drop across capacitor, $i_P(t)$ and $i_S(t)$ current flow from the S-S coil, $v_P(t) = \mathrm{M}\frac{di_S(t)}{dt}$ and $v_S(t) = -\mathrm{M}\frac{di_P(t)}{dt}$ are the induced voltage of primary and secondary S-S coils, respectively, M is the mutual inductance.

At the resonance frequency, the instantaneous power absorbed by the inductor L_P, L_S is equal to the instantaneous power delivered by the capacitorC_P, C_S. The net power delivered and absorbed by the capacitor and inductor is zero in the primary and secondary S-S coils, respectively. The impedance of the S-S coils is minimum at the resonating condition. Indeed, primary and secondary coil impedances are minimum; therefore, they represent the internal resistance of the S-S coil, i.e., R_P, R_S. Therefore, Equations (4.5) and (4.6) are re-arranged at resonating frequency as

$$i_P(t) = \frac{v_{HFPC}(t) - v_P(t)}{R_P}$$

$$i_S(t) = \frac{-v_{HFSC}(t) + v_S(t)}{R_S} \quad (4.7)$$

The voltage and current relationship at fundamental resonance frequency are represented in (4.8) to (4.11) for the DAHFWPT, similarly it is represented in (4.12) to (4.15) for SAHFWPT, by using approximation ωM >> R_S and $(\omega M)^2 >> R_P R_S$ for high Q-factor coil [6]. The expressions DAHFWPT and SAHFWPT are represented at fundamental harmonic approximation of the sinusoidal component in Tables 4.2 and 4.3 [20,22], respectively.

Table 4.2. DAHFWPT current voltage expressions at fundamental harmonic.

$v_{HFPC\_1}(t) = v_{HFPC\_1\_M} \sin\left(\frac{\alpha}{2}\right) \sin(\omega_r t)$	(4.8)	$v_{HFSC\_1}(t) = v_{HFSC\_1\_M} \sin\left(\frac{\beta}{2}\right) \sin(\omega_r t + \Phi)$	(4.9)
$i_{P\_D\_1}(t) = \frac{v_{HFSC\_1\_M}}{M\omega_r} \sin\left(\frac{\beta}{2}\right) cos(\omega_r t + \Phi)$	(4.10)	$i_{s\_1}(t) = \frac{-v_{HFPC\_1\_M}}{M\omega_r} \sin\left(\frac{\alpha}{2}\right) cos(\omega_r t)$	(4.11)

Table 4.3. SAHFWPT current voltage expressions at fundamental harmonic.

$v_{HFPC\_1}(t) = v_{HFPC\_1\_M} \sin\left(\frac{\alpha}{2}\right) \sin(\omega_r t)$	(4.12)	$v_{HFSR\_1}(t) = v_{HFSR\_1\_M} \sin(\omega_r t + \Phi)$	(4.13)
$i_{P\_S\_1}(t) = \frac{v_{HFSR\_1\_M}}{M\omega_r} cos(\omega_r t + \Phi)$	(4.14)	$i_{s\_1}(t) = \frac{-v_{HFPC\_1\_M}}{M\omega_r} \sin\left(\frac{\alpha}{2}\right) cos(\omega_r t)$	(4.15)

$v_{HFPC\_1\_M}$, $v_{HFSC\_1\_M}$ and v_{HFPC_1}, v_{HFSC_1} are the fundamental maximum amplitude and fundamental voltage of HFPC and HFSC, respectively. The secondary fundamental currents i_{s_1}, represented in Equations (4.11) and (4.15) for DAHFWPT and SAHFWPT, are the same as they only depend on α. Moreover, the primary fundamental current $i_{P\_D\_1}$ of DAHFWPT depends on β, while the primary fundamental current $i_{P\_S\_1}$ of SAHFWPT is constant, as β is fixed at π.

The uni-directional power flow was considered only in the case of battery charging, and the rated source voltages $V_{DCP\_S} = V_{DCP\_D}$ = 386 V are constant for SAHFWPT and DAHFWPT; as mentioned in Table 4.4 the battery voltage is also same, i.e., $V_{O\_S} = V_{O\_D}$ = 120V. The secondary absolute lossless power for SAHFWPT and DAHFWPT can be express in (4.16) and (4.17) by using the (4.9), (4.11), (4.13), and (4.15)

$$P_{SAHFWPT\_S} = \frac{-v_{HFPC\_1\_M} v_{HFSC\_1\_M} \sin\left(\frac{\alpha}{2}\right) \sin(\Phi)}{2\omega M} \quad (4.16)$$

$$P_{DAHFWPT\_S} = \frac{-v_{HFPC\_1\_M} v_{HFSC\_1\_M} \sin\left(\frac{\alpha}{2}\right) \sin\left(\frac{\beta}{2}\right) \sin(\Phi)}{2\omega M} \quad (4.17)$$

where $v_{HFPC\_1\_M} = \frac{4V_{DCP\_S}}{\pi}$ and $v_{HFSR\_1\_M} = \frac{4V_O}{\pi}$ are the maximum voltage at the primary and secondary coil. From the Equations (4.16) and (4.17), the secondary power can be regulated using the internal phase shift angles $\alpha = \beta \in [0, 2\pi]$, and external phase shift angle $\Phi \in [\pi, 2\pi]$, while in Equation (4.16) $\beta = \pi$ and $\Phi = 3\pi/2$. the secondary power of SAHFWPT and DAHFWPT can be related by Equation (4.18):

$$P_{DAHFWPT\_S} = sin\left(\frac{\beta}{2}\right) P_{SAHFWPT\_S} \tag{4.18}$$

Table 4.4. Simulation parameter for EV.

Parameters	Symbols	Values
Source Rated Voltage	V_{DCP_S}, V_{DCP_D}	384 V
Battery Rated voltage	V_{O_S} ,V_{O_D}	120 V
Resonating frequency	f_r	85 kHz
MOSFETs	$T_5 - T_{12}$	SiHG33N60EF
Self-Inductance	$L_P L_S$	220 µH
Compensation Capacitors	$C_P C_S$	15.9 nF
S-S coil Resistance	$R_P R_S$	0.5 Ω
Mutual-Inductance	M	22.5 µH

Fig. 4.5 shows the comparison of power curve between DAHFWPT and SAHFWPT of secondary power, w.r.t α, where α is in radian. The power $P_{DAHFWPT\_S}$ plotted with the red line, and $P_{SAHFWPT\_S}$ plotted with the blue line are directly related with sin(α/2) as mentioned in (4.18), when we fixed $\Phi = 3\pi/2$ for maximum power transfer condition. From the power curve, it can be proven that the power of DAHFWPT and SAHFWPT are same at α = 3.14, i.e., π. Apart from that, DAHFWPT power sinusoidal decreases and it is always less than the SAHFWPT power that decreases almost linearly. It is observed in Fig. 4.5 that SAHFWPT and DAHFWPT have similar instantaneous power, the internal phase shift angle of secondary power of DAHFWPT is always bigger than secondary power of SAHFWPT.

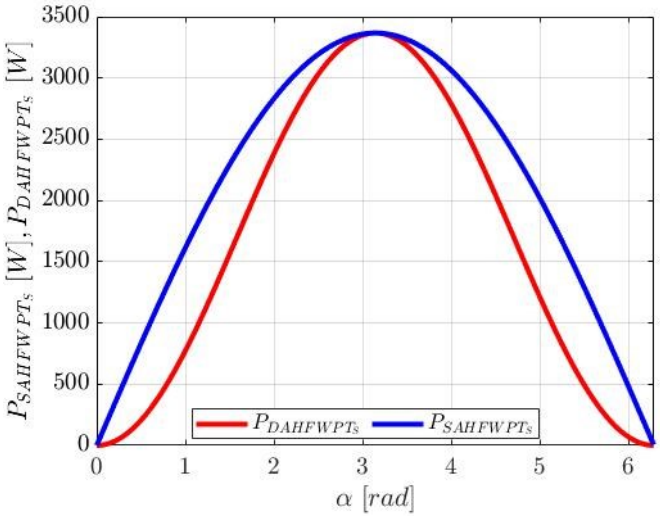

Fig. 4.5 Secondary of the S-S coupling coil power relation of SAHFWPT and DAHFWPT w.r.t. α.

4.4. Methods of Loss Analysis of SAHFWPT and DAHFWPT

The operation of SAHFWPT and DAHFWPT are approximately same. The only difference is in the operation of the secondary side converter. The secondary HFSR of SAHFWPT is the passive converter, while the secondary HFSC of DAHFWPT is the active converter. Because HFSR and HFSC work in different ways, they are operating in the soft switching mode and the hard switching mode, respectively. Indeed, the switching losses of switches for the HFSR and HFSC are lower and higher, respectively. However, each diode of the HFSR are conducted for a π phase interval, whereas the conducting phase interval of the HFSC switches depending on β which one varies in the range of [0, 2π] so that the conduction period of HFSC switches may be π or the lesser than π period. The conduction loss of MOSFETs and body diodes depends on the amount of current flowing in the converter. As the secondary converter operation of the SAHFWPT and DAHFWPT are not the same, the power drawn from the source towards the rated load is different. Furthermore, conduction losses are only equal at the α = β = π. Apart from this loss, the few losses that depend on the converters are due to the gate charge, body diode conduction, output capacitor, body diode recovery, hard turn on, and hard turn off. In this section the comparative loss in the S-S coil is elaborated by using simulation parameter that listed in Table 4.4 whilst the losses in the filter capacitor and inductor are neglected.

4.4.1. S-S Coil Loss

Referring to the equivalent circuit shown in Fig. 4.4, the resistive loss of the S-S coupling coil [10] can be expressed as:

$$P_{S-S\_coil\_SAHFWPT\_loss} = i^2_{P\_S\_1\_rms}R_P + i^2_{S\_1\_rms}R_S \tag{4.19}$$

$$P_{S-S\_coil\_DAHFWPT\_loss} = i^2_{P\_D\_1\_rms}R_P + i^2_{S\_1\_rms}R_S \tag{4.20}$$

where $i_{P\_S\_1\_rms}$, $i_{P\_D\_1\_rms}$, and $i_{S\_1\_rms}$ are the rms values of $i_{P\_S\_1}$, $i_{P\_D\_1}$, and i_{S_1}, respectively. R_P and R_S are the primary and secondary coil resistance. Using (4.10), (4.14) and any one from (4.11) and (4.15), we obtain

$$i_{P\_S\_1\_rms} = \frac{v_{HFSR\_1\_M}}{\sqrt{2}M\omega_r} \tag{4.21}$$

$$i_{P\_D\_1\_rms} = \frac{v_{HFSC\_1\_M}}{\sqrt{2}M\omega_r} sin\left(\frac{\beta}{2}\right) \tag{4.22}$$

$$i_{S\_1\_rms} = \frac{v_{HFPC\_1\_M}}{\sqrt{2}M\omega_r} sin\left(\frac{\alpha}{2}\right) \tag{4.23}$$

The efficiency of the S-S coupling coil of SAHFWPT and DAHFWPT can be expressed by using (4.16), (4.17), (4.19), and (4.20) as

$$\eta_{S-S\_coil\_SAHFWPT} = \frac{P_{SAHFWPT\_S}}{P_{SAHFWPT\_S} + P_{S-S\_coil\_SAHFWPT\_loss}} \quad (4.24)$$

$$\eta_{S-S\_coil\_DAHFWPT} = \frac{P_{DAHFWPT\_S}}{P_{DAHFWPT\_S} + P_{S-S\_coil\_DAHFWPT\_loss}} \quad (4.25)$$

$$\eta_{S-S\_coil\_SAHFWPT} = \frac{\eta_{S-S\_coil\_DAHFWPT}(A + B + C)\sin\frac{\alpha}{2}}{A\sin\frac{\alpha}{2} + B + C\sin^2\frac{\alpha}{2}} \quad (4.26)$$

Equation (4.26) represents the relation between $\eta_{S-S\_coil\_SAHFWPT}$ and $\eta_{S-S\_coil\_DAHFWPT}$ and can be derive by using (4.16), (4.17), (4.19), (4.20), (4.24), and (4.25) and setting

$$A = \frac{v_{HFPC\_1\_M} v_{HFSR\_1\_M}}{2M\omega_r}$$

$$B = \frac{\mathrm{R}v^2{}_{HFSR\_1\_M}}{2M^2\omega^2{}_r}$$

$$C = \frac{\mathrm{R}v^2{}_{HFPC\_1\_M}}{2M^2\omega^2{}_r} \quad (4.27)$$

$$R = R_R = R_S$$

$$\alpha = \beta$$

Fig. 4.6 shows the comparison of the S-S coil efficiency curves of SAHFWPT and DAHFWPT w.r.t α. They are computed by (4.24) and (4.25), using the parameters listed in Table 4.4 taken from an experimental setup. The efficiency plot of $\eta_{S-S\_coil\_SAHFWPT}$ is drawn in a solid blue line, while the plot of $\eta_{S-S\_coil\_DAHFWPT}$ is drawn in solid red line. At α = π the efficiency is equal in both systems. The efficiency of both systems are approximately same in the range of 2 rads to 4 rads. Further with movement left from 2 rads and right from 4 rads and up to approximate 0.3 rads and 6 rads, the efficiency of the SAHFWPT is higher than the DAHFWPT. Equation (4.26) complies with the graph plotted in Fig. 4.6.

4.4.2. Loss of HFSR, HFSC and HFPC

According to the Fig. 4.2a,b, the secondary and primary converters of SAHFWPT and DAHFWPT are denoted as HFSR, HFSC, and HFPC. Two MOSFETs SiHG33N60EF are turned on at a same instant of time in the HFSC and HFPC converter during the active mode. Furthermore, the diodes are used for the passive mode of the HFSR. As the converters have a different operating principle, their losses are not equal.

4.4.2.1 Conduction Loss of MOSFET and Diodes

The conduction loss depends on amount of current flowing through the converter switches during in operating state, i.e., $i_{s\_1\_\mathrm{rms}}$, $i_{P\_s\_1\_\mathrm{rms}}$, and $i_{P\_D\_1\_\mathrm{rms}}$. The current $i_{s\_1\_\mathrm{rms}}$ depends on α, but α is not the same in both the HFSR and HFSC converters for the same instantaneous

power. As shown in Fig. 4.5, the current flowing through HFSR is less than the current following through the HFSC apart from α =π. The current $i_{P\_S\_1\_\mathrm{rms}}$ is constant at 8.99 A whilst $i_{P\_D\_1\_\mathrm{rms}}$ varies depending on β, and is always lower than or equal to 8.99 A. The conduction losses of the diodes, body diodes, and MOSFETs are $P_{HFSR\_Cond\_loss}$, $P_{HFSC\_Cond\_loss}$, $P_{HFPC\_Cond\_S\_loss}$, and $P_{HFPC\_Cond\_D\_loss}$ and are represented in Equations (4.28), (4.29), (4.30), and (4.31), respectively [11] as

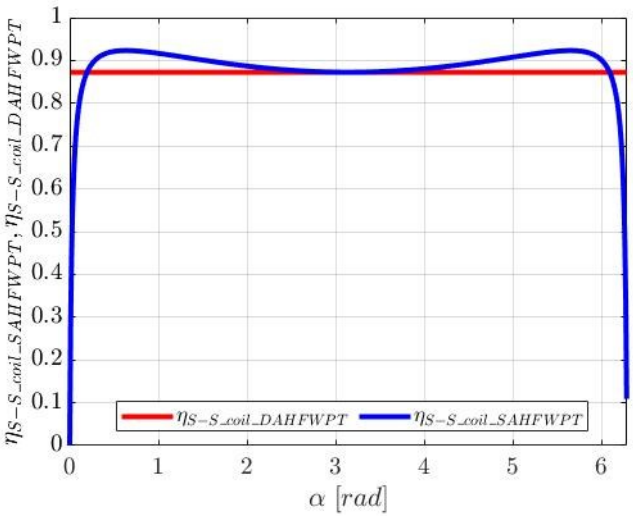

Fig. 4.6 S-S coupling coil efficiency of SAHFWPT and DAHFWPT w.r.t. α.

$$P_{HFSR\_Cond\_loss} = 2i_{S\_1\_rms}^2 R_{SD\_on} + 2V_{SD}\left|i_{S\_1\_avg}\right| \quad (4.28)$$

$$P_{HFSC\_Cond\_loss} = 2i_{S\_1\_rms}^2 R_{SD\_on} + 2V_{SD}\left|i_{S\_1\_avg}\right| \quad (4.29)$$

$$P_{HFPC\_Cond\_S\_loss} = 2i_{P\_S\_1\_rms}^2 R_{SD\_on} \quad (4.30)$$

$$P_{HFPC\_Cond\_D\_loss} = 2i_{P\_D\_1\_rms}^2 R_{SD\_on} \quad (4.31)$$

where $i_{P\_D\_1\_avg}$ and $i_{S\_1\_avg}$ are the average currents flowing in the diodes of the HFPC and HFSR in half of the switching period. From the data sheet of SiHG33N60EF, R_{SD_on} results in about 0.085Ω and the diode forward voltage V_{SD} is about 0.9 V.

4.4.2.2. Hard Turn on and off Loss

The switching loss of diodes of MOSFETs for HFSR are zero, as diodes turn on and turn off at zero current, as shown in Fig. 4.3a. However, in the HFSC the body diodes D_9 and D_{12} have hard turn on and turn off at $\frac{-\beta}{2}$ and $\frac{\beta}{2}$ as shown in Fig. 4.3b. The power $P_{HFSC\_on\_off\_loss}$ corresponds to the switching loss of switches for the HFSC and is given by (4.32) in [12,13], the power $P_{HFPC\_on\_off\_S\_loss}$, and $P_{HFPC\_on\_off\_D\_loss}$ are the switching loss of switches for the HFPC for SAHFWPT and DAHFWPT, respectively, and they are provided by (4.33) and (4.34), respectively as

$$P_{HFSC\_on\_off\_loss} = \frac{1}{2} f_r V_{O\_D} I_{on} t_{on} + \frac{1}{2} f_r V_{O\_D} I_{off} t_{off} \quad (4.32)$$

$$P_{HFPC\_on\_off\_S\_loss} = \frac{1}{2} f_r V_{DCP\_S} I_{on} t_{on} + \frac{1}{2} f_r V_{DCP\_S} I_{off} t_{off} \quad (4.33)$$

$$P_{HFPC\_on\_off\_D\_loss} = \frac{1}{2} f_r V_{DCP\_D} I_{on} t_{on} + \frac{1}{2} f_r V_{DCP\_D} I_{off} t_{off} \quad (4.34)$$

From the data sheet of SiHG33N60EF, t_{on} and t_{off} are 28ns and 161ns, respectively. I_{on} and I_{off} are on the and off current of $i_{S\_1\_rms}$ at $\frac{-\beta}{2}$ and $\frac{\beta}{2}$ in the HFSC shown in Fig. 4.3b. I_{on} and I_{off} are the on and off current of $i_{P\_S\_1\_rms}$; I_{on} and I_{off} are on and off current of $i_{P\_D\_1\_rms}$ current at $\Phi - \frac{\alpha}{2}$ and $\Phi + \frac{\alpha}{2}$ in the HFPC for the SAHFWPT and DAHFWPT shown in Fig. 4.3a and 4.3b, respectively.

4.4.2.3. Other Switching Losses in the MOSFET

Apart from the above losses of the MOSFET, the overall switching loss estimation depends on some other losses. Such as, output capacitance C_{OSS} and body diode reverse recovery losses. When MOSFETs turn off, the energy stored in the C_{OSS} discharges through the body diode and originates the turn on loss provided in [22]. The P_{Coss_loss} in C_{OSS} is expressed in Equation (4.35) as

$$P_{Coss\_loss} = \frac{1}{2} f_r C_{oss} V_{DS}^2 \quad (4.35)$$

From the data sheet of SiHG33N60EF $C_{oss} = 154\ pF$, the switching frequency is same as resonating frequency $f_r = 85$ kHz and the drain to source voltage V_{DS} is the same as the voltage applied across the converter.

The body diode reverse recovery takes place [10], therefore the diode turns off while carrying a positive forward current due to the large reverse time t_{rr}. The relation for body diode reverse recovery loss P_{body_loss} is as follows

$$P_{body\_loss} = f_r Q_{rr} V_{off} \quad (4.36)$$

where V_{off} is the forward voltage drop of the diode during the conduction. $Q_{rr} = 2\mu C$ is the reverse recovery charge.

4.5. Efficiency of SAHFWPT and DAHFWPT

The efficiency is the ratio of the output power to the input power of any system. The general expression for efficiency is

$$\eta = \frac{P_O}{P_{in}} \tag{4.37}$$

whereas $P_{in} = P_O + P_{loss}$ with P_{loss} denoting the overall losses of the system, P_{in} represents the input power and P_O represents the output power. Equation (4.37) express the overall efficiency of the system. However, overall efficiency expression for SAHFWPT and DAHFWPT follow Equation (4.37). and are represented as $\eta_{SAHFWPT}$ and $\eta_{DAHFWPT}$ and formulated in Equation (4.38) and (4.39), respectively.

$$\eta_{SAHFWPT} = \frac{P_B}{P_B + P_{SAHFWPT\_loss}} \tag{4.38}$$

$$\eta_{DAHFWPT} = \frac{P_B}{P_B + P_{DAHFWPT\_loss}} \tag{4.39}$$

where P_B represents the power at the battery end. $P_{SAHFWPT\_loss}$ and $P_{DAHFWPT\_loss}$ represent the overall loss of the SAHFWPT and DAHFWPT, respectively. They can be subdivided into the contributions provided by

$$\begin{aligned} P_{SAHFWPT\_loss} = {} & P_{S-S\_coil\_SAHFWPT\_loss} + P_{HFSR\_Cond\_loss} + \\ & P_{HFPC\_Cond\_S\_loss} + P_{Coss\_loss} + P_{body\_loss} + P_{HFPC\_on\_off\_S\_loss} \end{aligned} \tag{4.40}$$

$$\begin{aligned} P_{DAHFWPT\_loss} = {} & P_{S-S\_coil\_DAHFWPT\_loss} + P_{HFSC\_Cond\_loss} \\ & + P_{HFPC\_Cond\_D\_loss} + P_{Coss\_loss} + P_{body\_loss} \\ & + P_{HFPC\_on\_off\_D\_loss} + P_{HFSC\_on\_off\_loss} \end{aligned} \tag{4.41}$$

The Equations (4.40) and (4.41) represent the overall loss of the WPT system. That includes coil loss, conduction loss of switch, output capacitor of MOSFET discharging time loss, diode, body diode reverse recovery loss, and converter on and off losses are included for both the SAHFWPT and DAHFWPT system.

The input power of SAHFWPT and DAHFWPT system are represented in equations (4.42) and (4.43), respectively.

$$P_{in\_SAHFWPT} = P_B + P_{SAHFWPT\_loss} \tag{4.42}$$

$$P_{in\_DAHFWPT} = P_B + P_{DAHFWPT\_loss} \tag{4.43}$$

Where P_B denotes the power absorbed by the battery.

4.6. Simulation Results

The SAHFWPT and DAHFWPT in Fig. 4.2a,b were simulated in MATLAB with the parameters specified in Table 4.4. This section presents the discussion about the overall losses and the efficiency of the system, described by the loss characteristics and efficiency curve.

Voltage and current plots in Fig. 4.7a refer to SAHFWPT, the solid blue line represent the output voltage of HFPC and the input voltage of HFSR in steady state and the corresponding currents using the solid red lines. Voltage and current plots in Fig. 4.7b refer to DAHFWPS, the solid blue line the output voltage of HFPC and input voltage of HFSC in steady state, and the corresponding currents using the solid red lines. For a clear viewing of the current, the primary current and the secondary current are multiplied by the factors 20 and 3, respectively. Due to resonating behaviour of the S-S coupling coil, the currents of primary and secondary coils are sinusoidal in nature and the voltage are a quasi-square wave. The input power ratings are 1252 W and 472 W at $\alpha = 0.73$ for SAHFWPT and DAHFWPT, respectively.

It will be investigated with Table 4.5 data that can be taken from the several MATLAB simulation operations. The total loss of the system is calculated using equations (4.21–4.23). This table is formed by taking the condition with the internal phase shift angle α of HFPC and internal phase shift angle β of HFSC, the internal phase shift angle HFPC is same as the HFSC but the internal phase shift angle HFSR is fix at β=π. The respective parameters include the comparative data between in SAHFWPT and DAHFWPT in term of input power, loss of WPT system and efficiency, in Table 4.5. When we look at Table 4.5. Its divided into four column section: the first column includes the internal phase shift angle, the second column includes the input power of SAHFWPT and DAHFWPT, the third column includes the complete loss of SAHFWPT and DAHFWPT, the fourth column includes the complete loss in percentage of SAHFWPT and DAHFWPT, respectively. Table 4.5 first column contains the various value of α. For the analysis, we consider α equal to β as a reference value. Further, input power, complete loss of the system, and complete loss in percentage are further subdivided into two column sections, the second and third columns are associated with decreases in input power for SAHFWPT and DAHFWPT, the fourth and fifth columns are associated with decreases in complete losses for SAHFWPT and DAHFWPT, and the second and third columns are associated with decreases in complete percentage losses for SAHFWPT and DAHFWPT, respectively.

From the analytical data reported in Table 4.5, the percentage losses of SAHFWPT decrease as α decreases, but near to zero value of α, percentage losses increase. On the contrary, in the case of DAHFWPT, losses percentage is almost constant as α decreases but, as it happens with SAHFWPT, near to the zero value of α loss percentage increases and losses in DAHFWPT are higher than losses in SAHFWPT. However, the instantaneous input power of SAHFWPT and DAHFWPT at $\alpha = 0.33$ are 604 W and 102 W. These results are obtained at Φ = 3π/2.

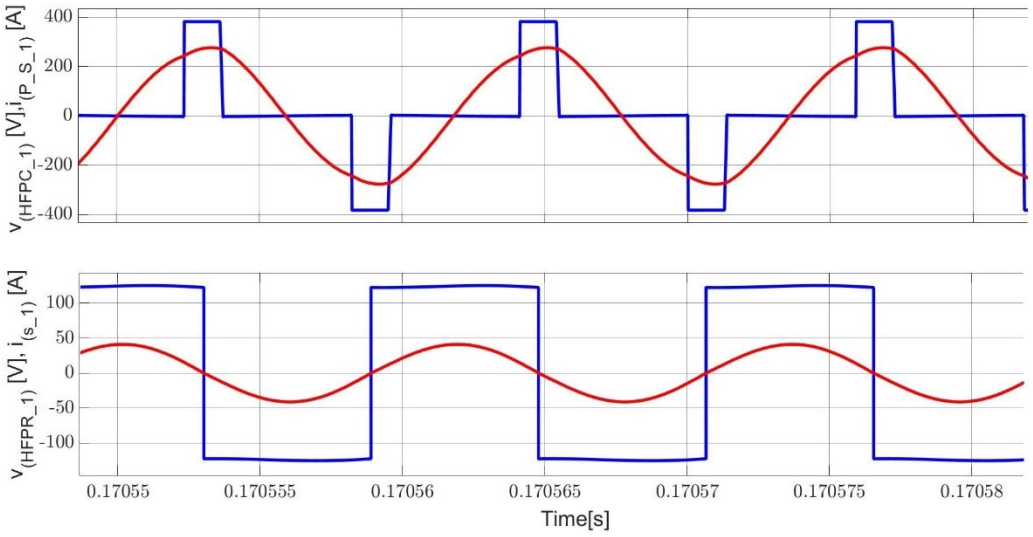

(a)

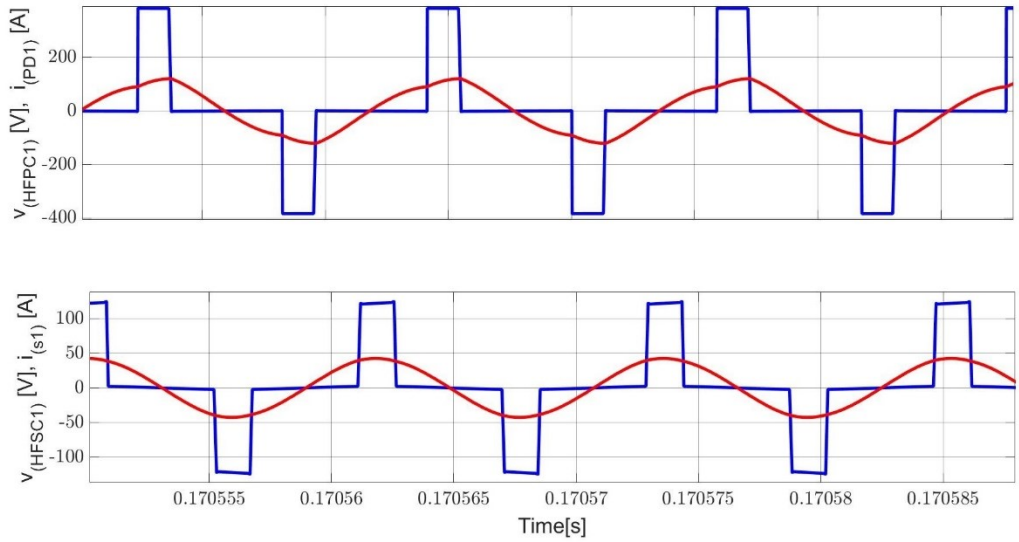

(b)

Fig. 4.7 Current (red) and voltage (blue) wave input of primary coil and output of the secondary coil of (a) SAHFWPT (b) and DAHFWPT.

Table 4.5. Overall loss analytical data for SAHFWPT and DAHFWPT at $\Phi = 3\pi/2$ and $\alpha = \beta$

A	Input Power		Loss into the System		% Loss into the System	
	SAHFWPT	DAHFWPT	SAHFWPT	DAHFWPT	SAHFWPT	DAHFWPT
3.12	3605	3605	586	586	16.25	16.25
2.16	3146	2807	469	453	14.97	16.15
1.82	2795	2252	388	361	13.87	16.05
1.44	2312	1574	290	250	12.54	15.88
1.14	1881	1057	217	165	11.51	15.65
0.73	1245	467	136	71	10.94	15.23
0.33	605	102	99	23	16.34	22.43

Fig. 4.8a,b show the steady state input power and the loss curves of the SAHFWPT in solid blue line and DAHFWPT in solid red line. The input power of the system is in the range of 0

to 3600 W. As per Equation (18), SAHFWPT input power is always greater than DAHFWPT at equal α apart from $\alpha = \pi$. Both input power and loss curve are symmetric with respect to $\alpha = 3.14$. From the loss curve, it is visible that the losses in SAHFWPT are always greater than losses in DAHFWPT. Consequently, for the same instantaneous input power in both systems, the losses are not same. For example, at the input power equal to 2004 W indicated by data tip at $\alpha = 1.68$ and $\alpha = 5.06$, the losses are 320 W and 236 W for the DAHFWPT and the SAHFWPT, respectively. From the above discussion and Table 4.5 data, it is proven that the losses of SAHFWPT are less than or equal to the DAHFWPT.

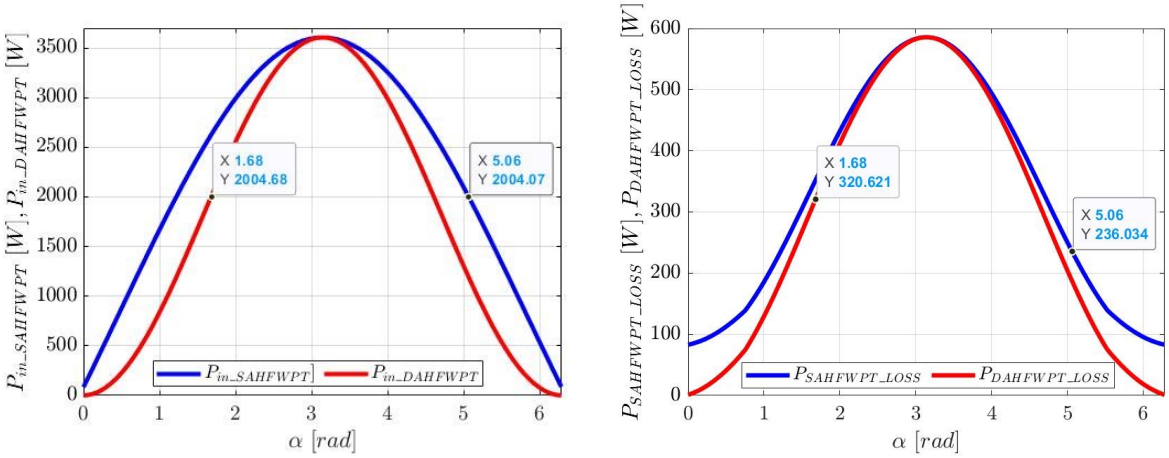

(a) (b)

Fig. 4.8.(a) Input power (b) overall losses of the system w.r.t. α.

To replicate the losses of the complete system, as mentioned in Fig. 4.8b. Further, it will be investigated in detail with Table 4.6 data that can be taken from the several MATLAB simulation operations. This table is form by taking the condition with the equal instantaneous input power, and respective parameters includes the comparative data between in SAHFWPT and DAHFWPT in term of efficiency, primary and secondary current, and internal phase shift angle α and β, whereas α = β in case of DAHFWPT and β= π fixed in case of SAHFWPT in Table 4.6. When we look at Table 4.6. Its divided into two column sections of WPT converters arrangement, SAHFWPT and DAHFWPT, respectively. Both arrangement are further subdivided into six column section: the first and second sub columns are associated with the internal phase shift angles α and β, third and fourth sub column are associated with the input power and efficiency of WPT system, fifth and sixth sub column are associated with the primary and secondary s-s coil current of WPT system.

The equal instantaneous input power 1252 W of SAHFWPT and DAHFWPT is given in Table 4.6. The efficiencies of SAHFWPT and DAHFWPT converters are 89.13% and 84.31%, respectively. The primary and secondary coil RMS currents of SAHFWPT and DAHFWPT converters are 8.99 A, 10.33 A and 5.28 A, 16.91 A, respectively, and are drawn from the source to maintain the input power equal. To limit these current the internal phase shift angle α of HFPC in the case of the SAHFWPT and DAHFWPT operation are 0.234π and 0.4 π. While, the internal phase shift angle β of the HFSR and HFSC in the case of the SAHFWPT and DAHFWPT operation are π and 0.4 π, respectively. The above explanation is for the one case

of study w.r.t. the input power. Several case study in terms of different instentatenious input power was mentions in Table 4.6.

From the above explanation, it is clear that for the same instantaneous input power, the primary and secondary coil currents in SAHFWPT and DAHFWPT are not equal shown in. Fig 4.9(a) and (b) by the bar chart for primary current blue and secondary current orange w.r.t. instantaneous efficiencies of SAHFWPT and DAHFWPT, respectively.The RMS current relation is obtained from equations (4.21 to 4.23). The well-known value of internal resistance (paracetic resistance) R_P, R_S in primary and secondary of s-s coils is 0.5 Ω, as mentioned in Table 4.4. That could be used to calculate the losses into the coils by using the primary and secondary RMS currents of the coils from equations (4.21) to (4.23) of SAHFWPT and DAHFWPT, respectively.

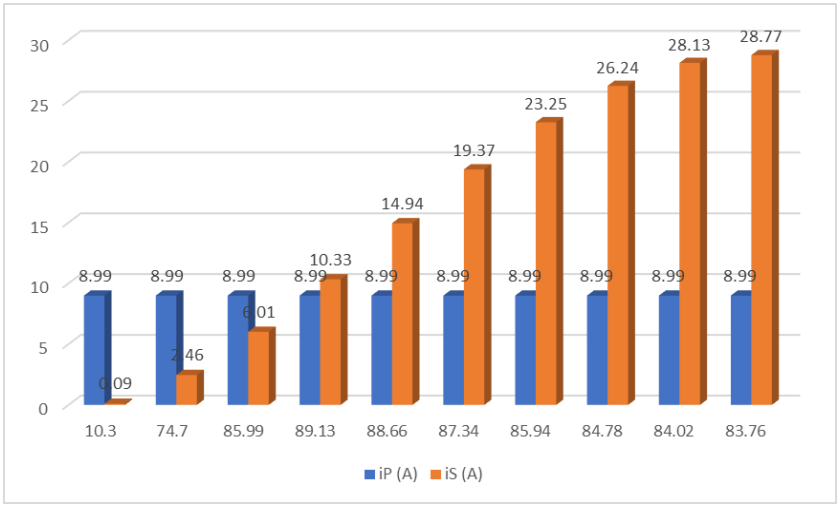

(a)

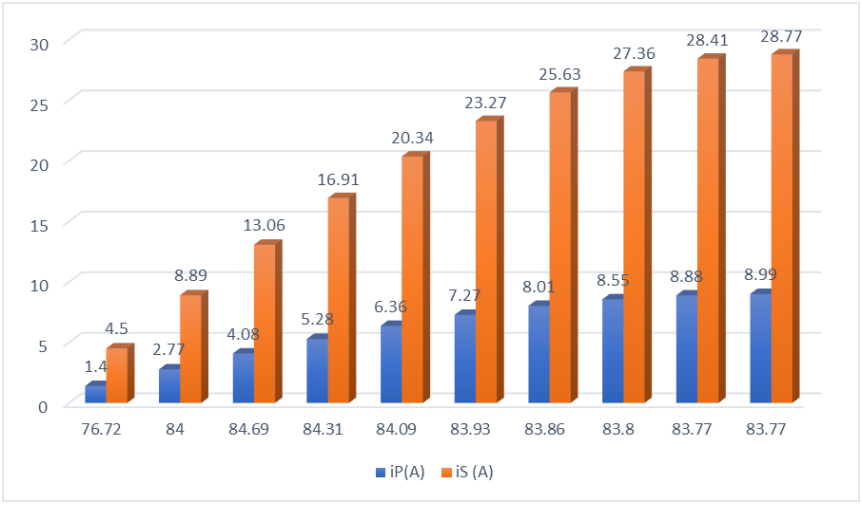

(b)

Fig. 4.9 Bar chart for primary current blue and secondary current orange w.r.t. instantaneous efficiency (a) SAHFWPT (b) DAHFWPT

Table 4.6. Overall loss analytical data for SAHFWPT and DAHFWPT at Φ = 3π/2 and α are not equal β

SAHFWPT						DAHFWPT					
α	**β**	**Pin(W)**	**H**	**i_P(A)**	**i_S(A)**	**A**	**β**	**Pin(W)**	**η**	**i_P(A)**	**i_S (A)**
0.002π	π	92.04	10.3	8.99	0.09	0.1π	0.1π	92.04	76.72	1.4	4.5
0.0544π	π	350	74.7	8.99	2.46	0.2π	0.2π	350	84	2.77	8.89
0.134π	π	750	85.99	8.99	6.01	0.3π	0.3π	750	84.69	4.08	13.06
0.234π	π	1252	89.13	8.99	10.33	0.4π	0.4π	1252	84.31	5.28	16.91
0.34764π	π	1808	88.66	8.99	14.94	0.5π	0.5π	1808	84.09	6.36	20.34
0.4705π	π	2363	87.34	8.99	19.37	0.6π	0.6π	2363	83.93	7.27	23.27
0.599π	π	2864	85.94	8.99	23.25	0.7π	0.7π	2864	83.86	8.01	25.63
0.731π	π	3261	84.78	8.99	26.24	0.8π	0.8π	3261	83.80	8.55	27.36
0.8657π	π	3517	84.02	8.99	28.13	0.9π	0.9π	3517	83.77	8.88	28.41
π	π	3605	83.76	8.99	28.77	π	π	3605	83.77	8.99	28.77

Fig. 4.10a presents efficiency plots, i.e., $\eta_{SAHFWPT}$ in solid blue line and $\eta_{DAHFWPT}$ in solid red line as a function of the internal phase shift angle α, obtained from (4.38) and (4.39) for the SAHFWPT and DAHFWPT, respectively. Both the maximum efficiencies of the SAHFWPT and DAHFWPT, i.e., 89.2% and 84.9%, are reached at $\alpha = 0.73$, respectively. The efficiencies $\eta_{SAHFWPT}$ and $\eta_{DAHFWPT}$ have two picks at $\alpha = 0.73$ and 5.55. For α in the ranges from 0.73 to 2.3 and from 3.98 to 5.55 the efficiency $\eta_{SAHFWPT}$ is always greater than $\eta_{DAHFWPT}$. Moreover, in these range of $\eta_{DAHFWPT}$ the results nearly constant. For α ranging in the interval from 2.3 to 3.98, the efficiency $\eta_{SAHFWPT}$ is almost equal to $\eta_{DAHFWPT}$.

Fig. 4.10b reports the efficiency plots as a function of the input power $P_{SAHFWPT}$ and $P_{DAHFWPT}$, obtained from (38) and (39), respectively. The maximum efficiencies of 89.2% and 84.9% of SAHFWPT and DAHFWPT are reached at $P_{SAHFWPT} = 1325$ W and $P_{DAHFWPT} = 491$ W, respectively. It is visible that the operating conditions of the SAHFWPT and DAHFWPT can be divided into two zones. When power $P_{SAHFWPT}$ is in the interval [648 W 3606 W], efficiency $\eta_{SAHFWPT}$ is greater than efficiency $\eta_{DAHFWPT}$. However, for the input power $P_{DAHFWPT}$ less than 648 W, the efficiency $\eta_{DAHFWPT}$ is greater than the efficiency $\eta_{SAHFWPT}$.

At the end of the study and their losses comparison of SAHFWPT and DAHFWPT, we are able to decide the superiority of the DC–DC converters, in terms of efficiency and input power. As per the above discussion, the efficiency performance of the SAHFWPT is greater than that of DAHFWPT in the medium power range. Indeed, at medium power the efficiency of the SAHFWPT is 4.3% more than the efficiency of the DAHFWPT. Whilst for the low power range the efficiency of the SAHFWPT is approximately 12% less than the efficiency of the DAHFWPT.

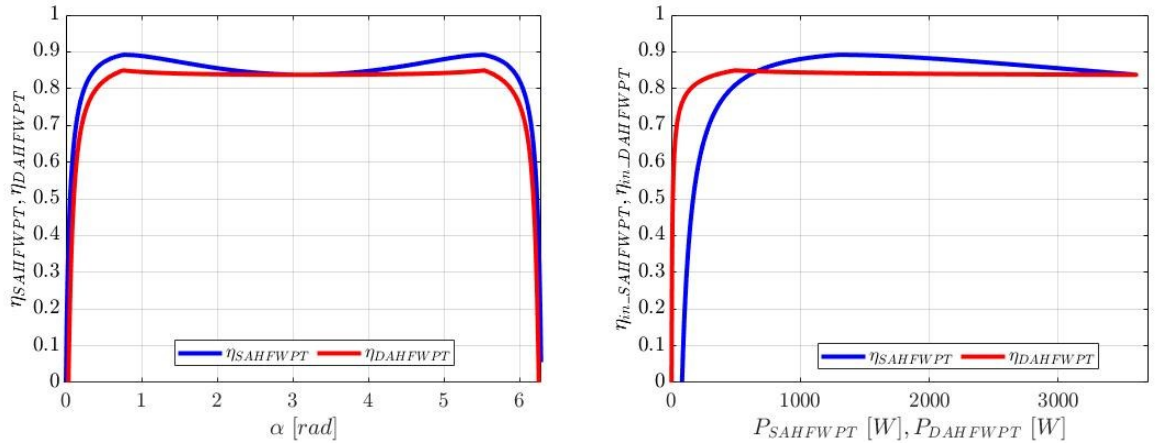

(a) (b)

Fig. 4.10 Efficiency of WPT system (a) w.r.t. α (b) w.r.t. $P_{SAHFWPT}$ and $P_{DAHFWPT}$.

4.7. Conclusions

This chapter presents a step-by-step comparison study of the losses at different stages of converters and S-S coupling coils together with the control approaches of primary and secondary converters of the SAHFWPT and DAHFWPT, respectively, at a domestic load, i.e., domestic load input power up to 3600 W. This includes the uni-directional power flow estimation at each stage of the WPT system, such as the HFPC, primary coil, secondary coil, HFSC, and HFSR. The power assessment includes the estimation of system losses considering the switches losses, conduction losses, hard turn on and off losses, and S-S coil losses, etc. These estimations of the power are performed according to the SAE J2954 and the domestic grid power. To analyse the comparative performance of SAHFWPT and DAHFWPT, the two different converters control approaches, i.e., EPS and DPS methods took place by varying the internal and external phase shift angle. This was further verified through MATLAB, and the respective power loss and efficiency plots were drawn. Following from the simulation result discussion reported in Section 5 about the loss and efficiency of the SAHFWPT and the DAHFWPT, the efficiency of the SAHFWPT converter was found always superior at the medium power level of domestic use, i.e., 89.2%. Indeed, it has approximately 4% higher efficiency. Whereas in the lower and higher power ranges, the DAHFWPT is more efficient than the SAHFWPT with this method of control.

The literature has reported about the use of the SAHFWPT and DAHFWPT system to control the battery current during charging. Indeed, charging through the SAHFWPT needs one more DC–DC converter to control the battery charging. Nevertheless, since the efficiency of SAHFWPT is higher than that of DAHFWPT in medium power range of domestic use, we have a new result: if we are able to design the secondary DC–DC converter (i.e., chopper) having approximately 98% efficiency, then the SAHFWPT is superior in terms of efficiency at medium power of domestic use.

4.8. Reference

1. Chen, T., Zhang, X.-P., Wang, J., Li, J., Wu, C., Hu, M., Bian, H "A Review on Electric Vehicle Charging Infrastructure Development in the UK," J. Mod. Power Syst. Clean Energy, 2020, 8, pp. 193–205.

2. Far, M.F. Paakkinen, M. Cremers, P. "A Framework for Charging Standardisation of Electric Buses in Europe," In Proceedings of the IEEE Vehicle Power and Propulsion Conference, Gijon, Spain, 2020, pp. 1–4.

3. Bertoluzzo, M., Giacomuzzi, S., Kumar, A "Design of a Bidirectional Wireless Power Transfer System for Vehicle-to-Home Applications," Vehicles ,2021, 3, pp. 406–425.

4. Fontana, C., Forato, M., Bertoluzzo, M., Buja, G. "Design characteristics of SAB and DAB converters," In Proceedings of the Intl Aegean Conference on Electrical Machines & Power Electronics (ACEMP) Intl Conference on Optimization of Electrical & Electronic Equipment (OPTIM) & Intl Symposium on Advanced Electromechanical Motion Systems (ELECTROMOTION), Side, Turkey, 2015; pp. 661–668.

5. Jha, R.; Forato, M.; Prakash, S.; Dashora, H.; Buja, G. An Analysis-Supported Design of a Single Active Bridge (SAB) Converter. Energies, 2022, 15, 666.

6. Zhao, B., Song, Q., Liu, W., Sun, Y. "Overview of Dual-Active-Bridge Isolated Bidirectional DC–DC Converter for High-Frequency-Link Power-Conversion System," IEEE Trans. Power Electron, 2014, 29, pp. 4091–4106.

7. Xu, F., Wong, S.C., Tse, C.K. "Overall Loss Compensation and Optimization Control in Single-Stage Inductive Power Transfer Converter Delivering Constant Power," IEEE Trans. Power Electron, 2022, 37, pp. 1146–1158.

8. Di Capua, G., Femia, N., Petrone, G., Lisi, G., Du, D. Subramonian, R. Rajaram Subramonian. "Power and efficiency analysis of high-frequency Wireless Power Transfer Systems," Int. J. Electr. Power Energy Syst., 2017, 84, pp. 124–134.

9. J2954: Wireless Power Transfer for Light-Duty Plug-In/Electric Vehicles and Alignment Methodology; SAE International: Warrendale, PA, USA, 2020.

10. Gonzalez-Gonzalez, J.M., Trivino-Cabrera, A., Aguado, J.A. "Assessment of the Power Losses in a SAE J2954-Compliant Wireless Charger," IEEE Access, 2022, 10, pp. 54474–54483.

11. Ravikiran, V., Keshri, R., Rathore, A., Chakraborty, C. "Loss Analysis of Resonant Inductive Power Transfer System for Wireless Charging of e-Rickshaw," In Proceedings of the IEEE 28th International Symposium on Industrial Electronics (ISIE), Vancouver, BC, Canada, 2019, pp. 2559–2564,.

12. Di Capua, G., Femia, N., Lisi, G. "Impact of losses and mismatches on power and

efficiency of Wireless Power Transfer Systems with controlled secondary-side rectifier," Integration, 2016, 55, pp. 384–392.

13. Acquaviva, A., Rodionov, A., Kersten, A., Thiringer, T., Liu, Y. "Analytical Conduction Loss Calculation of a MOSFET Three-Phase Inverter Accounting for the Reverse Conduction and the Blanking Time," IEEE Trans. Ind. Electron, 2021, 68, pp. 6682–6691.

14. Kalra, G.R., Pearce, M.G.S., Kim, S., Thrimawithana, D.J., Covic, G.A. "A Power Loss Measurement Technique for Inductive Power Transfer Magnetic Couplers," IEEE J. Emerg. Sel. Topics Ind. Electron, 2020, 1, pp. 113–122.

15. Carretero, C. "Coupling Power Losses in Inductive Power Transfer Systems with Litz-Wire Coils," IEEE Trans. Ind. Electron, 2017, 64, pp. 4474–4482.

16. Rossmanith, H., Doebroenti, M., Albach, M., Exner, D. "Measurement and Characterization of High Frequency Losses in Nonideal Litz Wires," IEEE Trans. Power Electron, 2011, 26, pp. 3386–3394.

17. Ren, Y., Xu, M., Zhou, J., Lee, F. "Analytical loss model of power MOSFET," IEEE Trans. Power Electron, 2006, 21, pp. 310–319.

18. Huang, Z., Lam, C.S., Mak, P.I., Martins, R.S., Wong, S.C., Tse, C.K. "A Single-Stage Inductive-Power-Transfer Converter for Constant-Power and Maximum-Efficiency Battery Charging," IEEE Trans. on Power Electron, 2020, 35, pp. 8973–8984.

19. Fu, M., Tang, Z., Liu, M., Ma, C., Zhu, X. "Full-bridge rectifier input reactance compensation in Megahertz wireless power transfer systems," In Proceedings of the IEEE PELS Workshop on Emerging Technologies: Wireless Power, Daejeon, Republic of Korea, 2015; pp. 1–5.

20. Enssle, A., Parspour, N. "Power Loss Shifted Design of Inductive Energy Transfer Systems," IEEE Open J. Power Electron, 2020, 1, pp. 113–123.

21. Shiba, K., Morimasa, A., Hirano, H. "Design and Development of Low-Loss Transformer for Powering Small Implantable Medical Devices," IEEE Trans. Biomed. Circuits Syst, 2010, 4, pp. 77–85.

22. Di Capua, G., Sánchez, J.A., Cabrera, A.T., Cabrera, D.F., Femia, N., Petrone, G., Spagnuolo, G. "A losses-based analysis for electric vehicle wireless chargers," In Proceedings of the International Conference on Synthesis, Modeling, Analysis and Simulation Methods and Applications to Circuit Design, 2015; pp. 1–4.

23. Sagar, A., Kumar, A., Bertoluzzo, M., Jha, R.K. "Analysis and Design of a Two-winding Wireless Power Transfer System with Higher System Efficiency and Maximum Load Power," IECON 2022—48th Annual Conference of the IEEE Industrial

Electronics Society, 2022; pp. 1–6.

24. Van Mulders, J., Delabie, D., Lecluyse, C., Buyle, C., Callebaut, G., Van der Perre, L., De Strycker, L. “Wireless Power Transfer: Systems, Circuits, Standards, and Use Cases,” Sensors, 2022, 22, pp. 5573.

25. Turzyński, M., Bachman, S., Jasiński, M., Piasecki, S., Ryłko, M., Chiu, H.-J., Kuo, S.-H., Chang, Y.C. “Analytical Estimation of Power Losses in a Dual Active Bridge Converter Controlled with a Single-Phase Shift Switching Scheme,” Energies, 2022, 15, pp. 8262.

26. Oggier, G.G., García, G.O., Oliva, A.R. “Switching Control Strategy to Minimize Dual Active Bridge Converter Losses,” IEEE Trans. Power Electron, 2009, 24, pp. 1826–1838.

27. Bai, H., Mi, C. “Eliminate Reactive Power and Increase System Efficiency of Isolated Bidirectional Dual-Active-Bridge DC–DC Converters Using Novel Dual-Phase-Shift Control,” IEEE Trans. Power Electron, 2008, 23, pp. 2905–2914.

Chapter 5

Analysis and comparisons of reactive power control state for the V2H wireless power transfer system

5.1 Introduction

THE ability of electric vehicles to serve as both flexible loads and mobile generators will make them a valuable asset in power grids, smart grids, and micro grids of future. The purpose of this study is to investigate these aspects in the context of a wireless power transfer in term of V2H, which can be considered in terms of a micro grid, and reports the considerable advantages for vehicle owner. In order to provide a full suite of V2H services, electric vehicle chargers will need to be upgraded to bidirectional power flow. As a result, it is crucial for these systems to account for the adjustments needed to supply power in both directions. This chapter compares the effects of the different states of the control signals in between primary and secondary H-bridge by looking at the EV's active and reactive power consumption and generation, respectively. Series-Series compensation is an important element in the area of wireless charging and it is the foundation of the control strategy. Based on the results of an analytical investigation, it seems that the controller can work with a wide range of active and reactive power setups in the wireless power transfer between primary and secondary side of converters.

5.2 Background and application of DC to DC BWV2H converter

Electric vehicles may be refuelled in two ways: conductive charging and wireless charging. While charging by cable is common, it does have certain drawbacks. Most notably, difficulties with wires being entangled, and there have been concerns raised regarding its viability in damp environments. [1]. Wireless power transfer overcome above issues [2]. When compared to the traditional conductive method, wireless charging of electric vehicle's battery offers several advantages such as i) elimination of plug, cable, outlet; ii) simplify the charging procedure; iii) safe energy transfer in any environment condition; etc. [3].

Fig.1.1. from chapter one depicts a resonant WPT system's architecture. On primary section, the grid supplies power to the coil through converters that function as an AC-AC converter operating at grid frequency at input and producing high frequencies output, in range of 79-90 kHz, as per SAE J2954 standard [4]. The primary coil is inductively coupled with secondary. The voltage induced across the secondary coil is used to charge the battery pack through AC-DC converter, by regulating current and voltage [5].

The current proliferation of distributed power generation has also prompted academics to investigate the use of bidirectional battery chargers to realize the Grid-To-Vehicle and Vehicle-To-Grid concepts, which involves employing EVs as the power source [6]. V2G is a notion that stems from the principle of active demand, in which the end-user serves as both an energy consumer and generator, which can further realize in term of Home-to-Vehicle and Vehicle-to-Home [7]. In this context, the Bidirectional WPT could lessen the operating expense of EVs and hence lowering the total cost of ownership of EV [8].

This chapter contributes in design and implementation of V2H by BWV2H [9] to charge and discharge EV as per requirements of load by configuring two high frequency H-bridge converters and S-S compensated coupling coil. By the help of MATLAB/ Simulation we

investigate control approach i.e., based on the dual phase shift (DPS) control [10],[11]. The control approach is based on comparative mathematical study at different state of active and reactive power flow in between primary and secondary DC bus and EV battery [12]. With this study we are able to understand the effects of reactive power in WPT system, and to analyse the consequent efficiency and VA rating of the system [13].

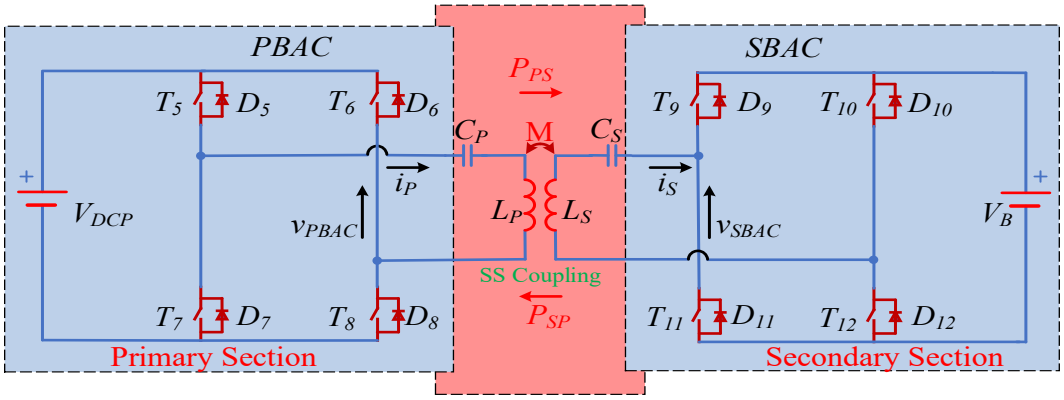

Fig. 5.1 BWV2H Topology of primary and secondary H-bridge converters

The schematic of the DAHFWPT converter with equivalent load in Fig. 4.4 b has been redrawn in Fig. 5.1 with the distinct nomenclatures that will be the one of the power transfer converter section of BWV2H system. This was done to prevent any confusion between the application area and the relation that we use to study this system. It depicts a typical BWV2H converter setup for V2H. In this chapter, we are focusing on control operation of primary and secondary H-bridge converters to regulate active and reactive power in DC-to-DC BWV2H converter [9]. The two converters are denoted as Primary Bi-direction active converter (PBAC) and secondary Bi-directional active converters (SBAC). The switching operation of converters takes place by MOSFET (T_5, T_{12}), and anti-parallel diode (D_5, D_{12}). These converters are connected through S-S compensated coils, represented in Fig. 5.1 as capacitors C_P, C_S, inductors L_P, L_S and mutual inductor M. The currents i_P, i_S are sinusoidal due to the resonance and v_{PBAC}, v_{SBAC} output and input voltages PBAC and SBAC have a quasi-square waveform, as shown in Fig.5.2.

However, PBAC and SBAC of BWV2H are operating at 85 kHz resonating frequency. Fig. 5.2 depicts a typical switching operation and respected voltage, current wave form of BWV2H topology of primary and secondary H-bridge converters at unity power factor. To regulate power flow of BWV2H, as per to fulfil the power demand by EVs and load can be achieved by using phase shift control i.e., Dual phase shift (DPS). To mitigate control complexity of the analysis we choose DPS control, in which we consider the internal phase shift (IPS) α and β of of PBAC and SBAC, respectively, to be equal, i.e. ($\alpha = \beta$). The DPS control does not end with the internal phase shift angle; Consequently, the power flow depends on the external phase shift (EPS) angle Φ. When the fundamental voltage and current of the primary converter are lagging by the secondary converter through the angle Φ. Active power will flow from the primary to the secondary and vice versa for reversal direction of the of the BWV2H system, when Φ is either +90 or -90. However, the system operates at the maximum efficiency in either direction

in this condition. It is only possible when the chosen system is lossless. But in real time, some loss always available in to the system, due to the parasitic resistance of the system components. Apart from loss, reactive power is also an important factor that affects the efficiency of the system.

Each power state of BWV2H operation in Fig.5.3 are associate with switching operation of converters w.r.t gating signal in Fig. 5.2. The eight state PBAC and SBAC with the DPS control method of BWV2H in unidirectional operation are explain i.e., when power flow from primary to secondary side take place i.e., forward mode. We are not going to explain the reverse mode of operation as the operation mode are similar as forward mode.

1. T_7, T_8 and T_9, T_{12} having gating signal at t0-t1: this is the passive phase for the primary converter, the current i_P is circulating through the T8 and D7, Even the circulating current not reach the primary DC side so v_{PBAC} is zero as shown in Fig 5.3(a) and the primary instantaneous current at t0 is zero. Due to resonating behaviour of coil at time t0, L_P is discharging and during same time capacitor C_P charging from negative pick toward positive pick till time t1, as gating operation shown in Fig. 5.2. However, in the interval t0-t1, this is the active phase of the secondary converter, i_S current is flowing through secondary coil, diode D_9 and D_{12}, further path is complete through battery of EV. In this interval L_S charging towards the positive peck and the C_S discharging towards the negative peck till time t1.
2. T_5, T_8 and T_9, T_{10} having gating signal at t1-t2: this is the active phase of the primary converter, current i_P is flowing through primary MOSFET T_5 and T_8, in this operation current from DC primary source to the primary coil are flowing, at time t1 primary voltage v_{PBAC} is appear across coil as shown in Fig 5.3(b), still in this interval L_P discharging after reaching sudden jump in voltage due to v_{PBAC} and capacitor C_P charging, in this interval as C_P oppose the sudden change in voltage, it continues charging up to t1. At t2 the instantaneous current of primary coil current was the maximum i_P as gating operation shown in Fig. 5.2. However, in interval t1-t2, this is the passive phase for the secondary converter, the current i_S is circulating through the T_{10} and D_9, Even the circulating current not reach the secondary DC side so v_{SBAC} is zero, the i_S current start decreasing from maximum value as shown in the Fig. 5.2 the instantaneous current i_S at t2 is zero. In this interval L_S is still charging towards the positive peck and the C_S discharging towards the negative peck till time t2.
3. T_5, T_8 and T_9, T_{10} having gating signal at t2-t3: Fig 5.3 (c) depicts for interval t2-t3. In this interval the primary converter is still in the active mode so T_5 and T_8 are still in conduction state, however the i_P start decreasing from the maximum. L_P and C_P still following same trend for charge and discharge. However, during the interval t2-t3, the secondary converter operates in the passive phase, the i_S circulate from T_9 and D_{10} and the polarity of i_S become reverse as shown in Fig 5.2 still no current reaches secondary of battery. In t2-t3 interval, L_S start discharging towards the negative pick and C_S start charging towards positive pick as gating operation shown in Fig. 5.2.
4. T_5, T_6 and T_{10}, T_{11} having gating signal at t3-t4 : In the time interval t3-t4 , the primary converter again in passive phase, the i_P current circulating through the T_3 and D_6, i_P

current was in decreasing in nature, the instantaneous current i_P at t4 is zero as gating operation shown in Fig. 5.2 and i_P don't even reach the primary DC bus side. At t3 primary voltage v_{PBAC} is become zero across coil as shown in Fig 5.3(d), still in this interval LP charging after reaching sudden drop in voltage due to v_{PBAC} and capacitor C_P discharging, in this interval as C_P oppose the sudden change in voltage, it continues discharging up to t4. At the same time, the secondary converter in time interval t3-t4 is under the active phase, current i_S from secondary coil to battery of EV is flowing through the D_{10} and D_{11}, However the v_{SBAC} is appear at the input of the converter. Indeed, the instantaneous i_S current at t4 is negative maximum. In this interval the C_S and L_S are charge and discharge as the same as in step 3 up to the time t4.

5. The operation of the converter for first half cycle was explain in the step 1-4. As wave shape of voltage and current for first-half cycle is symmetrical at t4 with second-half cycle shown in Fig. 5.2. A fundamental different appear on the basis of symmetrical switch operating in second half cycle as shown in Fig. 5.3(e), (f), (g) and (h), those switches are (T_6, T_7, T_9 , T_{12}, D_5, D_8, D_{11}, D_{12}) and respective wave form is shown in Fig. 5.2. Indeed, no need explain twice whole process for step 5-8.

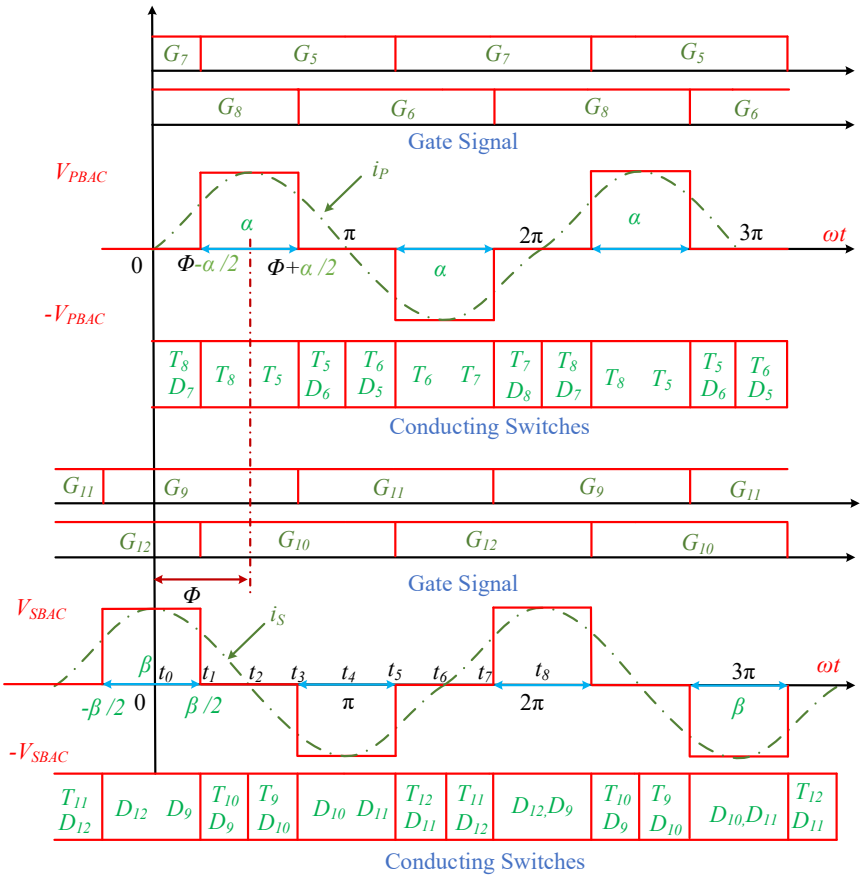

Fig. 5.2 The switching operation and respected voltage, current wave form of BWV2H

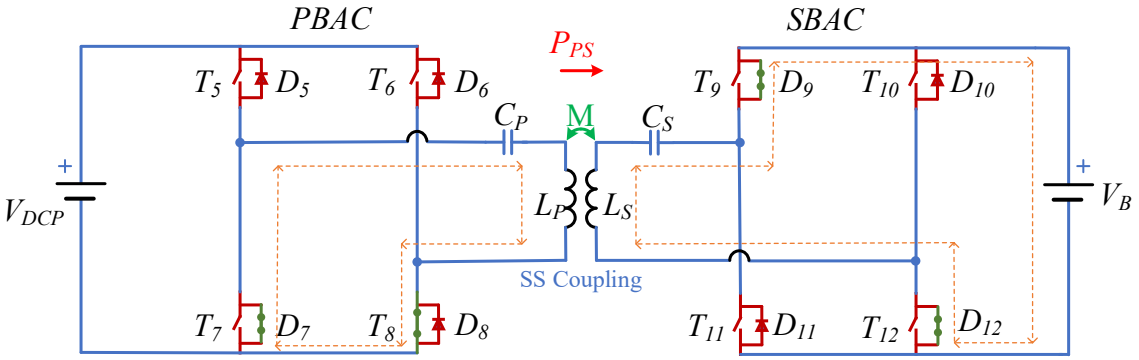
PBAC
SBAC
P_{PS}
T_5 D_5 T_6 D_6
C_P M C_S
T_9 D_9 T_{10} D_{10}
V_{DCP}
L_P L_S
V_B
SS Coupling
T_7 D_7 T_8 D_8
T_{11} D_{11} T_{12} D_{12}

(a)

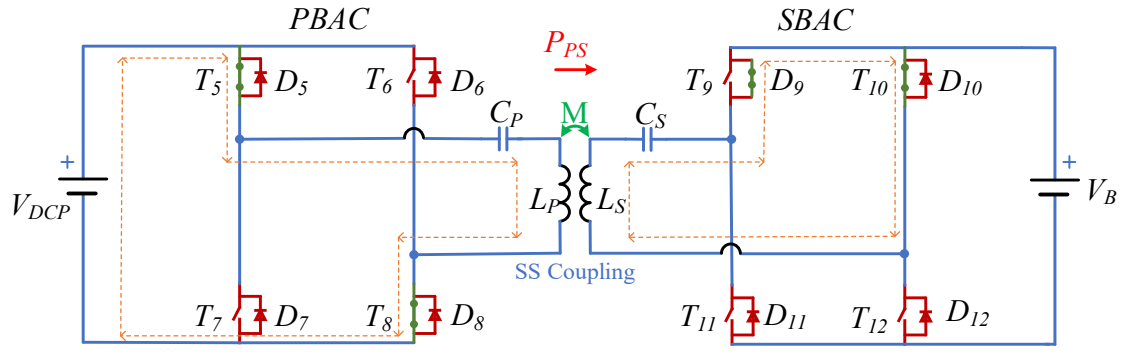
PBAC
SBAC
P_{PS}
T_5 D_5 T_6 D_6
C_P M C_S
T_9 D_9 T_{10} D_{10}
V_{DCP}
L_P L_S
V_B
SS Coupling
T_7 D_7 T_8 D_8
T_{11} D_{11} T_{12} D_{12}

(b)

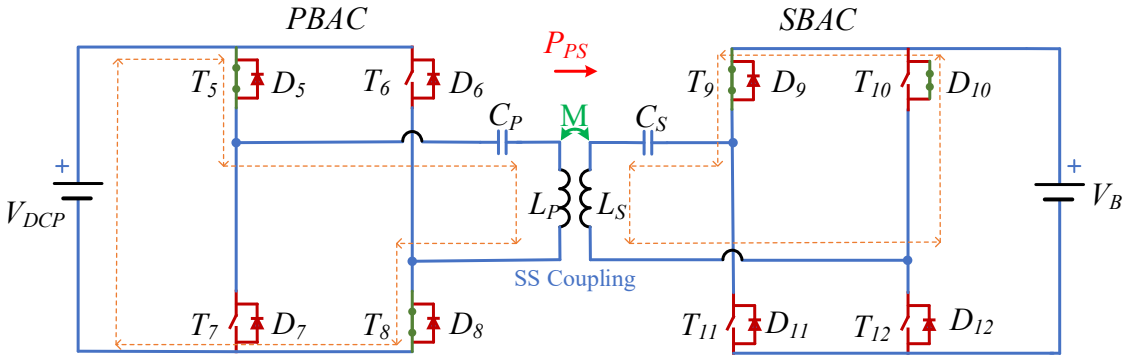
PBAC
SBAC
P_{PS}
T_5 D_5 T_6 D_6
C_P M C_S
T_9 D_9 T_{10} D_{10}
V_{DCP}
L_P L_S
V_B
SS Coupling
T_7 D_7 T_8 D_8
T_{11} D_{11} T_{12} D_{12}

(c)

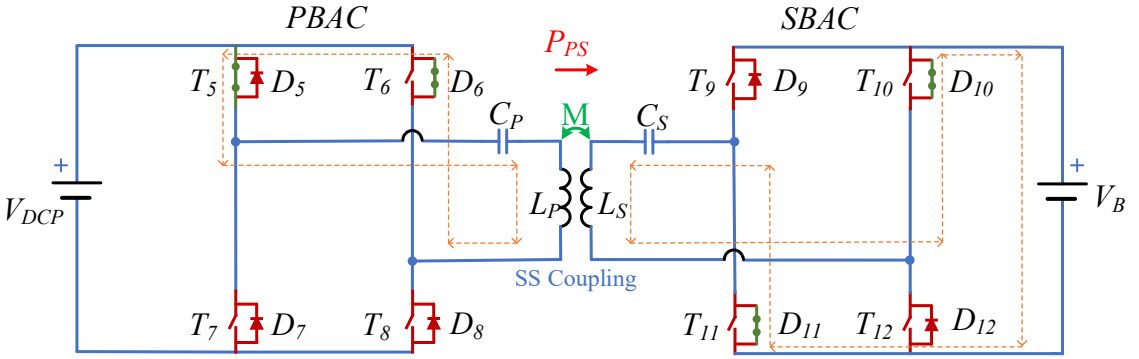
PBAC
SBAC
P_{PS}
T_5 D_5 T_6 D_6
C_P M C_S
T_9 D_9 T_{10} D_{10}
V_{DCP}
L_P L_S
V_B
SS Coupling
T_7 D_7 T_8 D_8
T_{11} D_{11} T_{12} D_{12}

(d)

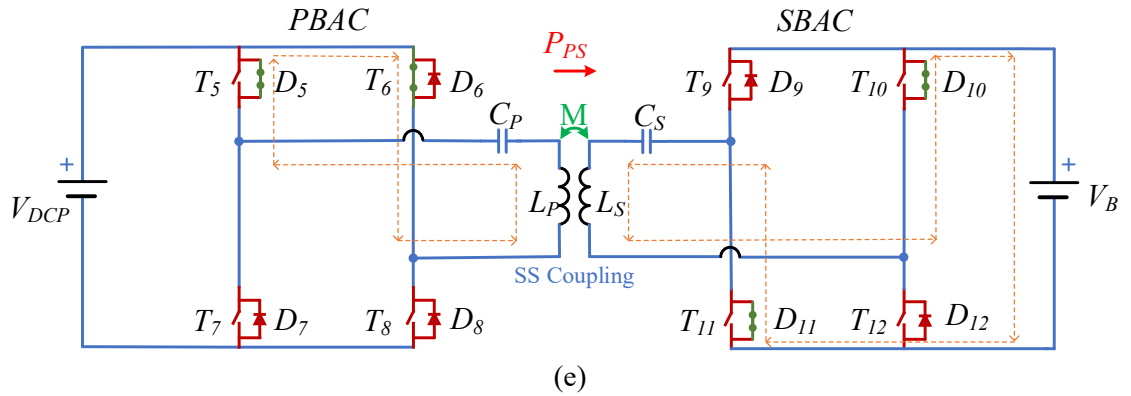

(e)

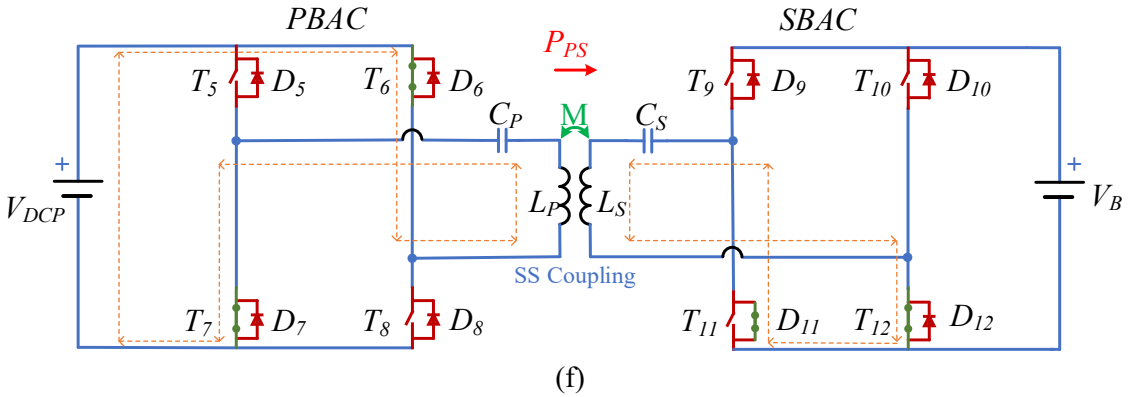

(f)

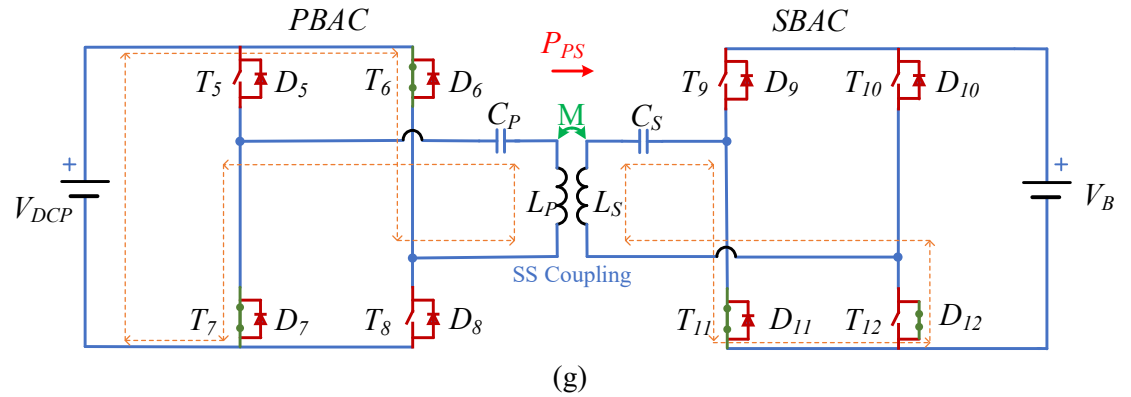

(g)

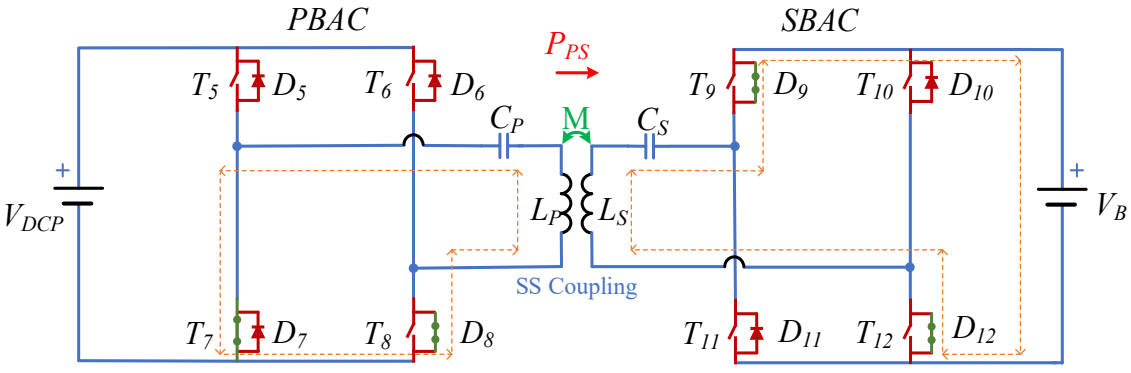

(h)

Fig. 5.3 Operation of DC-to-DC BWV2H system for V2H

5.3 Analysis

Denoting with I_S and I_P the First Harmonic Components (FHC) of the coil's currents, by the Faraday law of electromagnetic induction [14], the FHC voltages V_P and V_S induced across the coils are:

$$V_P = j\omega M I_S \tag{5.1}$$

$$V_S = -j\omega M I_P \tag{5.2}$$

where ω is angular switching frequency, by mesh analysis of circuit of Fig. 5.1, they can be expressed as below:

$$V_{PBAC} = Z_P I_P + V_P \tag{5.3}$$

$$V_{SBAC} = -Z_S I_S + V_S \tag{5.4}$$

Where, $Z_P$and $Z_S$are impedance, that includes primary and secondary inductor L_P and L_S, primary and secondary resonating capacitor C_P and C_S and primary and secondary parasitic resistance of coils R_P and R_S, respectively. Moreover, I_P , I_S and V_{PBAC} and V_{SBAC} are the fundamental component of the converter's current and voltage. V_P and V_S are the induce voltage of the primary and secondary coils, respectively.

According to Fig.5.1, secondary side complex power S_{SBAC} relation for BWV2H system is expresses in (5.5). Where P_{SBAC}, Q_{SBAC} represent the active and reactive power flow in secondary of S-S coil, due to switching effect of PBAC and SBAC convertor.

$$S_{SBAC} = P_{SBAC} + jQ_{SBAC} \tag{5.5}$$

Table 5.1: Eight mode of the BWV2H between primary and secondary converters.

	+ P_{SBAC} axis	1st quadrant	+ Q_{SBAC} axis	2nd quadrant	- P_{SBAC} axis	3rd quadrant	- Q_{SBAC} axis	4th quadrant
P_{SBAC}	> 0	> 0	0	< 0	< 0	< 0	0	> 0
Q_{SBAC}	0	> 0	> 0	> 0	0	< 0	< 0	< 0

The power level and power flow were first configure via active power (P_{SBAC}). But as mentioned in the Table 5.1, comprehensive and advanced control approaches involve the adjustment of both active and reactive power. As shown in Table 5.1, we may discuss control operation in a four-quadrant scheme when considering both forms of power. EV battery draining is connected with Quadrant-I and Quadrant-IV operations. EV battery charging occurs

in Quadrant-II and III. The quadrant is connected to reactive power flow. Reactive power is positive in Quadrant I and Quadrant II, and thus, it behaves as an inductive load. The charger produces reactive power as a capacitive load in Quadrant III and IV. With varied P_{SBAC} and Q_{SBAC} values, advanced algorithms will operate in quadrant regions. Nevertheless, early techniques that do not address the adjustment of a reactive power to a reference power differing from null only move axis of Table 5.1. So EV can regulate power in eight different states in the BWV2H system. That can be investigated for active power and reactive power absorb and deliver in BWV2H system at different state, obtained by regulating external phase shift angle Φ of PBAC and SBAC converter that can vary in all quadrant and axis as:

Sate 1 charges the battery with no power factor. G2V.

Sate 2. V2G power transfers deplete the battery with zero power factor.

Sate 3. The controller makes the power converter and battery use positive reactive power and zero active power. The secondary side has a pure inductive load.

Sate 4. The secondary load (power converter and battery) is capacitive with zero active power and negative reactive power.

Sate 5. The controller may configure. any first quadrant point to have positive active and reactive power. The power converter and supplementary batteries form a general inductive load.

Sate 6. V2G means the battery sends active power to the grid. The secondary power converter-battery set also uses positive reactive power.

Sate 7. like Sate 6, active power flows from the battery to the grid, but the secondary load provides reactive power, acting as a generic capacitor.

Sate 8. In this mode, the power converter and backup battery use active power and create reactive power.

Control logic in different quadrant can be easily determine by knowing active power and reactive power flow in it. The expiration for primary and secondary active and reactive power are determine by equation (5.1), (5.2), (5.3), and (5.4) are as follow:

$$P_{PBAC} = \frac{Z_S \, {V_{PBAC}}^2 - \omega M V_{PBAC} V_{SBAC} \, sin(\Phi)}{2(Z_P Z_S + \omega^2 M^2)} \tag{5.6}$$

$$Q_{PBAC} = \frac{-\omega M V_{PBAC} V_{SBAC} \, cos(\Phi)}{2(Z_P Z_S + \omega^2 M^2)} \tag{5.7}$$

$$P_{SBAC} = \frac{-Z_P\, {V_{SBAC}}^2 - \omega M V_{PBAC} V_{SBAC}\, sin(\Phi)}{2(Z_P Z_S + \omega^2 M^2)} \tag{5.8}$$

$$Q_{SBAC} = \frac{\omega M V_{PBAC} V_{SBAC}\, cos(\Phi)}{2(Z_P Z_S + \omega^2 M^2)} \tag{5.9}$$

From the above equation and Table 5.1, it is clear that EV charger can consume and deliver both active and reactive power and that from the point of view of the grid it can be treated as inductive, capacitive and resistive load. The values of power consumed and delivered depend on operation of the converters. The work in [11] deals with charger converters based on Table 5.1. The values of the active and reactive transferred power depend on Φ , α and β. For example, consider Fig. 5.4, where the input voltage and current waveforms of SBAC converter are reported for different value of Φ. With Φ = -90°, the SBAC operates with the active power as voltage V and current I are in phase and reactive power are almost zero as shown in Fig. 5.4(a). When Φ approaches 0°, current I leads the voltage V as in Fig. 5.4(b), and the SBAC can be treated as capacitor. Finally, when Φ approaches -180°, the current I lags the voltage V as in Fig. 5.4(c), and the SBAC can be treated as an inductor. These are three possible conditions of BWV2H functioning, useful for the analysis of active and reactive power flow and in both the direction.

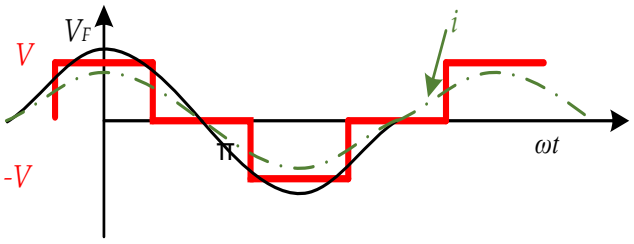

(a)

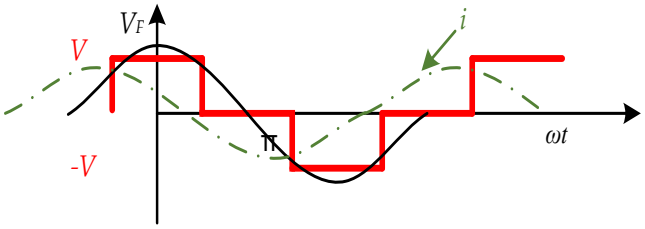

(b)

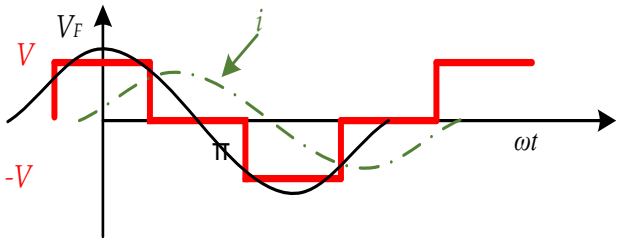

(c)

Fig. 5.4 Secondary coil square wave voltage (red solid), voltage fundamental sinusoidal (black solid) current (green dash)

Apart from loss, reactive power is also an important factor that affects the efficiency of the system, the effect of reactive power in the secondary of BWV2H already explain in last paragraph with the help of Fig. 5.4. The EPS angle determine by equation (5.8) and (5.9) with assumption $Z_P << \omega M$.

$$\Phi = \tan^{-1}\frac{-P_{SBAC}}{Q_{SBAC}} \tag{5.10}$$

From the above relation, the EPS angle Φ is dependent on both active and reactive power of secondary. The dominancy of the reactive element depends on Φ. Indeed, it is the deciding factor to quadrature operation as we are dealing with the bidirectional power flow.

Further, as per the consideration in earlier section IPS angle $\alpha = \beta$ on the basis of DPS control. We know that $V_{PBAC} = \frac{4V_{DCP}}{\pi} sin\left(\frac{\alpha}{2}\right)$ and $V_{SBAC} = \frac{4V_B}{\pi} sin\left(\frac{\beta}{2}\right)$ using this relation in equation (5.9) with assumption $Z_P << \omega M$ the IPS angle to control the amount of power deliver and absorb by BWV2H is represented in (5.11)

$$\alpha = \beta = 2\sin^{-1}\sqrt{\frac{-\pi^2 P_{SBAC}(Z_P Z_S + \omega^2 M^2)}{8\omega M V_{DCP} V_B \, sin(\Phi)}} \tag{5.11}$$

By the using the equation (5.10) and (5.11), we are able to generate the driving signal for both PBAC and SBAC converter to operate the BWV2H charge in all the possible direction. In general, only active power operation is takes place to control the power flow as mention in Fig. 5.4(a). While using this control method, we are able to control active and reactive power in respective quadrant system is possible, as shown in Fig. 5.4(b) and 5.4(c). As freedom to control active and reactive power with this method, but its cause lower efficiency of BWV2H system.

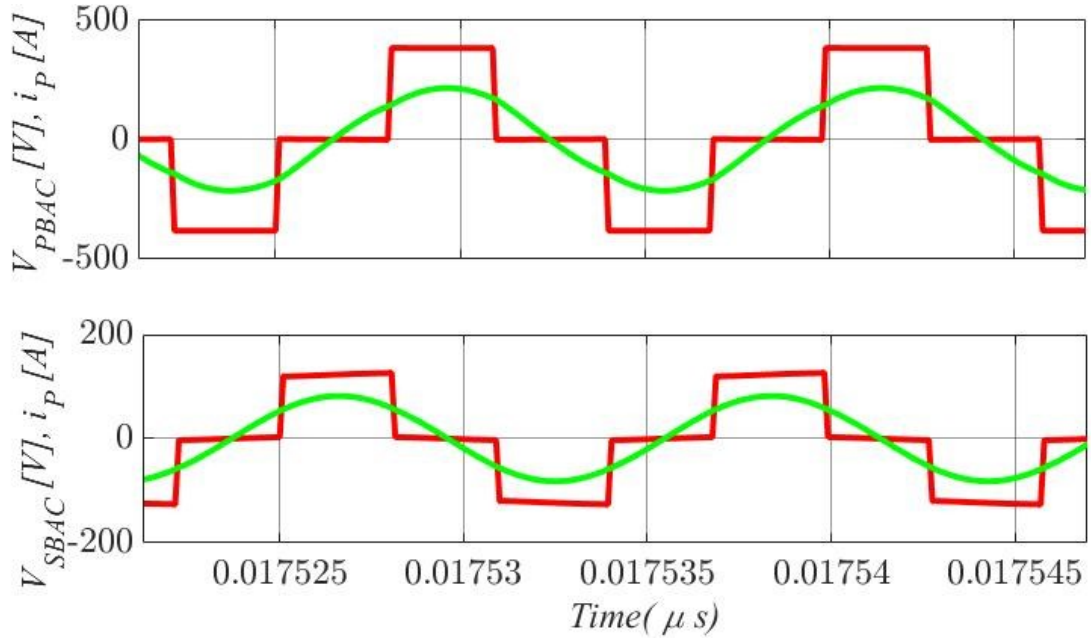
500
0
-500
V_{PBAC} [V], i_P [A]
200
0
-200
V_{SBAC} [V], i_P [A]
0.017525
0.01753
0.017535
0.01754
0.017545
Time(μ s)

(a)

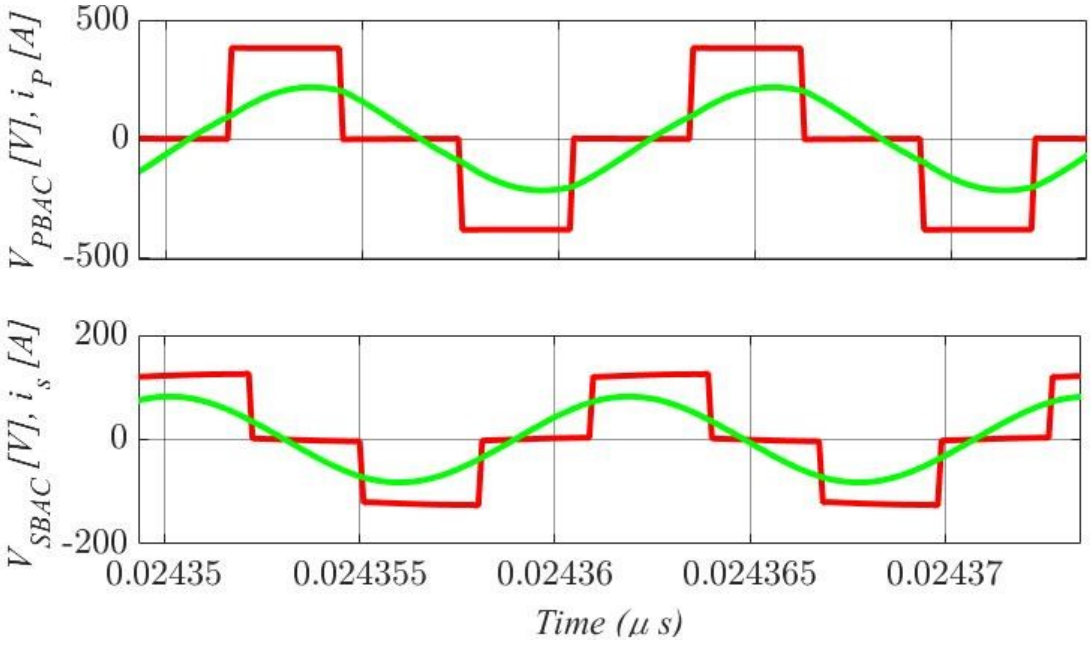
500
0
-500
V_{PBAC} [V], i_P [A]
200
0
-200
V_{SBAC} [V], i_s [A]
0.02435
0.024355
0.02436
0.024365
0.02437
Time (μ s)

(b)

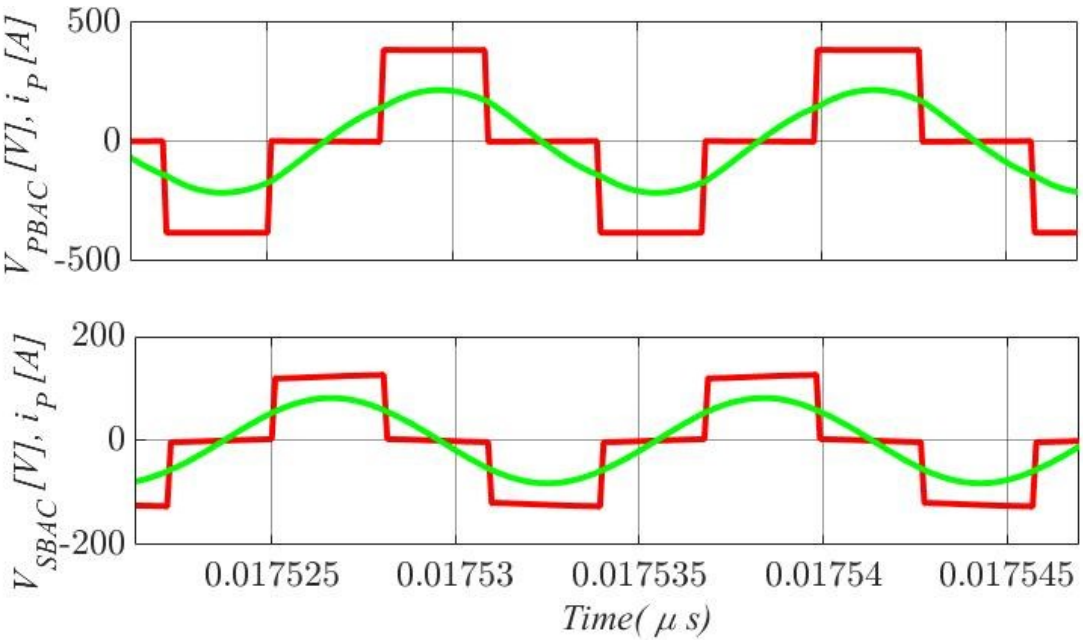

(c)

Fig.5.5 Primary and secondary coil voltage (red) current (green), primary current multiple of 20 and secondary current multiple of 3 at (a) $\Phi = -0.5\ \pi$ (b) $\Phi = -0.4\ \pi$ (c) $\Phi = -0.7\ \pi$

5.4 Discussion and Result

Fig. 5.5. depicts the steady state MATLAB/simulation waveforms of primary and secondary current and voltage side of S-S coil. The simulation result was taken place by utilized simulation parameters from Table 4.4 in chapter 4. Comparing Fig.5.5 (a), 5.5(b) and 5.5(c) of secondary side with Fig. 5.4(a), 5.4(b), 5.4(c) control approach of active and reactive power and following the same pattern as given in Fig. 5.4. We can see in Fig. 5.5(a), 5.5(b) and 5.5(c), the primary inverter and secondary control rectifier control with internal phase shift angle $\alpha = \beta = \pi$ and external phase shift angle Φ was chosen for three different states of control for $-0.5\ \pi, -0.4\ \pi, -0.7\ \pi$. The effect of change in external phase shift angle was visible in these wave form. As, $\Phi = -0.5\ \pi$ the behaviour of the BWV2H is resistive, so it operates at unity power factor, as a result voltage and current are in the phase. It causes only active power flow in BWV2H operation and negligible amount of reactive power is available. However, for $\Phi = -0.4\ \pi$ the behaviour of the BWV2H secondary and primary sides are inductive and capacitive, indeed, it operates at lagging and leading power factor i.e., current leads voltage in secondary and current lag voltage in primary, respectively. Due to this circulating current behaviour reactive power are available in this interval of control Moreover, for $\Phi = -0.7\ \pi$ the behaviour of the BWV2H secondary and primary sides are capacitive and inductive, indeed, it operates at leading and lagging and power factor i.e., current lag voltage in secondary and current leads voltage in primary, respectively. Due to this circulating current behaviour reactive power are available in this interval of control.

As we are aware that, in BWV2H system we utilise the active power to make the system more efficient, we are neglecting reactive power operation in BWV2H system. It was well

undusted from above control analysis and simulation result shown in Fig. 5.5 that, reactive power in BWV2H system is depended on Φ value. Indeed, secondary active and reactive power at different value of Φ are shown in Table 5.2, and it also realized that when reactive power is in action, it cause the VA rating of BWV2H system will be higher and its effect the efficiency of system.

Table 5.2. Active and reactive power at different Φ value

	$\Phi = -0.5\,\pi$	$\Phi = -0.4\,\pi$	$\Phi = -0.7\,\pi$
P_{SBAC}	1570 W	1500 W	1310 W
Q_{SBAC}	-15 VAR	-490 VAR	893 VAR

Fig. 5.6. depicts the efficiency plot of BWV2H system w.r.t input power flow from primary to secondary. For drawing this efficiency plot by MATLAB, we are considering losses of the system such as S-S coil loss, switching loss, conduction loss, effect of reactive power and many more. However, for comparative study, for the effect of reactive power on the efficiency of BWV2H system was plotted at $\Phi = -0.5\,\pi, -0.4\,\pi, -0.7\,\pi$ in blue, red, and black dotted, respectively in Fig. 5.6. Maximum efficiency 84.9%,84%, and 82% were achieved at power 500W, from there efficiency of the system are slightly reduce as in put power of the system are increase. The maximum loss take place in the secondary side, as it has more than double current w.r.t to primary side, and having large hard switching loss too. We are not repeating the reversal mode operation as they are the mirror image and having almost similar loss. Still in secondary side have higher loss as the voltage in secondary is low as per the battery voltage label, there for it have higher current w.r.t primary side.

As per the current study, we see that the efficiency of the system is reduce when we are changing Φ from its optimal value, this is the major draw back of the system to control the power flow with this method. But it will become reward for BWV2H, when we utilise this control method with minimum reactive power flow, to almost eliminate the hard switching of PBAC and SBAC converter. It can help to improve the efficiency of BWV2H system by 1% - 2% approximate.

5.5 Conclusion

This chapter includes BWV2H operation based on J2954. We explain and examine operation of active and reactive power flow with quadrature operation. Further, we analyse the control approach of BWV2H by DPS control method with different EPS angle, to understand the effect of reactive power. Indeed, when $\Phi = -0.5\,\pi, -0.4\,\pi, -0.7\,\pi$, maximum efficiency 84.9%,84%, and 82% was achieved with a transferred power of 500W. This can be considered as a drawback, but it could result in an advantage if a small amount of reactive power is transferred to eliminate the hard switching. This condition could enhance the efficiency approximately of 1% - 2%. To eliminate the hard switching control method was not analysis till now. As future work, we would like to investigate this control with zero voltage switching.

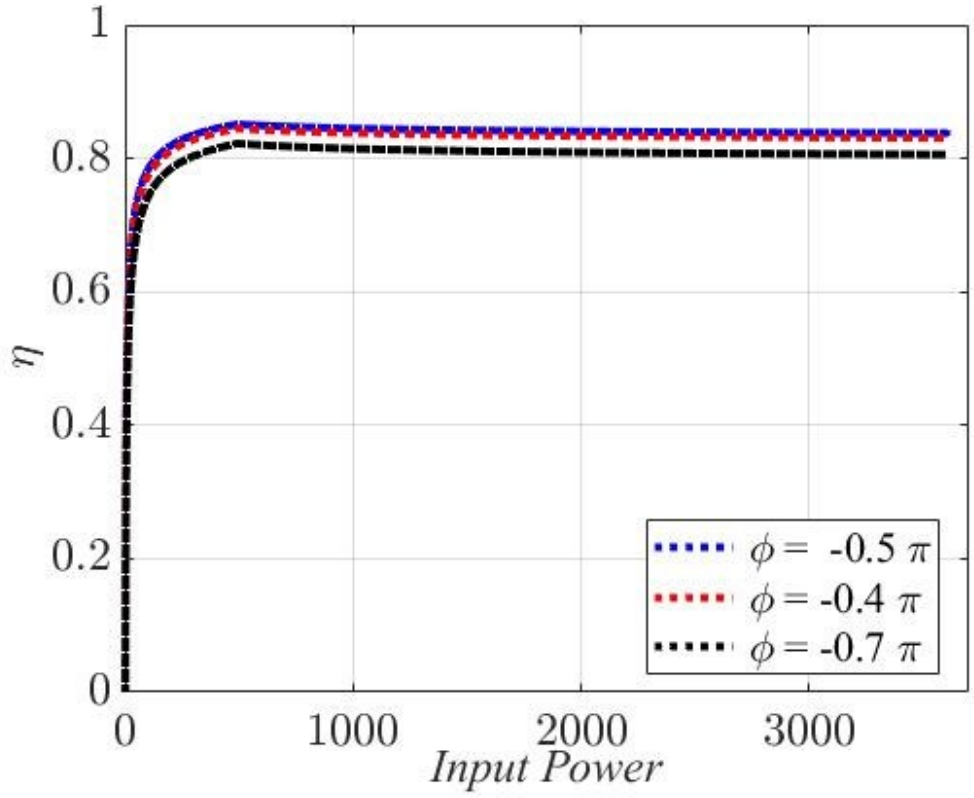

Fig. 5.6 BWV2H Topology of primary and secondary H-bridge converters

5.6 References

1. Monteiro V, Afonso JA, Ferreira JC, Afonso JL. "Vehicle Electrification: New Challenges and Opportunities for Smart Grids," Energies, 2019, 12, 1 , pp. 118

2. Sagar, A., Kumar, A., Bertoluzzo, M., Jha, R.K. "Analysis and Design of a Two-winding Wireless Power Transfer System with Higher System Efficiency and Maximum Load Power," IECON 2022—48th Annual Conference of the IEEE Industrial Electronics Society, 2022; pp. 1–6

3. S. Li and C. C. Mi. "Wireless Power Transfer for Electric Vehicle Applications," In IEEE Trans. Emerg. Sel., 2015, 3, 1, pp. 4-17

4. J2954: Wireless Power Transfer for Light-Duty Plug-In/Electric Vehicles and Alignment Methodology; SAE International: Warrendale, PA, USA, 2020

5. Kumar, A., Neogi, N. "Bidirectional Converter and Energy Storage System," International Journal of Enhanced Research in Science Technology & Engineering, 2015, 4, 6, pp. 15-23

6. G. Pandey and N. R. T. "Power Flow Study of Grid Connected Bidirectional WPT Systems for EV Application," In IEEE International Conference on Power Electronics,

Smart Grid and Renewable Energy, 2020, pp. 1-6

7. Bertoluzzo, M., Giacomuzzi, S., Kumar, A., “Design of a Bidirectional Wireless Power Transfer System for Vehicle-to-Home Applications,” Vehicles, 2021, 3, 3, pp. 406-425

8. Villante C, Ranieri S, Duronio F, De Vita A, Anatone M. “An Energy-Based Assessment of Expected Benefits for V2H Charging Systems through a Dedicated Dynamic Simulation and Optimization Tool,” World Electric Vehicle Journal, 2022, 13, 6, pp. 99

9. Kumar, A., Bertoluzzo M., Sagar, A., “Different loading of Bi-directional wireless power transfer for VaH at good efficiency,” In: International Conference on Advanced Computing and Ingenious Technologies in Engineering Science Proceeding on AIP, Greater Noida, 2021 (accepted)

10. A. Berger, M. Agostinelli, S. Vesti, J. A. Oliver, J. A. Cobos and M. Huemer. “A Wireless Charging System Applying Phase-Shift and Amplitude Control to Maximize Efficiency and Extractable Power,” In IEEE Trans. Power Electron, 2.15, 30, 11, pp. 6338-6348

11. Triviño A, Gonzalez-Gonzalez JM, Castilla M. “Review on Control Techniques for EV Bidirectional Wireless Chargers,” Electronics, 2021,10 ,16, pp.1905

12. Y. Hsieh, Z. Lin, M. Chen, H. Hsieh, Y. Liu and H. Chiu. “High Efficiency Wireless Power Transfer System for Electric Vehicle Applications,” IEEE Trans. Circuits Syst. II: Express Br., 2017, 64, 8, pp. 942-946

13. J. M. González-González, A. Triviño-Cabrera and J. A. Aguado. “Assessment of the Power Losses in a SAE J2954-Compliant Wireless Charger,” in IEEE Access, 2022, 10, pp. 54474-54483

Chapter 6

A bidirectional wireless power transfer system's control architecture with V2H compatibility

6.1 Introduction

CHANGES in electric vehicle charging method will have an effect on the electrical grid in the near future. According to the "vehicle-to-grid" concept, electric vehicle battery chargers can send and receive power in both directions [1,2]. They will provide valuable services to the distribution grid or to the home grid of the person who owns the vehicle. Wireless power transfer battery chargers make it possible for people who aren't good with technology to use electric vehicles in a way that is safer and easier to use [3,4]. The next step in all of these ideas is the development of wireless chargers that can send power from a vehicle to the grid [5]. Before come to know that what we are dealing in this chapter? Two different arrangement power sizing of the BWV2H [6,7] i.e., secondary with passive rectifier together with the DC-DC chopper, and secondary only with active rectifier are explain in Chapter 3. However, in this chapter we discuss the control algorithms for BWV2H system only with the primary and secondary active H-bridge converter for battery charger [8]. It focuses on the power conversion stages that are needed for a charging work and grid synchronization at home [9,10,11,12,13]. The algorithms are built one by one in the continuous time domain using techniques based on the analysis of Bode diagrams of the transfer functions involved in the operation of the system. Using simulations made in the Matlab/Simulink environment, each algorithm's performance has been checked on its own.

6.2 Circuital scheme of the BWV2H

Fig. 6.1 shows the circuital scheme of BWV2H. In the scheme and through the full chapter, uppercase letters indicate constant quantities or quantities that vary slowly with respect to the grid frequency, peak amplitudes of alternating quantities, or average values of continuous quantities. Lowercase letters indicate alternating or variable quantities at or above grid frequency.

The BWV2H is interfaced to the domestic grid by means of the front-end converter (FEC) equipped with an inductive input filter L_G.[14] The FEC absorbs the current i_G from the domestic grid. The phase of i_G with respect to grid voltage v_G is adjusted in order to define the direction of the active power flow and the amount of the reactive power exchanged with the grid [15], if any. At the output of the FEC the capacitor C_{DCP} sustains the dc bus of the primary section. The continuous voltage V_{DCP}, which can be considered nearly constant, is applied to the input of the high-frequency primary converter (HFPC).

The HFPC generates the quasi-square wave voltage v_{HFPC} at the nominal supply frequency of 85 kHz [16], and controls the first harmonic amplitude V_{HFPC} of this voltage by adjusting the phase delay between the gate commands of its two legs, according to the phase shift control technique [17]. The HFPC supplies the primary coil and its compensation network, consisting of the capacitor C_P connected in series to the coil and resonating with the coil's self-inductance [18,19].

Thanks to resonance, the current i_P flowing in the coil is practically sinusoidal. It generates

a variable magnetic induction flux that links the secondary coil and induces an alternating voltage across its terminals. The induced voltage is the mean by which the power P_{PS} is transferred from the primary to the secondary section of the BWV2H. The series resonant capacitor C_S compensates for the voltage drop across the secondary coil's self-inductance L_S originated by the flow of the current i_S. Consequently, the first harmonic of the voltage v_{HFSC} applied across the input of the HFSC is ideally equal to the induced voltage [18]. During the charging operation, the switches T_9-T_{12} of HFSC are driven, and the current i_S flows through the switches T_9-T_{12}. The alternating component of the rectified current I_{DCS} flows in the capacitor C_{DCS} while its average component I_B, that suitable to charges the battery. The capacitor C_{DCS} is sized so that the dc bus voltage V_{DCS} of the secondary section of the BWV2H can be considered constant. Following from this condition, and in the hypothesis that i_S flows for the whole supply period forcing the alternative conduction of the pairs of switches T_9-T_{12} and T_{10}-T_{11}, it derives that v_{HFSC} actually have a square waveform.

In order to reverse the direction of the power flow, i.e. to transfer the power P_{SP} from the EV battery to the grid, it is sufficient to adjust the current references provided to the control loops of FEC and to mutually exchange the control strategies of HFPC and HFSC. Indeed, in this condition the HFPC behaves as a high frequency active rectifier whilst the HFSC operates as a high frequency inverter.

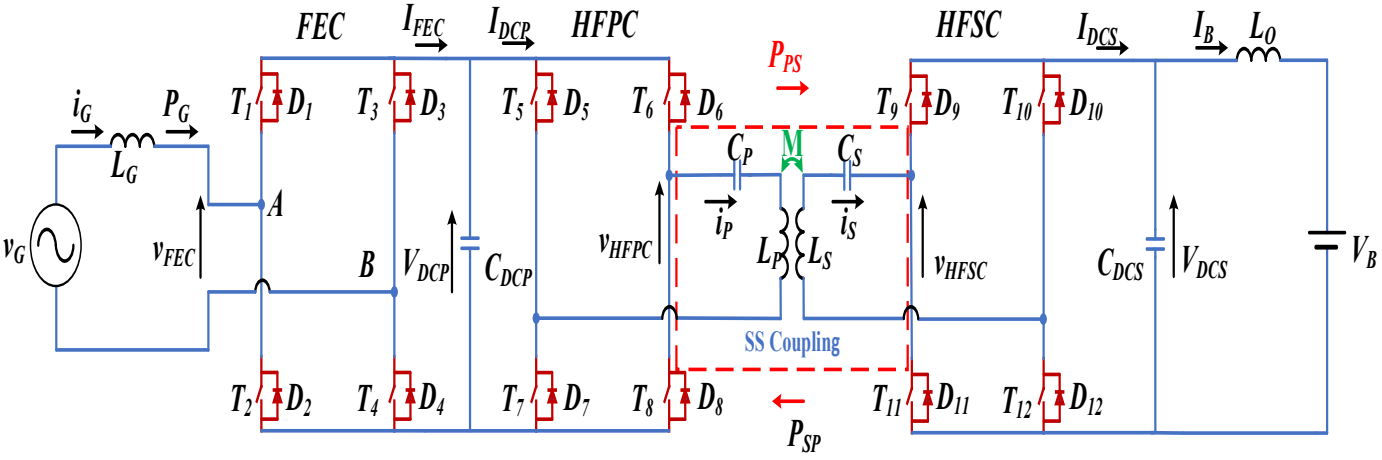

Fig. 6.1 Circuital scheme of the BWV2H

6.3. Generalized control approach

As a general approach, the controllers of the algorithms of the internal and external levels are based on the PI topology and are designed by imposing the phase margin M_ϕ and the passband angular frequency ω_{PB} of the control loop.

The use of proportional integral (PI) controllers gets rid of this limitation. The TF between the error e(t) at the input of a PI controller and the manipulated quantity y(t) at its output is given by (6.1) in terms of the proportional gain K_P and the integral time constant τ_I.

$$C(s) \triangleq \frac{Y(s)}{E(s)} = K_p\left(\frac{1+s\tau_I}{s\tau_I}\right). \qquad (6.1)$$

From the expression (6.1) it is found that the controller's time constant must satisfy the condition in terms of phase margin (M_ϕ) of the controller at the passband frequency $\boldsymbol{\omega_{BP}}$ is expressed as

$$atan(\omega_{PB}\tau_I) - \frac{\pi}{2} = -\angle Sys(j\omega_{PB}) - \pi + M_\phi, \tag{6.2}$$

where the left-hand terms give the phase at the passband angular frequency of the TF of the PI and $\boldsymbol{\angle Sys(j\omega_{PB})}$ is the phase of the system to be controlled. From (6.2), the time constant τ_I is worked out as

$$\tau_I = \frac{1}{\omega_{PB}} tan\left(-\frac{\pi}{2} - \angle Sys(j\omega_{PB}) + M_\phi\right). \tag{6.3}$$

The assumption, usually taken, that the passband of the closed-loop TF corresponds to the cut-off frequency of the open-loop TF, leads to the relation

$$K_P \left|\frac{1+j\omega_{PB}\tau_I}{j\omega_{PB}\tau_I}\right| |Sys(j\omega_{PB})| = 1, \tag{6.4}$$

where the operator $|\cdot|$ denotes the magnitude of its argument.

By substituting (6.3) into (6.4) it is possible to work out τ_I and K_P as functions of the system TF and of the required ω_{PB} and M_ϕ. Finally, the integral gain K_I of the controller is expressed as

$$K_I = \frac{K_P}{\tau_I}. \tag{6.5}$$

The controllers are designed in the continuous-time domain according to (6.3) and (6.4), but bearing in mind that they will be implemented in a discrete-time system with sampling period T. To this end, in designing the controller a block representing the sampling delay has been inserted in series to the system to be controlled. This block, which in the discrete-time domain is represented by the z^{-1} operator, in the continuous-time domain is modelled using

$$SD(s) = \frac{1 - s\frac{T}{2}}{1 + s\frac{T}{2}} \tag{6.6}$$

obtained by bilinear or inversion of the Tustin discretization method.

After computing K_P and K_I, the controller is discretized using the Tustin method obtaining (6.7), which links the present value of the controller's output to its value in the previous sampling instant and to the present and previous values of the error signal.

$$Y(k) = Y(k-1) + K_{e(k)}e(k) + K_{e(k-1)}e(k-1). \tag{6.7}$$

The gains $K_{e(k)}$ and $K_{e(k-1)}$ are given by the equations

$$K_{e(k)} = \left(K_I \frac{T}{2} + K_P\right), \tag{6.8}$$

$$K_{e(k-1)} = \left(K_I \frac{T}{2} - K_P\right). \tag{6.9}$$

6.4. Control algorithms design

6.4.1. Grid current control by FEC

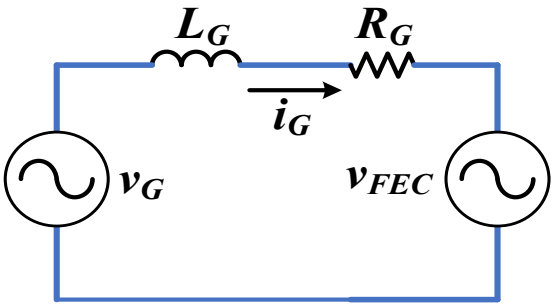

Fig. 6.2 Equivalent scheme of the system to be controlled.

The internal current loop (ICL) acquires the reference $i_{G,ref}$, generated by external voltage loop (EVL), computes the reference for the voltage v_{FEC} to be generated at FEC input, and finally generates the gate commands for the FEC converter as a function of $v_{FEC,ref}$ and of the measured dc voltage V_{DCP}.

The system to be controlled consists of the filter inductance L_G placed at the FEC input and its serially connected parasitic resistance R_G. The grid voltage v_G acts as an external disturbance. The scheme of the controlled system is shown in Fig. 6.2. Its TF is

$$G_{iG}(s) = \frac{1}{sL_G + R_G}, \tag{6.10}$$

and the block diagram of the relevant control loop is shown in Fig. 6.3

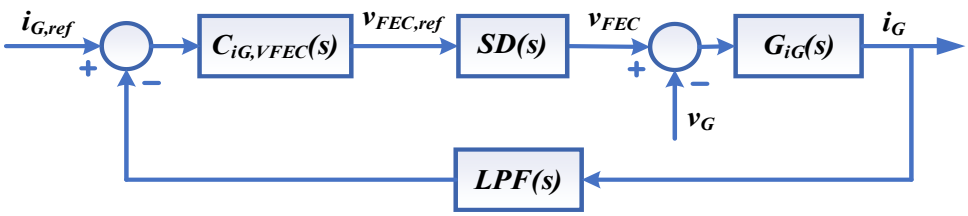

Fig. 6.3. Block diagram of the current control loop of i_G

The controller $C_{iG,VFEC}(s)$ processes the error on i_G and generates $v_{FEC,ref}$. Within one

sampling delay the voltage reference is converted into the command signals for the power switches of the FEC and v_{FEC} is generated at its input. A first order TF, given by (6.10) and

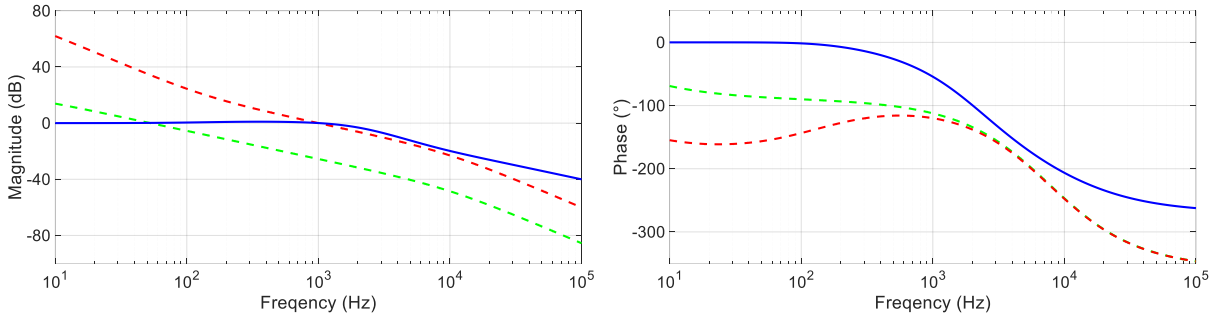

Fig. 6.4 Bode diagram relevant to internal current loop. Open-loop uncontrolled system (dashed green), open-loop controlled system (dashed red), closed-loop controlled system (solid blue).

having a cutoff frequency of 10 kHz, is inserted in the feedback path, to represent the LPF that attenuates the high-frequency components of the signal coming from the transducer of i_G.

$$LPF(s) = \frac{1}{s\tau_{LPF}+1}. \qquad (6.11)$$

The supply frequency of the coupled coils is standardized at 85 kHz [16]. However, the outputs of the control algorithms are updated once every four supply periods of the HFPC in order to allow the microcontroller enough processing time. Hence, the output of the discretized version of $C_{iG,VFEC}(s)$ is updated every 45 µs. For reasons related to the simplicity of the implementation of the control loops and to the reduction of the power losses, the switches of the FEC commutate with the same period, i.e., at 21.25 kHz. Given the sampling frequency above 20 kHz and the requirement of generating a sinusoidal current at 50 Hz, it is reasonable to set the passband ω_{PB} of the control loop to 1 kHz and the phase margin M_ϕ to 70°. This selection of M_ϕ gives a quick response, but causes an overshoot when a stepwise reference is applied. However, it must be remembered that $i_{G,ref}$ is sinusoidal, so this problem does not arise in the considered application.

The $C_{iG,VFEC}(s)$ controller is of the PI type and has been designed by applying the procedure reported in the section 6.3 to a system constituted by the cascade of $G_{iG}(s)$, SD(s), and LPF(s). Considering a BWV2H having the parameters reported in Table. 6.1 [1], the open-loop system without the controller has the Bode diagram plotted with the dashed green line in Fig.6.4.

The diagram of the open-loop controlled system is drawn with the dashed red line, while that of the closed-loop controlled system is shown by the solid blue line. The analysis of the diagrams confirms that $C_{iG,VFEC}(s)$ successes in imposing the required bandwidth and phase margin.

The step response for close loop i_G is plotted in Fig 6.5. As expected there is a small over elongation; Moreover, in the first moments after the step reference is applied, the system output decreases and becomes negative rather than increasing. Because of the inclusion of the delay block in the forward gain loop and the low pass filter in the feedback route, the control system does not behave like a conventional second-order system, which is normally used as a reference

in assessing the responses to canonical signals. As in the case of over elongation, this non-ideal behavior does not give cause for concern since the reference signal for this control loop will be sine.

Table 6.1. Specification of BWV2H

Parameters	Symbol	Value
Grid power	P_G	3300 W
Grid Peak Voltage	V_G	358 V
Grid Current	i_G	22.6 A
Battery Maximum voltage	$V_{B,M}$	130 V
Battery Minimum voltage	$V_{B,m}$	95 V
Battery current (charging)	$I_{B,C}$	30.48 A
Battery current (discharging)	$I_{B,D}$	50 A
Grid side inductance	L_G	3 mH
DC Primary Capacitor	C_{DCP}	1.21 mF
Primary & Secondary Inductance	$L_P = L_S$	220 µH
Primary & Secondary Capacitor	$C_P = C_S$	15.9 nF
DC Secondary Capacitor	C_{DCS}	3.51 µF
Battery side inductor	L_O	151 µH
Battery nominal charging current	$I_{B,C,N}$	30.48 A
Battery series resistance	$R_{B,ESR}$	0.1 Ω

From (6.4), and (6.5) the gain of continuous-time PI controller are

$$\mathrm{K_P} = 18.773 \tag{6.12}$$

$$\mathrm{K_I} \triangleq 15930 \tag{6.13}$$

Respectively the gain in the discrete domain from is obtain in (6.14), and (6.15). by putting the value of $\mathbf{K_P}$ and $\mathbf{K_I}$ (6.9) and (6.10) where $\boldsymbol{\tau = T}$

$$\mathrm{K_{e(k),}}_{i_G} = 19.1481090455518 \tag{6.14}$$

$$\mathrm{K_{e(k-1),}}_{i_G} = -18.3984509438856 \tag{6.15}$$

In order to limit the ripple of the current i_G, it was chosen to control the static FEC switches with the bipolar technique. The two duty cycles are calculated as

$$\delta_A = 0.5 + \frac{1}{2}\frac{v_{FEC,ref}}{V_{DCP}} \tag{6.16}$$

$$\delta_B = 0.5 - \frac{1}{2}\frac{v_{FEC,ref}}{V_{DCP}} \tag{6.17}$$

6.4.2. External close loop of V_{DCP} voltage through P_G

6.4.2.1. Generation of $P_{G,ref}$

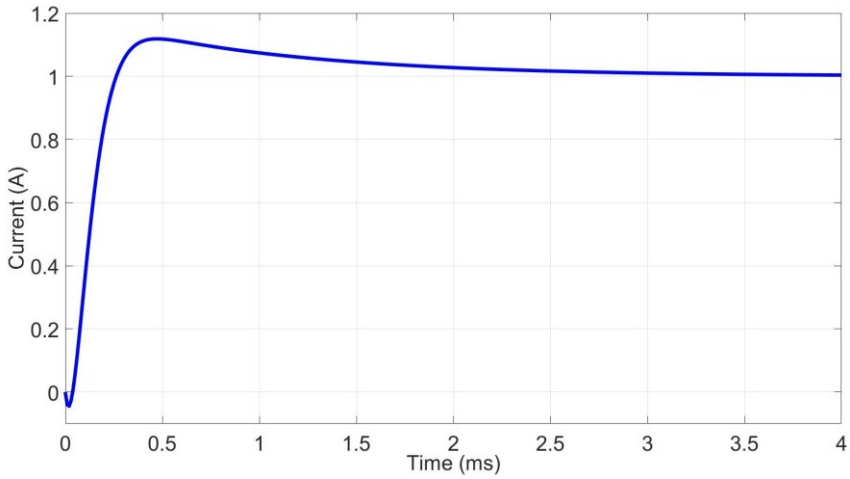

Fig 6.5 Response to the step of the current control loop of i_G

The FEC has the two tasks of controlling the average voltage V_{DCP} across the terminals of C_{DCP} to a value that allows the HFPC to operate correctly and of managing the power exchanged with the grid following the indications of CEI 0-21 [20], which requires adjusting the ratio of active to reactive power according to grid conditions. This latter issue is not considered in this chapter, however, EVL for V_{DCP} and ICL for i_G , which manipulates and controls the grid current, respectively, are designed to also provide for the management of reactive power. The two tasks of EVL for V_{DCP} are easily integrated if the algorithm is designed to manipulate directly the active and reactive power P_G and Q_G exchanged with the grid rather than the current i_G. The grid current reference $i_{G,ref}$ is then obtained by processing the active power reference $P_{G,ref}$ and, possibly, the reactive power reference $Q_{G,ref}$.

The EVL for V_{DCP} has an interaction of the first type with EVLC for V_{DC} during battery charging and another interaction of the first type with EVLD for V_{DCP} during battery discharging. During the charging process, EVLC for V_{DCP} tries to bring V_{DCP} to the lower reference value $V_{DCP,ref,low}$ by generating a reference for the power P_{PS} absorbed from C_{DCP} and transferred to the secondary side of BWV2H. At the same time, EVLD for V_{DCP} tries to bring V_{DCP} to the higher reference value $V_{DCP,ref,high}$ by generating the reference for the grid power P_G injected in C_{DCP}. Instead, while discharging the battery, EVLD for V_{DCP} tries to bring V_{DCP} to the higher reference value $V_{DCP,ref,high}$ by generating the reference for the power P_{SP} drawn from the battery and injected in C_{DCP}. At the same time, EVL for V_{DCP} tries to bring V_{DCP} to the lower reference value $V_{DCP,ref,low}$ by generating the reference for the power P_G drawn from C_{DCP} and injected in the grid.

The assumption that the power P_{SP} is transferred from the battery and injected into C_{DCP} entails that the losses in the power converters and in the coupled coils have been neglected. The same approach is also applied in manipulating the power references to obtain the current references. This approximation does not affect the functioning of the system since it is automatically compensated by the feedback control loops implemented in all the algorithms.

Given that EVL for V_{DCP} generates a reference for P_G, it results convenient to model the controlled system by highlighting this quantity. The first step is to express the relationship

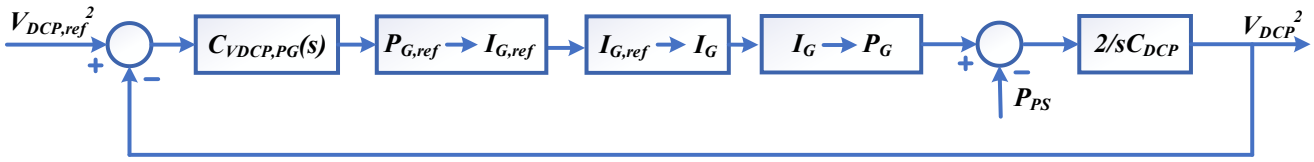

Fig. 6.6 Ideal block diagram of control loop of V_{DCP}.

between the voltage across a capacitor and its stored energy in terms of Laplace transforms. By considering that the energy stored in the capacitor corresponds to the integral of the injected power, this relationship is given by

$$\frac{P(s)}{s} = \frac{1}{2} C V^2(s), \tag{6.18}$$

where $V^2(s)$ is the L-transform of the capacitor squared voltage. From (6.18) it derives that the state variable used in modelling the system is V_{DCP}^2 instead of V_{DCP} and that it is convenient to control the square of C_{DCP} voltage rather than the voltage itself.

The ideal scheme of the voltage control loop is represented in Fig. 6.6. Like in the previous cases, the controller $C_{VDCP,PG}(s)$ is of the PI type. The integral action would not be strictly necessary if the purpose of the controller was only to charge an insulated capacitor at the desired voltage. In this case, however, the capacitor supplies the HFPC (or the FEC, during battery discharging). Consequently, $C_{VDCP,PG}(s)$ must require the injection of power into C_{DCP} even when the voltage error is null to compensate for the power P_{PS} absorbed by the HFPC.

The block denoted as $P_{G,ref} \rightarrow I_{G,ref}$ represents the conversion between the active power reference generated by the controller and the reference $I_{G,ref}$ for the amplitude of the grid current. It is approximated by the relation

$$I_{G,ref} = \frac{2P_{G,ref}}{V_{G,N}}, \tag{6.19}$$

obtained by assuming that the grid voltage is sinusoidal and with the nominal amplitude $V_{G,N}$, that the grid current is in phase with the voltage, and that the efficiency of the FEC is equal to one. The reference $I_{G,ref}$ will be further manipulated to work out the grid current reference $i_{G,ref}$ to be provided to ICL for i_G , described in Subsection 6.4.1.

The block denoted as $I_{G,ref} \rightarrow I_G$ models the non-idealities introduced by the control algorithm ICL for i_G in modulating the amplitude of i_G. Considering that the amplitude Bode diagram of the control loop of i_G, shown in Fig. 6.4, is flat up to 1 kHz, and that, as it will be shown in the following paragraphs, the bandwidth of the loop controlled by $C_{VDCP,PG}(s)$ is much smaller, these effects can be disregarded and the block $I_{G,ref} \rightarrow I_G$ can be considered as an unitary gain. The block $I_G \rightarrow P_G$ represents the conversion between the actual amplitude of the grid current and the power entering into to the dc bus of the FEC. By disregarding the FEC losses,

it is approximated by reversing (6.19). The power P_{PS} constitutes a disturbance for the system. It is subtracted from P_G to obtain the net power injected in the capacitor. The last block in the forward path of Fig. 6.6 derives from (6.18) and represents the capacitor C_{DCP}.

In implementing the control system, it must be remembered that the transduced quantity is V_{DCP} instead of V_{DCP}^2 and that C_{DCP} is actually charged by a current. Consequently, the block

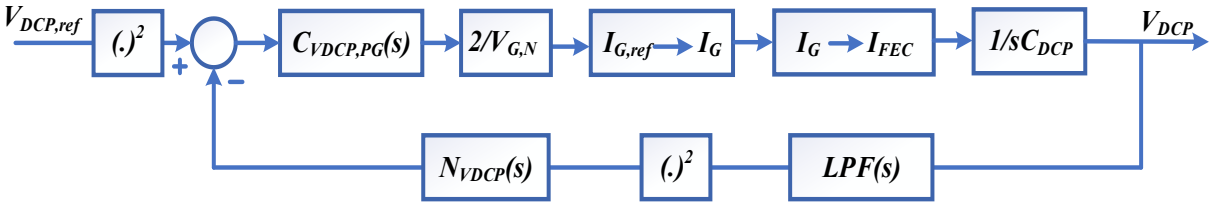

Fig. 6.7 Ideal block diagram of control loop of V_{DCP}.

diagram of Fig. 6.7 gives a more realistic representation of the physical structure of the control loop of V_{DCP}. In the figure, the block $P_{G,ref} \rightarrow I_{G,ref}$ has been substituted for by the gain coming from (6.19) whilst the block $I_G \rightarrow I_{FEC}$ represents the relation between the grid current and the currents that actually enters into the dc bus of the FEC. In order to simplify the diagram, the disturbance current I_{DCP}, which accounts for the power P_{PS}, is not shown. The blocks $(\cdot)^2$ represent the square operator and are implemented by the microprocessor while processing the samples of $V_{DCP,ref}$ and of the voltage acquired at the output of the LPF.

The capacitor C_{DCP} has the function of absorbing the oscillating components of the power exchanged with the grid in order to charge or discharge the battery with a constant power. For this reason, at steady state, V_{DCP} oscillates at twice the grid frequency around its reference value and can be approximated as

$$V_{DCP}(t) \approx V_{DCP,ref} + \Delta v_{DCP} sin(2\omega_G t). \tag{6.20}$$

The quantity processed by the controller $C_{VDCP,PG}(s)$ is V_{DCP}^2 that, following from (6.20), is approximated with the expression

$$V_{DCP}{}^2(t) \approx V_{DCP,ref}{}^2 + \frac{\Delta v_{DCP}{}^2}{2} + 2V_{DCP,ref}\Delta v_{DCP} sin(2\omega_G t) - \frac{\Delta v_{DCP}{}^2 cos(4\omega_G t)}{2}, \tag{6.21}$$

obtained using the half-angle formulas. In (6.20) a term with angular frequency $4\omega_G$, corresponding to 200 Hz, appears.

The controller $C_{VDCP,PG}(s)$ should not attempt to eliminate the oscillations of V_{DCP}^2, otherwise a distortion in the waveform of i_G would be introduced. Hence, either the components at frequencies of 100 Hz and 200 Hz are left outside the bandwidth of the V_{DCP} control loop, or they are attenuated before being processed by the controller. In designing the control loop, an intermediate solution has been selected: the bandwidth ω_B has been set to $2\pi \cdot 20$ rad/s and the

phase margin to 80°, and a notch filter, denoted as $N_{VDCP}(s)$ in Fig. 6.7, has been inserted in the feedback path of the loop. The notch filter has the TF

$$N_{VDCP}(s) = \frac{s^2+\omega_0^2}{s^2+s\omega_B+\omega_0^2}, \tag{6.22}$$

with a bandwidth $\omega_B=2\pi\cdot40$ rad/s and a center frequency $\omega_0=2\pi\cdot100$ rad/s. Being inserted

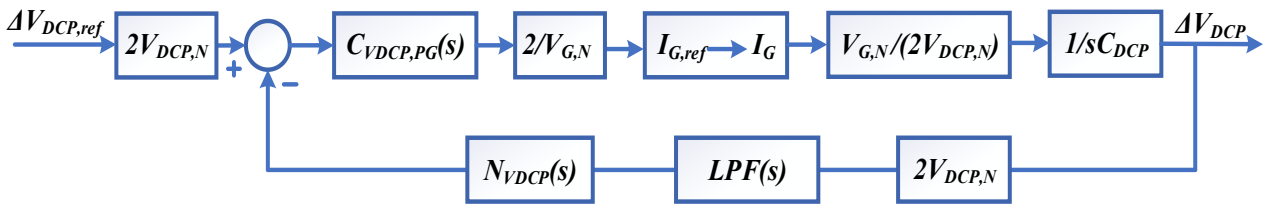

Fig. 6.8 Ideal block diagram of control loop of V_{DCP}.

after the square operator $(\cdot)^2$, the notch filter operates both on the 100 Hz and the 200 Hz components of V_{DCP}^2.

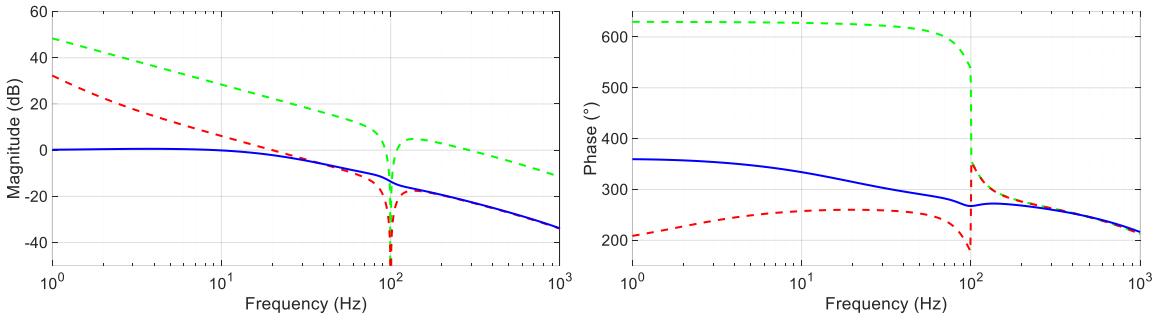

Fig. 6.9. Bode diagrams relevant to EVL for V_{DCP}. Open-loop uncontrolled system (dashed green), open-loop controlled system (dashed red), closed-loop controlled system (solid blue).

The presence of the operator $(\cdot)^2$ makes the diagram of Fig. 6.7 not linear and, consequently, the controller $C_{VDCP,PG}(s)$ cannot be designed using the conventional approach. The diagram is then linearized around the nominal working point $V_{DCP}=V_{DCP,N}$ by expressing V_{DCP} in the form

$$V_{DCP}{}^2 \approx V_{DCP,N}{}^2 + 2V_{DCP,N}\Delta V_{DCP}, \tag{6.23}$$

where ΔV_{DCP} is the variation of V_{DCP} with respect to $V_{DCP,N}$. Using (6.23) and a similar expression for $V_{DCP,ref}{}^2$, the diagram of Fig. 6.7 has been redraw as in Fig. 6.8. The block $I_G \rightarrow I_{FEC}$ has been replaced by

$$I_{DCP} = \frac{V_{G,N}}{2V_{DCP,N}} I_G \tag{6.24}$$

obtained neglecting the losses of the FEC and in the hypothesis that the current i_G is in phase with the voltage v_G and that the voltage V_{DCP} remains close to its nominal value. The

$C_{VDCP,PG}(s)$ controller was designed on the basis of Fig. 6.8 using the same technique described in Subsection 6.4.1. The Bode diagram for V_{DCP} control loop is shown in Fig. 6.9 where, as in the previous figure, the dotted green line represents the diagram of the open-loop system without the controller; the dashed red line refers to the open-loop controlled system, and the solid blue line shows the Bode diagram of the closed-loop controlled system.

From equation (6.4), and (6.5) as mention in section 6.4.1 the gain of continuous-time PI controller are

$$K_{P,V_{DCP}} = 0.0377, \tag{6.25}$$

$$K_{I,V_{DCP}} \triangleq 0.3188 \tag{6.26}$$

Respectively the gain in the discrete domain from is obtain in (6.14), and (6.15). by putting the value of $\mathbf{K_{P,V_{DCP}}}$ and $\mathbf{K_{I,V_{DCP}}}$ (6.9) and (6.10) where $\boldsymbol{\tau = T}$

$$K_{e(k),V_{DCP}} = 0.0376845537993056 \tag{6.27}$$

$$K_{e(k-1),V_{DCP}} = -0.0376695569697946 \tag{6.28}$$

6.4.2.2 Generation of $i_{G,ref}$

The power reference $P_{G,ref}$ computed by $C_{VDCP,PG}(s)$ is further manipulated to work out the grid current reference $i_{G,ref}$ for ICL of i_G.

In static converters connected to the three-phase grid, the power control algorithm is often developed on the basis of the theory of instantaneous power [15]. The application of this theory requires a prior transformation of the three-phase voltages from the reference frame a,b,c to the stationary reference frame α,β,γ and, eventually, to the synchronous reference frame d,q,0 by means of the well know Clarke and Park matrixes.

In a three-phase system without neutral, or when the sum of the phase currents is identically zero, the theory of instantaneous power defines the real instantaneous power p and the imaginary instantaneous power q as

$$\begin{aligned} p &\triangleq \frac{3}{2}\left(v_\alpha i_\alpha + v_\beta i_\beta\right) = \frac{3}{2}\left(v_d i_d + v_q i_q\right) \\ q &\triangleq \frac{3}{2}\left(v_\alpha i_\beta - v_\beta i_\alpha\right) = \frac{3}{2}\left(v_d i_q - v_q i_d\right)' \end{aligned} \tag{6.29}$$

where i_α, i_β, i_d, and i_q are the current components in the stationary and in the synchronous reference frames.

In a three-phase system with symmetrical voltages and balanced currents, the real instantaneous power corresponds to the active power whilst the imaginary instantaneous power corresponds to the opposite of the reactive power. From this property it derives that, if the

reference for the active and the reactive power are given, by inversion of (6.29) it is possible to work out the corresponding references for the currents in the stationary and/or in the synchronous reference frames by means of

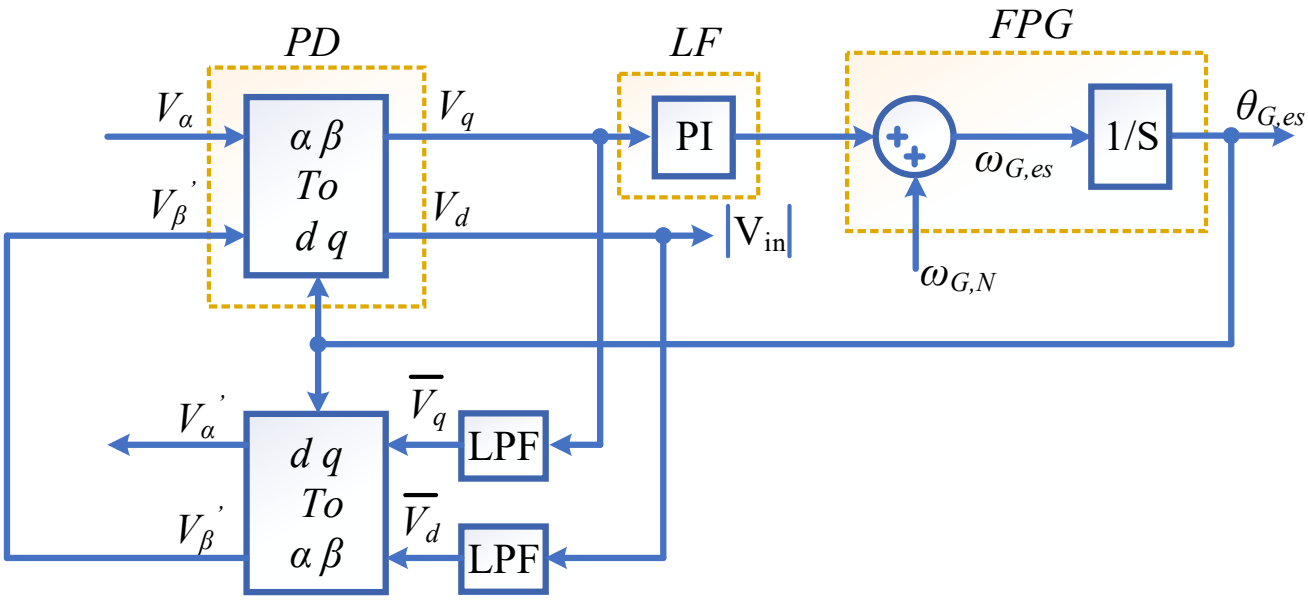

Fig. 6.10 Block diagram of a inverse Park -PLL

$$i_\alpha = \frac{2}{3}\frac{pv_\alpha - qv_\beta}{{v_\alpha}^2+{v_\beta}^2}, \qquad i_d = \frac{2}{3}\frac{pv_d - qv_q}{{v_d}^2+{v_q}^2}$$
$$i_\beta = \frac{2}{3}\frac{pv_\beta + qv_\alpha}{{v_\alpha}^2+{v_\beta}^2}, \qquad i_q = \frac{2}{3}\frac{pv_q + qv_d}{{v_d}^2+{v_q}^2}. \qquad (6.30)$$

In single-phase systems, like the BWV2H, the Clarke transformation cannot be applied because only one phase voltage is available. Nevertheless, v_α and v_β are computed considering that $v_\alpha = v_G$ and that v_β has the same waveform as v_G but lags it by 90°. The subsequent Park transformation requires to know the instantaneous phase θ_G of v_G, obtained by means of a PLL. If a Park based PLL is used, the voltage components v_d and v_q are obtained as a side-product of the computation as shown in the diagram of Fig. 6.10 have oscillations. The oscillations are attenuated by LPF, that present in a loop between the direct and inverse Park transform performs to obtain $\overline{\boldsymbol{v}}_{\boldsymbol{d}}$ and $\overline{\boldsymbol{v}}_{\boldsymbol{q}}$. Indeed, $\boldsymbol{v}'_{\boldsymbol{\alpha}}$ and $\boldsymbol{v}'_{\boldsymbol{\beta}}$ achieve by implementing the inverse Park transform to $\overline{\boldsymbol{v}}_{\boldsymbol{d}}$ and $\overline{\boldsymbol{v}}_{\boldsymbol{q}}$. In simulating the BWV2H the one described in [14] has been adopted.

Once v_d, v_q, and θ_G are obtained from the PLL, the active power references coming from $C_{VDCP,PG}(s)$, and, possibly, the reactive power reference generated by a suitable control loop, are processed according to the block diagram of Fig. 6.11 to work out $i_{G,ref}$. The gain 3 between i_α and $i_{G,ref}$ is explained considering that the instantaneous power theory used to derive $i_{G,ref}$ is based on the assumption of operating with a three phase system, but in the actual BWV2H the full power must be exchanged through a single phase.

It has been hypothesized that in the initial phase of the simulation the grid operated at a frequency of 314 rad and with nominal voltage of 325 V. In addition, the initial voltage of the capacitor has been set to 365 V and it is assumed that the HFPC did not absorb power. So, in the first moments of operation of the system, capacitor C_{DCP} was loaded up to its rated voltage

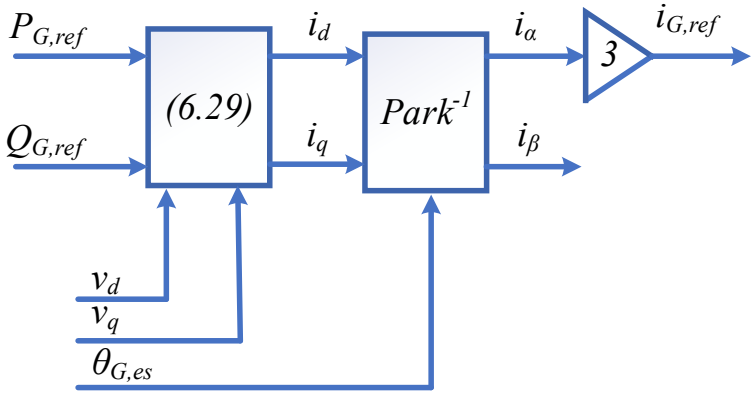

Fig. 6.11 Block diagram for the generation of $i_{G,ref}$.

of 450 V and then kept in such condition. From the instant t=0.5 s the power absorbed by the HFPC has been increased to 80% of the rate with a ramp lasting 0.1 s. Instantly t= 1 s the grid frequency was increased to 320.28 rad in 0.1 s and from the instant t= 1.5 s the grid voltage was increased to 358 V, i.e. 110% of the nominal with a ramp lasting 0.1 s; finally, instantly t=2 s the flow of power absorbed by the HFPC has been reversed, bringing it to -80% of the nominal with a ramp lasting 0.2 s.

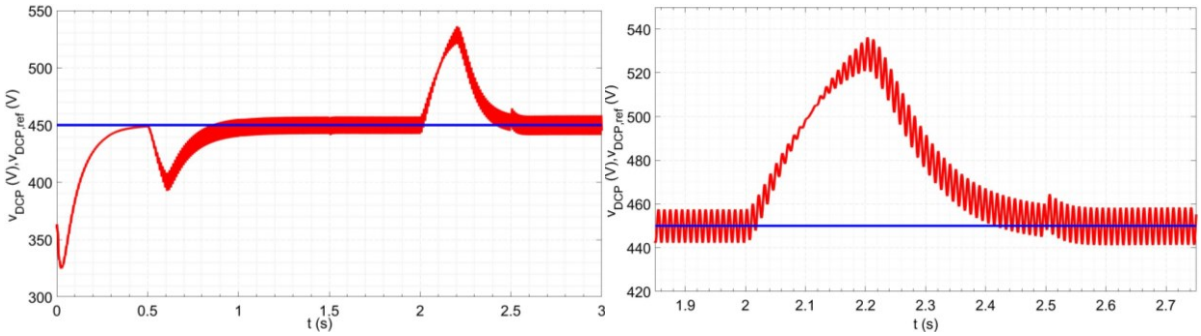

Fig. 6.12 Primary DC voltage reference (blue) $V_{DCP,ref}$ and control primary DC voltage (red) V_{DCP}

The V_{DCP} voltage trend during this operations is shown in the left half of Fig 6.12 with the red line; the blue line is the reference for V_{DCP}. The Fig. shows how in the initial the capacitor C_{DCP} is discharged instead of loaded, however after less than 0.1 s the charging process is actually started and around 0.4 s the capacitor reaches the reference voltage $V_{DCP,N}$. The initial discharge of the capacitor is due to the transient PLL, which initially does not provide the correct phase of the grid voltage and consequently makes it impossible to correctly fix the sign of the power exchanged with it. This problem can be easily solved by delaying the power exchange by a few fractions of a second compared to activating the BWV2H control system to give the PLL time to synchronize with grid voltage. It is noted that during the charging the capacitor the voltage V_{DCP} smooth and there are no undulations. Latter, on the other hand, after 0.5 s, the capacitor is discharged from HFPC and it is necessary to recharge it by current i_{FEC}

obtained by straightening the grid current. In the first phase of charging the i_{FEC} it is quite low, so that the undulations produced on the capacitor voltage are contained. When it is necessary to compensate for the power taken from the HFPC, this current is greater and therefore the voltage oscillations also grow. This phenomenon is also present during the inversion of power absorbed by the HFPC. As shown in the right half of Fig 6.12, initially the V_{DCP} voltage increases and as a result the amplitude of the current I_{FEC} is reduced to zero, thus reducing the amplitude of the oscillations; subsequently the control ring of V_{DCP} requires the absorption from the grid of a current of increasing amplitude but of opposite phase in order to discharge the C_{DCP} capacitor, so that the voltage oscillations at its heads resume to increase until they reach the amplitude present before the power reversal. If you look at the left half of Fig 6.12, you can see that neither the change in the grid frequency nor the variation in its amplitude have visible effects on $V_{DCP.}$

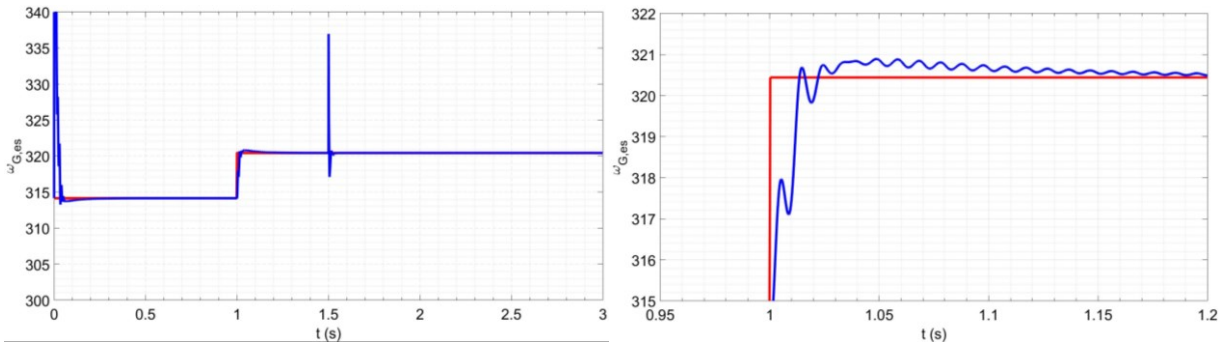

Fig. 6.13 Grid frequency estimate by the PLL(blue) and real grid frequency(red)

These changes, on the other hand, have a significant influence on the PLL's estimate of grid frequency. The left half of Fig 6.13 shows with the red line the grid angular frequency estimated by the PLL during the test sequence while with the blue line it shows its real value. Apart from the initial transient, during which the error is very large, it is noted that the PLL is able to provide an accurate estimate of the grid angular frequency. When it presents the step variation from 314 rad to 320.44 rad the PLL provides the correct estimate within about 0.4 s after having produced an over elongation of about 0.45 rad, as shown in the right half of Fig 6.13. At full speed there remains an estimated error about sine with twice the frequency of the grid.

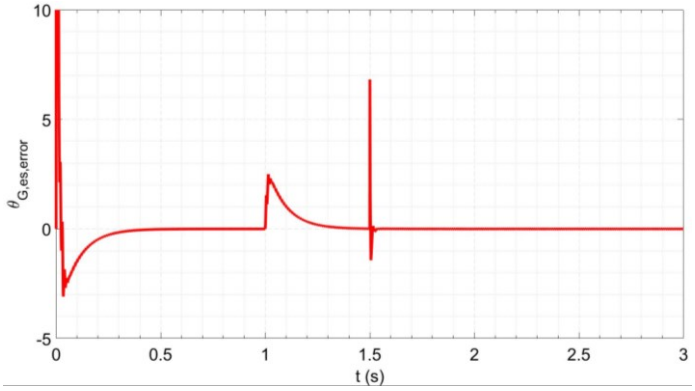

Fig. 6.14 Grid phase estimate error

Fortunately, errors in the frequency estimate have only a marginal impact on the grid phase estimate, as shown in Fig 6.14. Except in the very first moments of operation, both when the system is starting and if the change in the grid frequency at time 1s, the error in estimating the

phase of the grid voltage remains less and less than 3°. When the grid voltage has the amplitude variation at time 1.5s, despite a considerable error in estimating the frequency, the phase estimation error is less than 8°. The Fig. shows that at full speed the phase estimation error has a range of high-frequency oscillations about zero-centered. This is due to the fact that the phase of the grid voltage varies continuously over time while the phase estimated by the PLL is updated in discrete time.

The block shown as $P_{G,ref}$->$I_{,G,ref}$ in Fig 6.11 implements Equation (6.29) and generates the reference $i_{d,ref}$ for the current component that involves exchanging active power with the grid. Since in this case there is no reactive power involvement, the absolute value of $i_{d,ref}$ multiplied by 3 corresponds to the amplitude reference for the grid current. It is shown with the green line in the left half of Fig 6.15. According to the conventions adopted, when the $i_{d,ref}$ is negative the BWV2H delivered power to the grid while when the $i_{d,ref}$ is positive the power is absorbs from the grid. In the same Fig. the grid current is shown with the red line; the comparison between the two waveforms confirms the correct functioning of the control ring of i_G. The right half of Fig 6.15 refers to the initial charge of the capacitor and shows with the green line the trend of $i_{d,ref,}$ with the blue line the reference $i_{G,ref}$ and with the red line the actual value of i_G. It is noted that the $i_{d,ref}$ is subject to a small oscillation that increases with the amplitude of the current. It is due to the residual oscillation present at the exit of the notch filter placed on the feedback path of the control ring of V_{DCP} whose regulator generates the reference $P_{DCP,ref}$ from which $i_{d,ref}$

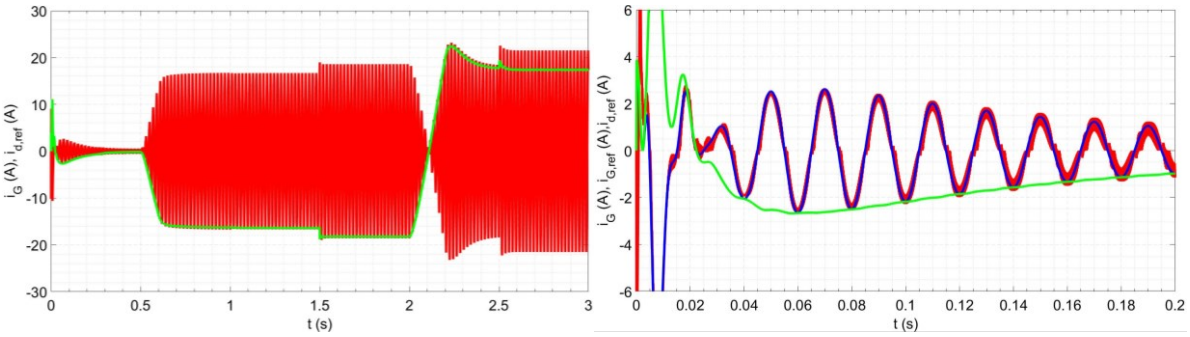

Fig. 6.15 Grid current actual (red) , $i_{d,ref}$ (green), and estimated grid current(blue)

is then obtained. The block referred to as Anti-Park in Fig 6.10 implements switch from $i_{d,ref}$ to $i_{G,ref}$. This operation is accurate, in fact the peaks of the sine blue of Fig 6.15 lie on the red curve. Finally, the comparison between the $i_{G,ref}$ and i_G confirms that the grid current control ring operates correctly even under dynamic conditions.

In the left half of Fig 6.16 are shown the trends of the grid current has the amplitude variation at time 1.5s, the same magnitudes at the time of the step-by-step increase in the amplitude of the grid voltage while the right half of the Fig. refers to the inversion of power deliver and absorbed by the HFPC. In the first case, to keep the deliver power constant, the reference for the amplitude of the current $i_{G,ref}$ (blue) is promptly reduced and the actual grid current grid current i_G (red) reduce and also a 180° shift of the current with respect to the grid voltage (black) demand in about 2ms. In the second case, the amplitude of the current absorbed by the grid is

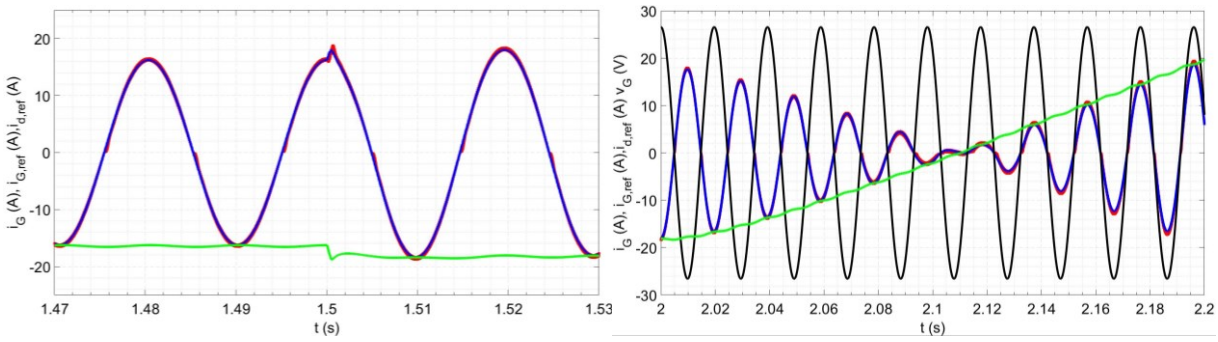

Fig. 6.16 Grid current estimate (blue) and real grid current (red), $i_{d,ref}$ (green), and grid voltage (black)

initially increased again until it reaches a value higher than the initial value, to keep the absorbed power constant, the reference for the amplitude of the current is promptly increase and the actual grid current is in phase with the grid voltage. The change of direction of power flow is highlighted by the fact that the $i_{d,ref}$ (green)changes sign.

6.4.3. Control of the amplitude of the secondary coil current during battery charging

When the power flows from the grid to the battery, HFPC acts as an inverter and HFSC act as active rectifier, its gate commands are generated by I_S current loop to deal with single PI control, to make system cost effective. The control method is base on the DPS modulation method, in which both bridge converters are control. Thanks to the series resonance, the first harmonic components of the HFPC output voltage v_{HFPC} is about equal to the voltage induced across the primary coil, and consequently, its amplitude is proportional to that of the current i_S flowing in the secondary coil. Based on this condition, during the battery charging, I_S current loop manipulates v_{HFPC} and v_{HFSC} to control I_S.

6.4.3.1. Current transduction is

The design of the I_S controller presents some difficulties due to the high frequency of the alternating quantities involved in the operation of the coupled coils. It is reasonable to assume that the frequency of sampling and processing of the BWV2H control algorithm is at most equal to the feed frequency of the coils. Consequently, it is not possible to control the waveform of the current i_s for an instant but only its peak amplitude, while it maintains an almost sine waveform due to the filtering effect of the compensation networks. It is therefore necessary to create a transduction and conditioning circuit which makes available to the analog digital converter of the microcontroller a voltage proportional to the peak amplitude of i_s. An example of such a circuit is given in Fig 6.17, which also shows an indicative representation of the waveform of signals exchanged between the different stages of the circuit.

The instantaneous value of currents is assumed to be translated by means of a Hall effect probe or another type of transducer. The signal at the transducer output is then processed by a high pass filter (HPF) to eliminate any continuous component due to transducer offsets. The output of the high pass filter is straightened to obtain its absolute value which, in turn, constitutes the input of a LPF. This filter provides the average value of the straightened value of the current and allows you to trace its peak value by the relation

$$I_{peck} = \frac{\pi}{2} I_{average} \,. \tag{6.31}$$

The (6.31) is valid only if the currents are sinusoidal, but this condition is well verified in resonant wireless systems. Particular attention should be paid to the size of the LPF: its cutting frequency must be low enough to effectively attenuate the oscillations present at the

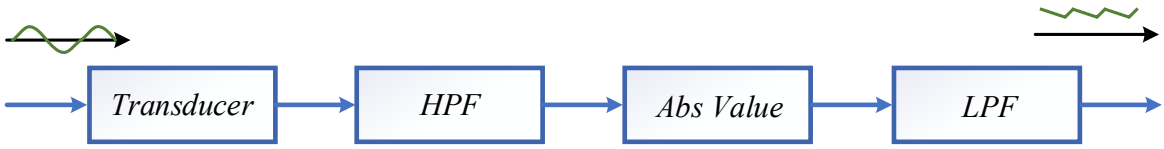

Fig. 6.17 Principle diagram of the acquisition circuit

output of the circuit, but high enough to allow the filter output to faithfully follow changes in the peak amplitude of the current. The cutting frequency of both the high pass filter and the low pass filter has been set at 1kHz.

In designing the controller, the coil current transduction circuit was modeled using the TF

$$T_{I_t}(s) = T_{I_r}(s) = \frac{\pi}{2} \frac{1}{1+s\tau_{PB}} \tag{6.32}$$

con τ_{PB}=1.5e-4.

6.4.3.2. Transfer function between the peak value of v_{HFPC} and the peak value of i_S

The TF from the first harmonic of v_{HFPC} to i_S is obtained from the equivalent circuit of the coupled coils sketched in Fig. 6.18 and results in

$$G_{v_{HFPC},i_S}(s) = -\frac{MC_S C_P s^3}{D_4 s^4 + D_3 s^3 + D_2 s^2 + D_1 s + 1}, \tag{6.33}$$

obtained by using the complex variable "s" instead of "jω" in representing the reactive components of the circuit and then working out the ratio i_S/v_{HFPC} by means of the conventional approach based on the Kirchhoff laws. The coefficients of the denominator of $G_{vHFPC,iS}(s)$ are equal to

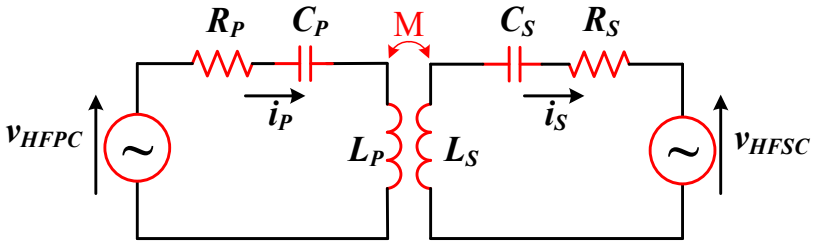

Fig. 6.18 Equivalent circuit of the coupled coils.

$$\begin{aligned} D_4 &= C_S C_P L_S L_P - C_S C_P M^2 \\ D_3 &= C_S C_P L_S R_P + C_S C_P L_P R_S \\ D_2 &= C_S L_S + C_P L_P + C_S C_P R_S R_P \\ D_1 &= C_S R_S + C_P R_P \end{aligned} \qquad (6.34)$$

and its Bode diagrams are plotted in Fig. 6.19.

Generally speaking, it is reasonable to assume that the sampling and processing frequency of i_S current loop is at most equal to the supply frequency of the coils. In the considered application, it is even a submultiple. Consequently, it is not possible to control the actual waveform of i_S but only its amplitude I_S, relying on the filtering effect of the compensation network to enforce the current to maintain an almost sinusoidal waveform.

On the other hand, v_{HFPC} cannot be freely manipulated because only the amplitude V_{HFPC} of its first harmonic component is directly affected by the phase shift angle between the gate commands of the legs of the HFPC. Then, the TF $G_{vHFPC,iS}(s)$ is not useful in designing the controller of i_S current loop and must be substituted for by the TF from V_{HFPC} to I_S. It can be demonstrated [28] that if the bandwidth of the variations of V_{HFPF} is much smaller than the supply frequency, and if the amplitude Bode diagram of $G_{vHFPC,iS}(s)$ is smooth enough around the supply frequency, as it happens in the considered case, then the TF that links V_{HFPC} to I_S can be simply approximated by the gain of $G_{vHFPC,iS}(s)$ computed at the supply frequency, i.e. by

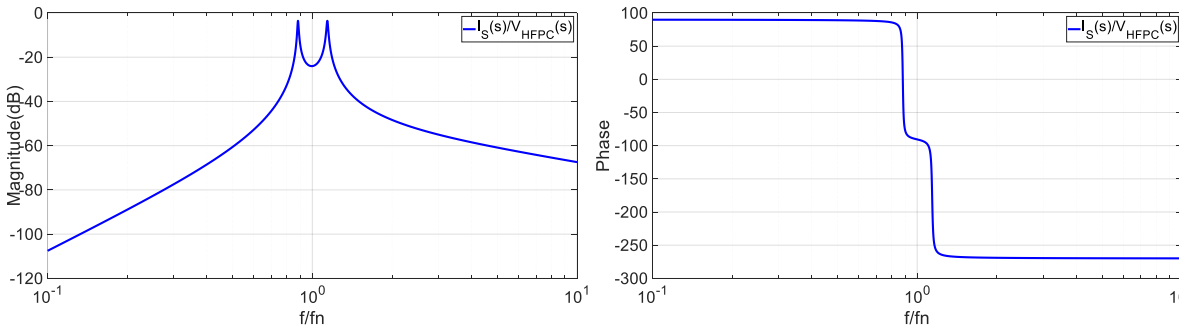

Fig. 6.19 Bode diagram of $G_{VHFP,iS}(s)$.

$$K_{V_{HFPC},I_S} = \frac{1}{\omega_{HF} M}, \tag{6.35}$$

where ω_{HF} is the supply angular frequency. With the parameters of Table. 6.1, it results $K_{VHFPC,IS}$=0.083.

When designing the controller of I_S, it must be remembered that the computation of $I_{S,ref}$ and the transduction of I_S are performed in the secondary section of the BWV2H, whilst the manipulated voltage v_{HFPC} is related to the primary section. It is therefore necessary to set up a communication channel between the two sections. A viable solution is to employ a pair of radio transceivers operating on the industrial, scientific and medical (ISM) band. It is reasonable to assume a refresh period of the transmitted data of 1 ms.

The block diagram of the control loop of I_S is shown in Fig. 6.20. The blocks within the dashed red rectangle are located on the primary section of the BWV2H whilst the others are on the secondary section. The blocks crossed by the rectangle interface the two sections: TD(s) represents the delay due to data transmission, whilst $K_{VHFPC,IS}$ approximates the TF from V_{HFPC} to I_S. The blocks SD(s) and $C_{IS,VHFPC}(s)$ represent the microprocessor delay and the controller, respectively. Like in the previous subsection, SD(s) is computed supposing that the sampling frequency of the microcontroller is one fourth of the HFPC switching frequency. The amplitude I_S is obtained by processing the signal coming from the transduction of i_S using an analog peak detector with a bandwidth of 10 kHz [28]. It is represented by the PD(s) block in the feedback path of the diagram of Fig. 6.20.

The Bode diagrams of the open-loop system without the controller, obtained using the parameters from Table. 6.1, are plotted with the dashed green line in Fig. 6.21. Initially, $C_{IS,VHFPC}(s)$ has been designed as a PI controller, sizing its gains in order to obtain a control loop with a bandwidth of 50 Hz and a phase margin of 80°. However, with this approach, the closed-loop gain at high frequencies was not effectively attenuated, and undue oscillations occurred in the system response. To prevent this issue, the controller architecture has been modified by inserting an additional pole at a frequency of 2 kHz. The pole has been considered part of the forward path of the system to be controlled, and the gains of $C_{IS,VHFPC}(s)$ have been computed again to maintain the same bandwidth and phase margin. The Bode diagrams of the open-loop and closed-loop systems with the enhanced controller are shown in Fig. 6.21 using

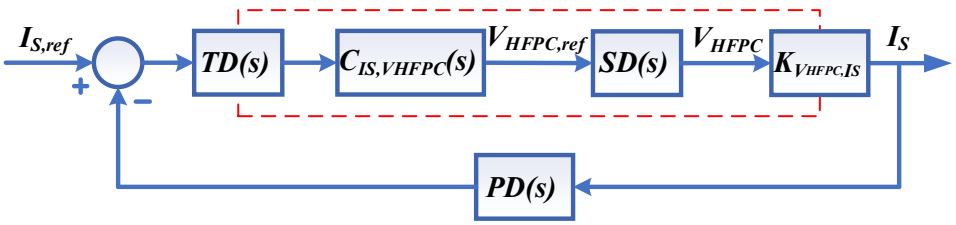

Fig. 6.20 Block diagram of control loop of I_S.

the dashed red line and the solid blue line, respectively.

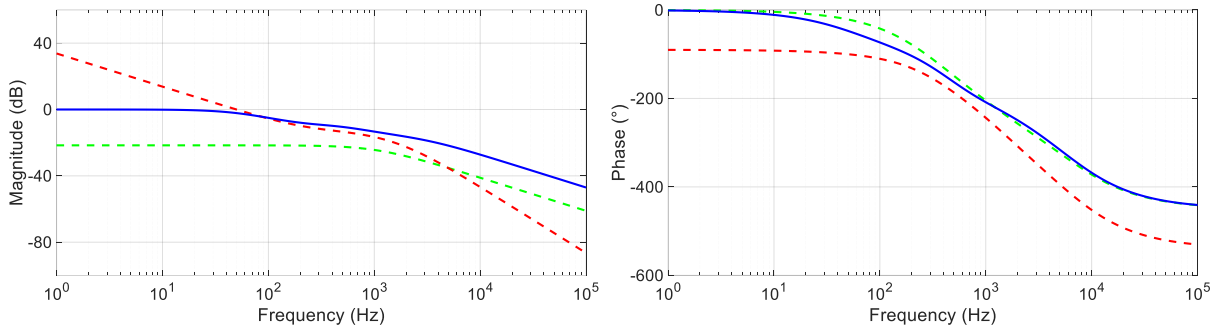

Fig. 6.21 Bode diagrams relevant to I_S current loop. Open-loop uncontrolled system (dashed green), open-loop controlled system (dashed red), closed-loop controlled system (solid blue)

Once computed $V_{HFPC,ref}$, the phase phase shift angle between the gate commands of the legs of the HFPC and HFSC are obtained as [26]

$$\alpha = \beta = 2arcsin\left(\frac{\pi}{4}\frac{V_{HFPC,ref}}{V_{DCP}}\right). \qquad (6.36)$$

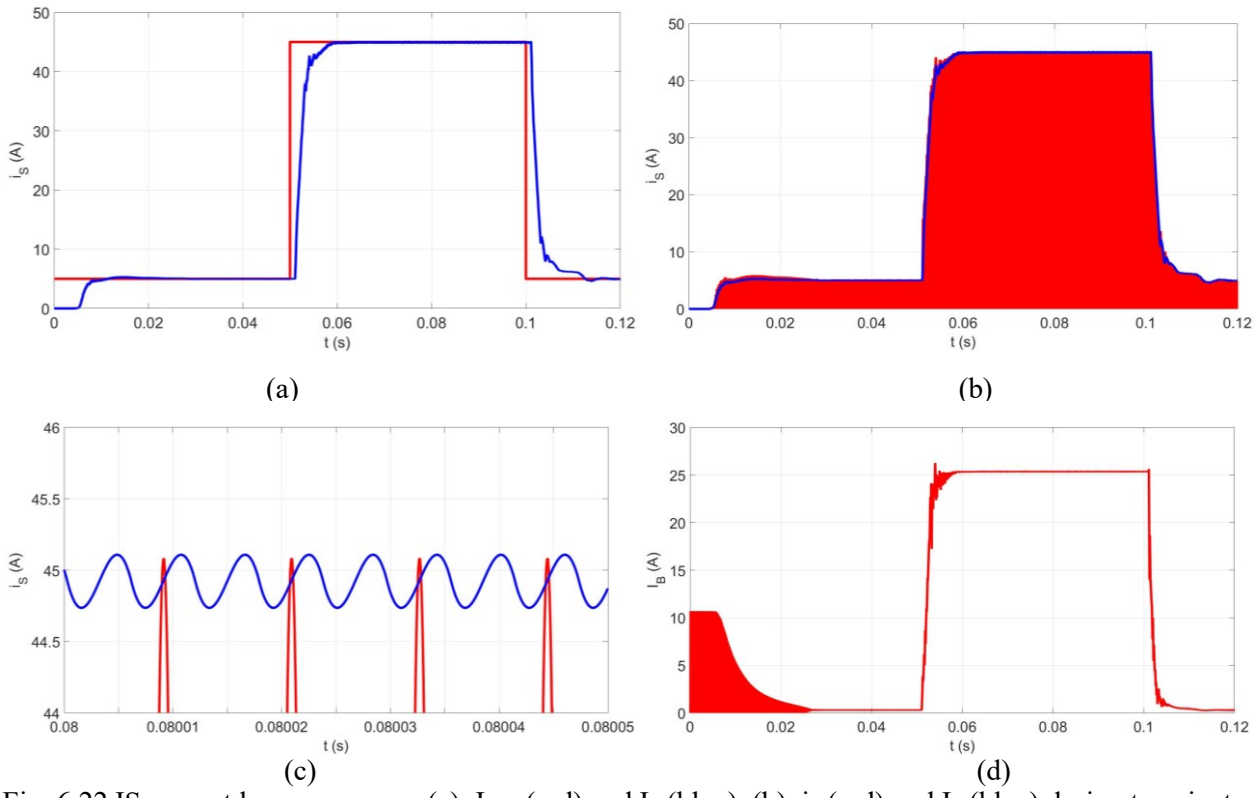

Fig. 6.22 IS current loop responses. (a): $I_{S,ref}$ (red) and I_S (blue). (b): i_S (red) and I_S (blue) during transient and their magnifications in (c), and (d): I_B (red)battery charging current .

The discrete version of the controller has been inserted into a simulation along with a circuital model of the HFPC and of the coupled coils to check the performance of the control algorithm. The response to an $I_{S,ref}$ (red) a square wave was used with frequency of 10 Hz, step from minimum value 5A to maximum value 45 A has been considered, obtaining the plots reported in Fig. 6.22. The solid blue line represents I_S (blue) obtained at the output of PD(s). It can be seen that the control loop reaches the steady state in about 60 ms without any overshoot,

even if a small oscillation is superimposed on the response shown in Fig 6.22(a). Fig 6.22(b) shows the waveforms of i_S (red) and I_S (blue) during the transiant up to 0.12 s. Because of its high frequency, at the time scale of the Fig., i_S appears as a solid red area with I_S following its envelope. It is worth highlighting that the peak detector operates accurately only at steady state and if i_S is sinusoidal. During the transient, these conditions are not satisfied and this explains why, in the first 5 ms after the reference step, the correspondence between I_S and the actual amplitude of i_S is not perfect. The magnification of the Fig., which is relevant to the steady state condition, shows that I_S tracks the amplitude of i_S accurately even if some oscillation at twice the supply frequency can be found in Fig 6.22 (c). However, Fig. 6.22 (d) repersent the battery charging current I_B (red) step from 1A to 26 A has been considered.

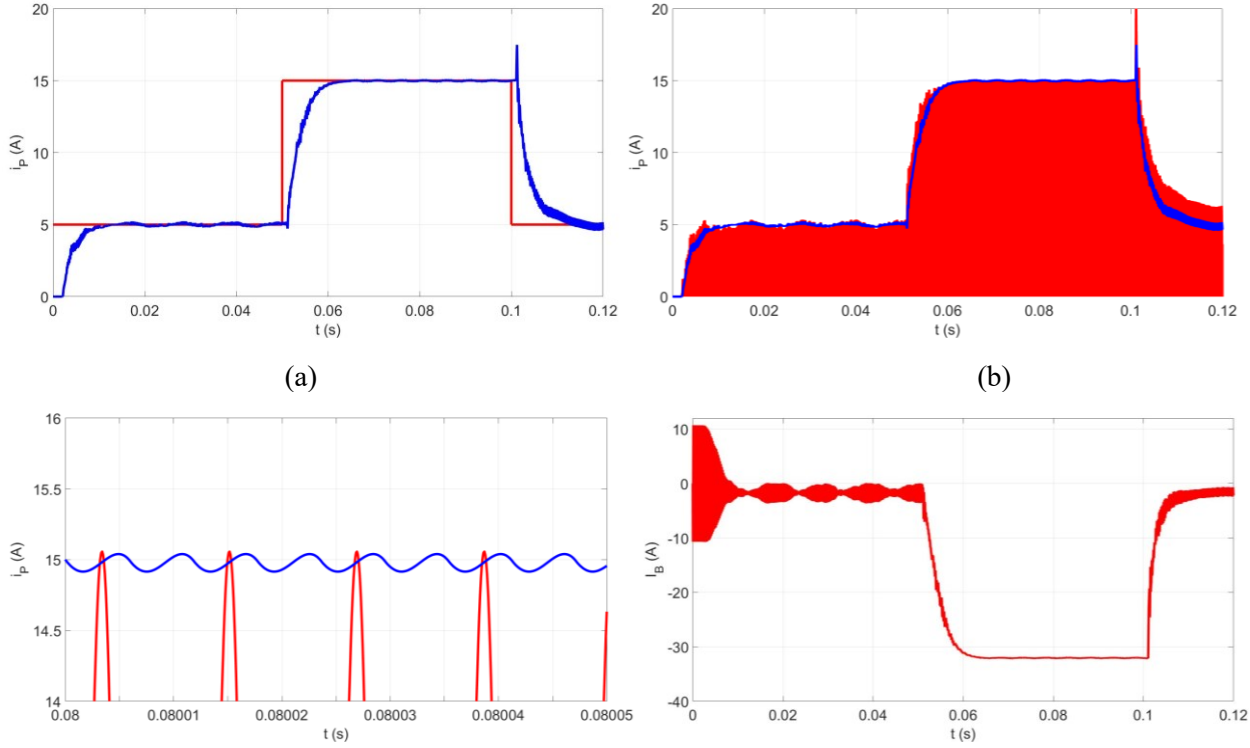

Fig. 6.23 IS current loop responses. (a): $I_{P,ref}$ (red) and I_P (blue). (b): i_P (red) and I_P (blue) during transient and their magnifications in (c), and (d): I_B (red) battery discharging current.

6.4.3.3 Control of the amplitude of the primary coil current during battery discharging

When the power flows from the battery to the grid, the functions of the two power converters are exchanged, and I_P current loop generates the gate commands for HFSC and HFPC. Where as HFSC work as the inverter and HFPC work as the active rectifier. In this case, the reference $I_{P,ref}$ and the transduction of I_P are performed in the primary section of the BWV2H, whilst the manipulated voltage v_{HFSC} and v_{HFPC} to control I_P current. Hence, the use of the radio transceiver and the relevant refresh period of 1ms must be considered in designing the controller $C_{IP,VHFSC}(s)$ as well. The design procedure is the same as that described for $C_{IS,VHFPC}(s)$ in the previous subsections. The results obtained from the simulation of this control loop are reported in Fig. 6.23. It clearly appears that the responses are quite similar to those relevant to I_S current loop.

6.5 Conclusion

This chapter faced the topic of developing a control strategy for a wireless battery charger system with V2H functionality. The proposed strategy is based on the control of the voltages of the dc buse and of the battery and is carried out by manipulating the power exchanged between the grid and the battery through the static power converters and the coil coupling. This approach allows to satisfy the charging and discharging requirements of the battery and at the same time to avoid exceeding the voltage or current ratings of the converters.

The control strategy is arranged in two levels: the algorithms of the internal level process the current references and the feedback signals transduced from BWV2H circuits to generate the gate commands for the static converters, while the external level control algorithms generate the references for the power to be exchanged between the various stages and between the two sections of the BWV2H. The functioning of the internal level algorithms has been verified in the Simulink environment using accurate circuital models of the various power converters that constitute the BWV2H..

6.6 References

1. Bertoluzzo, M., Giacomuzzi, S., Kumar, A. “Design of a Bidirectional Wireless Power Transfer System for Vehicle-to-Home Applications,” Vehicles., 2021, 3, pp.406-425

2. Kumar, A., Neogi N., “Bidirectional Converter and Energy Storage System,” International Journal of Enhanced Research in Science Technology & Engineering, 2015, 4, pp. 15-23

3. D. Patil, M. K. McDonough, J. M. Miller, B. Fahimi and P. T. Balsara, “Wireless Power Transfer for Vehicular Applications: Overview and Challenges,” IEEE Trans. Transp. Electrification, 2018, 4, pp. 3-37

4. G. Buja, R. K. Jha, M. Bertoluzzo and M. K. Naik, “Analysis and comparison of two wireless battery charger arrangements for electric vehicles,” Chin. J. Electr. Eng. 2015,1, pp. 50-57.

5. U. Vuyyuru, S. Maiti and C. Chakraborty, “Active Power Flow Control Between DC Microgrids,” IEEE Trans Smart Grid, 2019, 10, pp. 5712-5723.

6. P. He and A. Khaligh, “Comprehensive Analyses and Comparison of 1 kW Isolated DC–DC Converters for Bidirectional EV Charging Systems,” IEEE Trans. Transp. Electrification, 2017, 3, pp. 147-156.

7. Z. H. Shi, Z. C. Qiu, X. Y. Chen and M. Y. Li, “Modeling and Experimental Verification of Bidirectional Wireless Power Transfer,” IEEE Trans. Appl. Supercond. 2019, 29, pp. 1-5.

8. F. Liu, K. Li, K. Chen and Z. Zhao, “A Phase Synchronization Technique Based on Perturbation and Observation for Bidirectional Wireless Power Transfer System,” IEEE

Trans. Emerg. Sel. 2020 , 8, pp. 1287-1297

9. D. Dong, I. Cvetkovic, D. Boroyevich, W. Zhang, R. Wang and P. Mattavelli, “Grid-Interface Bidirectional Converter for Residential DC Distribution Systems—Part One: High-Density Two-Stage Topology,” IEEE Trans. Power Electron 2013, 28, pp. 1655-1666.

10. C. A. Hill, M. C. Such, D. Chen, J. Gonzalez and W. M. Grady, “Battery Energy Storage for Enabling Integration of Distributed Solar Power Generation,” IEEE Trans. Smart Grid, 2012, 3, pp. 850-857.

11. M. tabari and A. Yazdani, “Stability of a dc Distribution System for Power System Integration of Plug-In Hybrid Electric Vehicles,” IEEE Trans. Smart Grid 2014, 5, pp. 2564-2573.

12. G. Delille, B. Francois and G. Malarange, “Dynamic Frequency Control Support by Energy Storage to Reduce the Impact of Wind and Solar Generation on Isolated Power System's Inertia,” IEEE Trans. Sustain. Energy, 2012, 3, pp. 931-939.

13. V. Monteiro, J. G. Pinto and J. L. Afonso, “Operation Modes for the Electric Vehicle in Smart Grids and Smart Homes: Present and Proposed Modes,” IEEE Trans. Veh. Technol, 2016, 65, pp. 1007-1020.

14. M. Bertoluzzo, S. Giacomuzzi and A. Kumar, “Design and Experimentation of a Single-Phase PLL With Novel OSG Method, IEEE Access, 2022, 10, pp. 33393-33407.

15. H. Akagi, Y. Kanazawa, A. Nabae, “Generalized Theory of the Instantaneous Reactive Power in Three-Phase Circuits,” Proc. IPEC83, 1983, pp. 1375-1386.

16. Wireless Power Transfer for Light-Duty Plug-In/Electric Vehicles and Alignment Methodology, J2954, SAE International, 2020.

17. W.L. Malan, D. M. Vilathgamuwa, and G. R. Walker, “Modeling and control of a resonant dual active bridge with a tuned CLLC network,” IEEE Trans. Power Electron 2015, 31, pp. 7297–7310.

18. R. K. Jha, G. Buja, M. Bertoluzzo, S. Giacomuzzi and K. N. Mude, “Performance Comparison of the One-Element Resonant EV Wireless Battery Chargers,” IEEE Trans. Ind Appl, 2018, 54, pp. 2471-2482.

19. J. M. Miller, O. C. Onar and M. Chinthavali, “Primary-Side Power Flow Control of Wireless Power Transfer for Electric Vehicle Charging,” IEEE Trans. Emerg. Sel, 2015, 3,pp. 147-162.

20. Italian Electrotechnical Committee (CEI), Reference technical rules for the connection of active and passive users to the LV electrical Utilities. CEI 0-21 2019. https://www.ceinorme.it/it/norme-cei-0-16-e-0-21.html

Nomenclature

AC	Alternating Current
BMS	Battery Management System
BC	Bidirectional Chopper
C_{DCP}, C_{DCS}	High-Frequency Primary and Secondary Converter DC capacity
C_P, C_S	Primary and secondary resonant capacitor
δ	Duty cycle of the Bidirectional Chopper
DC	Direct Current
ΔI_O	Peak-to-peak current ripple on the inductor L_O
ΔV_{HFPC}	Peak-to-peak voltage ripple on the capacitor C_{HFPC}
η_c	Power converter efficiency
η_t	Transmission efficiency between the two coils
η_{tot}	Total efficiency of the V2H wireless system
FEC	Front-End Converter
f_G	Grid frequency
f_{HF}	Switching frequency of power converters supplying the coils
HFPC	High Frequency Primary Converter
HFSC	High Frequency Secondary Converter
I_{DCP}, I_{DCS}	Input current of HFPC and output current of HFSC in charging mode
I_{FEC}	FEC output current in charging mode
I_G	Grid-side current
I_{HFPC}, I_{HFSC}	Output current of HFPC and input current of HFSC in charging mode
I_O	Battery-side current
I_S	Secondary coil current
I_P	Primary coil current
L_{BC}	Chopper inductance
L_G	Grid filter inductance
L_O	Battery filter inductance
L_P, L_S	Primary and secondary coil self-inductance
M	Coils mutual inductance
P_G	Grid-side active power
P_{HFPC}	HFPC output active power in charging mode
P_{HFSC}	HFSC output active power in discharging mode
P_O,P_B	Battery-side active power
R_{eq}	Equivalent resistance seen from the HFPC
SoC	State of Charge of the battery
V2H	Vehicle to Home
V_B	Battery voltage
V_{BC}	BC voltage before the chopper inductance
V_{CP}, V_{CS}	Voltage across C_P and C_S
V_{DCP}, V_{DCS}	Voltage across C_{HFPC} and C_{HFSC}
V_{FEC}	Input FEC voltage (during charging mode)
V_G	Grid voltage
V_{HFPC}, V_{HFSC}	Output voltage of HFPC and input voltage of HFSC in charging mode

V_{LP}, V_{LS}	Voltage across L_P and L_S
V_P, V_S	Voltage across the primary and secondary coil
V_O	Output BC voltage (during charging mode)
WPT	Wireless Power Transfer
SAHFWPT	Single Active High-Frequency wireless power transfer
DAHFWPT	Dual Active High-Frequency wireless power transfer
SPS	Single Phase Shift
EPS	Extended Phase Shift
DPS	Dual Phase Shift
TPS	Triple Phase shift
EV	Electrical Vehicle
RE	Renewable Energy
ESS	Energy Storage System
SAB	Single Active Bridge
DAB	Dual Active Bridge
PSFB	Phase Shift Full Bridge
R_B	Battery Equivalent Resistance
C_O	Output low pass filter capacitor
ZVS	Zero Voltage Switching
ZCS	Zero Current Switching
V_{DCP_S}, V_{DCP_D}	DC voltage source of SAHFWPT and DAHFWPT
v_{HFPC_S}, v_{HFPC_D}	Output voltage of HFPC of SAHFWPT and DAHFWPT
i_{P_S}, i_{P_D}	Output current of HFPC of SAHFWPT and DAHFWPT
v_{HFSR_S}, v_{HFSC_S}	Input voltage of HFSR and HFSC of SAHFWPT and DAHFWPT
i_{S_S}, i_{S_D}	Input current of HFSR and HFSC of SAHFWPT and DAHFWPT
V_{O_S}, V_{O_D}	Input current of HFSR and HFSC of SAHFWPT and DAHFWPT
ω_r	Resonant Frequency
Φ	External Phase shift angle
α	Internal phase shift angle of HFPC
β	Internal phase shift angle of HFSC
v_{HFPC_M}, v_{HFSC_M}	Peak amplitude of output and input voltage of HFPC and HFSC of DAHFWPT
v_{HFSR_M}	Peak amplitude of input voltage of HFSR of SAHFWPT
M	Coils mutual inductance
P_{PS}	Average power flow from primary to secondary
v_{HFPC_1}, v_{HFSC_1}	Fundamental Output and Input voltage of HFPC and HFSC of DAHFWPT
v_{HFSR_1}	Fundamental of Input voltage of HFSR of SAHFWPT
$i_{P\_D\_1}, i_{P\_S\_1}$	Fundamental primary coil current of DAHFWPT and SAHFWPT
i_{s_1}	Fundamental secondary coil current of DAHFWPT and SAHFWPT
$P_{DAHFWP\_S}, P_{SAHFWPT\_S}$	Secondary Power of DAHFWPT and SAHFWPT
$P_{S-S\_coil\_DAHFWPT\_loss}, P_{S-S\_coil\_SAHFWPT\_loss}$	Coil Loss of DAHFWPT and SAHFWPT

$\eta_{S-S\_coil\_DAHFWPT\_loss}, \eta_{S-S\_coil\_SAHFWPT}$	Efficiency of coil of DAHFWPT and SAHFWPT
$P_{HFPR\_Cond\_S\_loss}, P_{HFSR\_Cond\_loss}$	Conduction loss of HFPC and HFSR of SAHFWPT
$P_{HFPR\_Cond\_D\_loss}, P_{HFSC\_Cond\_loss}$	Conduction loss of HFPC and HFSC of DAHFWPT
$P_{HFSC\_on\_off\_loss}$	Switching loss of switches for HFSC
$P_{HFPC\_on\_off\_D\_loss}, P_{HFPC\_on\_off\_S\_loss}$	Switching loss of switches for HFPC of DAHFWPT and SAHFWPT
P_{Coss_loss}	Output capacitor loss of MOSFET
P_{body_loss}	Body diode reverse recovery loss
η	Efficiency
P_O	Output Power
P_{in}	Input Power
P_{loss}	Power Loss
$P_{SAHFWPT\_loss}$	Overall loss Power of SAHFWPT
$P_{DAHFWPT\_loss}$	Overall loss Power of DAHFWPT
$\eta_{SAHFWPT}$	Efficiency of SAHFWPT
$\eta_{DAHFWPT}$	Efficiency of DAHFWPT

Publications

a) Journal Papers

I. Bertoluzzo, M.; Giacomuzzi, S.; **Kumar, A**. Design of a Bidirectional Wireless Power Transfer System for Vehicle-to-Home Applications. *Vehicles* 2021, *3*, 406-425. https://doi.org/10.3390/vehicles3030025

II. M. Bertoluzzo, S. Giacomuzzi and **A. Kumar**, "Design and Experimentation of a Single-Phase PLL With Novel OSG Method," in IEEE Access, vol. 10, pp. 33393-33407, 2022, doi: 10.1109/ACCESS.2022.3161658

III. Jha, R.K.; **Kumar, A.;** Prakash, S.; Jaiswal, S.; Bertoluzzo, M.; Kumar, A.; Joshi, B.P.; Forato, M. Modeling of the Resonant Inverter for Wireless Power Transfer Systems Using the Novel MVLT Method. *Vehicles* 2022, *4*, 1277-1287. https://doi.org/10.3390/vehicles4040067

IV. **Kumar, A**.; Bertoluzzo, M.; Jha, R.K.; Sagar, A. Analysis of Losses in Two Different Control Approaches for S-S Wireless Power Transfer Systems for Electric Vehicle. *Energies* 2023, *16*, 1795. https://doi.org/10.3390/en1604179

b) Conference Papers

I. **Abhay Kumar**, M. Bertoluzzo, and A. Sagar," Different loading of Bi-directional wireless power transfer for VaH at good efficiency, "2021 International Conference on Advance Computing and Ingenious Technology in Engineering Science (ICACITES), AIP Proceeding

II. A. Sagar, **A. Kumar** and M. Bertoluzzo, "Design and Analysis of a Robust High-Density Single-Phase Isolated Buck Converter System For Regulated Power Supply," 2022 3rd International Conference for Emerging Technology (INCET), 2022, pp. 1-5, doi: 10.1109/INCET54531.2022.9824560

III. A. Sagar, **A. Kumar**, M. Bertoluzzo, R.K.Jha, "Analysis and Design of a Two-winding Wireless Power Transfer System With Higher System Efficiency and Maximum Load Power," 48th Annual Conference of the Industrial Electronics Society IECON 2022

IV. **Abhay Kumar**, M. Bertoluzzo, and A. Sagar, " Design and control stage comparisons for the V2H wireless power transfer system," International Conference on Hydro and Renewable Energy (ICHRE) 2022, Accept

V. Amritansh Sagar, Manuele Bertoluzzo and **Abhay Kumar** "Analysis and Comprehensive Comparison of Wireless Power Transfer System Using SS and SP topology for Electric Vehicle Charging" 1st International Conference on Computational Intelligence, Communication Technology and Networking (CICTN)2023, Accepted